



**ELECTRONIC QUENCHING OF THE A(0^+_{u})
STATE OF Bi₂**
THESIS

Joseph Lee Cox, First Lieutenant, USAF

AFIT/GAP/ENP/01M-02

**DEPARTMENT OF THE AIR FORCE
AIR UNIVERSITY**

AIR FORCE INSTITUTE OF TECHNOLOGY

Wright-Patterson Air Force Base, Ohio

APPROVED FOR PUBLIC RELEASE; DISTRIBUTION UNLIMITED.

20010730 045

The views expressed in this thesis are those of the author and do not reflect the official policy or position of the United States Air Force, Department of Defense, or the U. S. Government.

AFIT/GAP/ENP/01M-02

ELECTRONIC QUENCHING OF THE A(0^+_{u}) STATE OF Bi₂

THESIS

Presented to the Faculty

Department of Engineering Physics

Graduate School of Engineering and Management

Air Force Institute of Technology

Air University

Air Education and Training Command

In Partial Fulfillment of the Requirements for the

Degree of Master of Science in Applied Physics

Joseph Lee Cox, B.A.

First Lieutenant, USAF

March 2001

APPROVED FOR PUBLIC RELEASE; DISTRIBUTION UNLIMITED.

ELECTRONIC QUENCHING OF THE A(0^+) STATE OF Bi₂

Joseph Lee Cox, B.A.
First Lieutenant, USAF

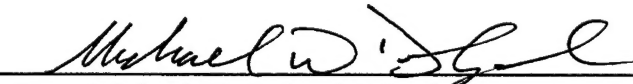
Approved:



2 MAR 01

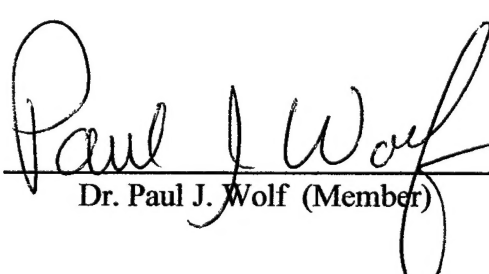
Lt. Col. Glen P. Perram (Chairman)

date


Capt. Michael W. Dolezal (Member)

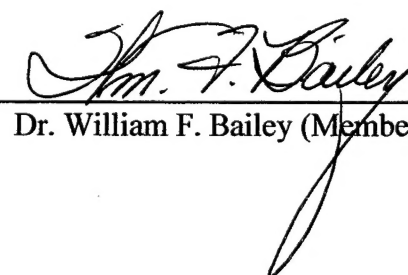
22 Feb 01

date


Dr. Paul J. Wolf (Member)

5 MAR 01

date


Dr. William F. Bailey (Member)

22 Feb 01

date

Acknowledgments

I would like to thank my Uncle [REDACTED] who passed on many years ago, for forcing me to promise him to become a physicist and fulfill a childhood dream. My wife, [REDACTED] has demonstrated remarkable patience and support during all of my academic and professional challenges since the first night we met. This work would not have been accomplished were it not for her love and understanding during eighteen grueling months at the Air Force Institute of Technology.

Joseph Lee Cox

Table of Contents

	Page
Acknowledgments	iv
List of Figures	viii
List of Tables	x
Abstract.....	xi
I. Introduction.....	1
1.1 Background	1
1.2 Motivation to Study Bismuth.....	2
1.2.1 Optically Pumped Bi ₂ Laser.....	3
1.2.2 Energy Transfer Theories.....	3
1.2.3 Support for NF/BiF(A-X) Chemical Laser Development.....	3
1.3 Problem Statement.....	4
1.4 Organization.....	5
II. Theory.....	6
2.1 Rovibrational Spectrum.....	6
2.1.1 Rotational Theory.....	7
2.1.1.1 Rigid Rotor Approximation.....	7
2.1.2 Vibrational Theory.....	9
2.1.3 Electronic Excitation Theory And Dunham Expansion.....	11
2.1.4 Group V Diatomic Structure.....	13
2.1.5 Predissociation.....	14
2.2 Laser Induced Fluorescence.....	16
2.3 Molecular Kinetics.....	18
2.3.1 Energy Transfer Processes.....	19
2.3.2 Master Rate Equation.....	22
2.3.3 Time-Dependent Solution.....	23
2.3.4 Energy Transfer Rates.....	25
2.3.4.1 Landau-Teller Theory.....	27
2.3.4.2 Schwartz, Slawsky, Herzfeld (SSH) Theory.....	28
2.4 Prior Work on Bismuth Dimers.....	29
III. Experimental Apparatus.....	32
3.1 Introduction.....	32
3.2 Experimental Setup.....	32
3.2.1 Bismuth Production and Maintenance of Pressure.....	39

3.3 Experimental Alignment and Characterization.....	42
3.4 Obtaining Fluorescence Data.....	46
3.4.1 Observation of Multiple Fluorescence Lifetimes.....	47
3.4.2 Mathematical Method Used To Extract Fluorescence Data.....	50
IV. Results and Discussion	53
4.1 Introduction.....	53
4.2 Electronic Quenching of Bi ₂ A(0 ⁺ _u).....	53
4.2.1 Quenching by Helium of Vibrational Levels v'=18, 19, 20, 21.....	53
4.2.2 Quenching by Helium of Vibrational Levels v'=22, 23, 24, 25.....	58
4.2.2.1 Single Exponential Fits to Observed Fluorescence.....	58
4.2.2.2 Multiple Exponential Fits to Observed Fluorescence.....	60
4.2.3 Quenching by Neon of Vibrational Levels v'=22, 23.....	63
4.2.3.1 Single Exponential Fits to Observed Fluorescence.....	63
4.2.3.2 Multiple Exponential Fits to Observed Fluorescence.....	65
4.2.4 Quenching by Nitrogen Dimers of Vibrational Levels v'=22, 23.....	66
4.2.4.1 Single Exponential Fits to Observed Fluorescence.....	66
4.2.4.2 Multiple Exponential Fits to Observed Fluorescence.....	68
4.2.5 Quenching by Argon of Vibrational Levels v'=22, 23.....	69
4.2.5.1 Single Exponential Fits to Observed Fluorescence.....	69
4.2.5.2 Multiple Exponential Fits to Observed Fluorescence.....	70
4.2.6 Quenching by Krypton of Vibrational Levels v'=22, 23.....	72
4.2.6.1 Single Exponential Fits to Observed Fluorescence.....	72
4.2.6.2 Multiple Exponential Fits to Observed Fluorescence.....	74
4.2.7 Quenching by Xenon of Vibrational Levels v'=22, 23.....	75
4.2.7.1 Single Exponential Fits to Observed Fluorescence.....	75
4.2.7.2 Multiple Exponential Fits to Observed Fluorescence.....	77
4.3 Qualitative Comparison of Stern-Volmer Plots.....	78
4.3.1 Vibrational Level 22.....	78
4.3.2 Vibrational Level 23.....	81
4.4 Conclusions.....	84
4.4.1 Report of Electronic Quenching Rates.....	84
V. Conclusions.....	85
5.1 Summary of Electronic Quenching Rates.....	85
5.2 Further Studies.....	85
Appendix A Report of Fluorescence Lifetimes.....	87
Appendix B Summary of Errors.....	94
Bibliography.....	99
Vita	102

List of Figures

Figure	Page
2.1. Electronic States of a Diatomic Molecule.....	15
2.2. Energy Transfer Processes.....	21
3.1. Definition of Axes.....	33
3.2. Location of Aluminum Oxide Crucible in Fluorescence Cell.....	34
3.3. Location of Manometer and Buffer Gas Valve.....	35
3.4. Periscope Assembly.....	36
3.5. Identification of Optical System Components.....	37
3.6. Characterization of the Optical System Spectral Response.....	43
3.7. Temporal Profile of the Laser Pulse.....	45
3.8. Radio-Frequency Noise Observed by Oscilloscope.....	46
3.9. Laser Excitation Spectra and Vibrational Level Assignments.....	49
3.10. Fluorescence Decay Curves for Helium Buffer Gas.....	52
4.1. Typical Fluorescence Curve, Helium Buffer Gas, ~3000mTorr, $v'=18$	54
4.2. Logarithm Plot of Fluorescence Curve.....	54
4.3. Residuals to Exponential Fit.....	55
4.4. Stern-Volmer Plot, Pressure versus Decay Rate, for He buffer gas, $v'=18$	56
4.5. Stern-Volmer Plot, Pressure versus Decay Rate, for He buffer gas, $v'=19$	56
4.6. Stern-Volmer Plot, Pressure versus Decay Rate, for He buffer gas, $v'=20$	57
4.7. Stern-Volmer Plot, Pressure versus Decay Rate, for He buffer gas, $v'=21$	57
4.8. Stern-Volmer Plot, He buffer gas, $v'=18, 19, 20, 21$	58
4.9. Stern-Volmer Plot, Single Exponential Fit, He buffer gas, $v'=22$	62

4.10. Stern-Volmer Plot, Single Exponential Fit, He buffer gas, $v' = 23$	62
4.11. Stern-Volmer Plot, He buffer gas, $v' = 23$, Double Exponential Fit.....	63
4.12. Stern-Volmer Plot, Ne buffer gas, $v' = 22$	64
4.13. Stern-Volmer Plot, Ne buffer gas, $v' = 23$	65
4.14. Stern-Volmer Plot, Ne buffer gas, $v' = 23$, Double Exponential Fit.....	66
4.15. Stern-Volmer Plot, N_2 buffer gas, $v' = 22$	67
4.16. Stern-Volmer Plot, N_2 buffer gas, $v' = 23$	68
4.17. Stern-Volmer Plot, N_2 buffer gas, $v' = 23$, Double Exponential Fit.....	69
4.18. Stern-Volmer Plot, Ar buffer gas, $v' = 22$	71
4.19. Stern-Volmer Plot, Ar buffer gas, $v' = 23$	71
4.20. Stern-Volmer Plot, Ar buffer gas, $v' = 23$, Double Exponential Fit.....	72
4.21. Stern-Volmer Plot, Kr buffer gas, $v' = 22$	73
4.22. Stern-Volmer Plot, Kr buffer gas, $v' = 23$	74
4.23. Stern-Volmer Plot, Kr buffer gas, $v' = 23$, Double Exponential Fit.....	75
4.24. Stern-Volmer Plot, Xe buffer gas, $v' = 22$	76
4.25. Stern-Volmer Plot, Xe buffer gas, $v' = 23$	77
4.26. Stern-Volmer Plot, Xe buffer gas, $v' = 23$. Double Exponential Fit.....	78
4.27. Stern-Volmer Summary of all Buffer Gasses, $v' = 22$	80
4.28. Plot of Quenching Probability with Reduced Mass, $v' = 22$	81
4.29. Stern-Volmer Summary of all Buffer Gasses, $v' = 23$	82
4.30. Stern-Volmer Summary of all Buffer Gasses, $v' = 23$	83
4.31. Plot of Quenching Probability with Reduced Mass, $v' = 23$	83

List of Tables

Table	Page
2.1. Gas Kinetic Collision Parameters for Bi ₂	26
3.1. Research Grade Buffer Gasses.....	42
3.2. Dye Laser Indicated Wavelengths.....	44
4.1. Collision Free Lifetimes and Approximate Rotational Levels, He Buffer Gas.....	61
4.2. Electronic Quenching Rates by Helium Buffer Gas.....	61
4.3. Collision Free Lifetimes and Approximate Rotational Levels, Ne Buffer Gas.....	65
4.4. Electronic Quenching Rates by Neon Buffer Gas.....	66
4.5. Collision Free Decay Rate and Approximate Rotational Levels, N ₂ Buffer Gas.....	68
4.6. Electronic Quenching Rates by Nitrogen Buffer Gas.....	69
4.7. Collision Free Decay Rate and Approximate Rotational Levels, Ar Buffer Gas.....	70
4.8. Electronic Quenching Rates by Argon Buffer Gas.....	72
4.9. Collision Free Decay Rate and Approximate Rotational Levels, Kr Buffer Gas.....	74
4.10. Electronic Quenching Rates by Krypton Buffer Gas.....	74
4.11. Collision Free Lifetimes and Approximate Rotational Levels, Xenon.....	76
4.12. Electronic Quenching Rates by Xenon Buffer Gas.....	78
4.13. Electronic Quenching Probabilities, v'=22.....	80
4.14. Electronic Quenching Probabilities, v'=23.....	82
4.15. A Summary of Electronic Quenching Rates.....	84

Abstract

Temporally-resolved laser induced fluorescence of high vibrational levels in Bi₂A(0_u⁺) above and below the predissociation limit of v'=22 were investigated by observing total fluorescence from a wavelength tunable, pulsed dye laser. Electronic quenching of Bi₂A(0_u⁺) by five collision partners (Ne, Ar, Kr, Xe, N₂) was examined for four vibrational levels (v'=22, 23, 24, 25). Electronic quenching by a sixth collision partner (He) was examined for eight vibrational levels (v'=18 through 25). The quenching from stable vibrational levels (v'≤22) was independent of vibrational quantum number. A significant increase in quenching occurs for the predissociated level v'=23. Electronic quenching transfer rates ranged from 227.3 to 850.5x10⁻¹³ cm³ molec⁻¹ sec⁻¹ for v'=22 and from 741.2 to 1570x10⁻¹³ cm³ molec⁻¹ sec⁻¹ for v'=23, and are very nearly gas kinetic for v'=23. Electronic quenching of higher vibrational levels (v'>23) was not temporally resolvable by the experimental apparatus.

ELECTRONIC QUENCHING OF THE A(0⁻_u) STATE OF Bi₂

I. Introduction

"It isn't very often an innovation comes along that revolutionizes our operational concepts, tactics, and strategies. You can probably name them on one hand – the atomic bomb, the satellite, the jet engine, stealth, and the microchip. It's possible the airborne laser is in this league." Secretary of the Air Force, Sheila E. Widnall in 1997. (McKenna, 1997, 10).

1.1 Background Chemical lasers derive their source of power from exothermic chemical reactions in which one of the products is left in an electronically or vibrationally excited state with a decay lifetime long enough to develop a population inversion over the lower state in the lasing transition. The concept of a vibrational chemical laser was first developed by Polanyi in 1961 and demonstrated by Kasper and Pimental in 1965 (Polanyi, 1961; 347 and Perram, 2000). The first purely chemical HF laser was introduced in 1969 by Cool and Stevens (Perram, 2000). Lasing in the infrared at 2.640-2.954 μ m, the HF laser has demonstrated mass efficiency of ~150kJ/kg. An HF laser called MIRACL has been tested at over 1MW. The advancement of chemical lasers has been so rapid that initial deployment of chemical laser weapons systems is expected within the decade.

A chemical laser known as COIL, chemically pumped oxygen iodine laser, is the basis for the weapons system called the Airborne Laser (ABL) (Vizard, 1999; 60). The ABL will primarily serve in a defensive role against theater ballistic missiles upon its

deployment in the first decade of this century. COIL was selected as a laser source because of its high power, in the megawatts, high beam quality, and because it had the shortest wavelength of any high powered chemical laser of its time (Perram, 2000).

Laser weapons systems have been considered for deployment in space by the United States Air Force since the early 1970s as a means of defense against intercontinental ballistic missiles (Pines, 1987; 34). A unique concern to laser systems in space is the accumulation of heat by the laser and the difficulty of space systems to cool as the only avenue available is the slow process of radiative cooling. Chemical lasers derive their energy sources from chemical reactions. As a normal process of chemical laser systems, these products are vented into space and the accumulation of heat is much less of a concern (Perram, 2001). The launch weight of a space system is limited by the launch vehicles available and the enormous cost of putting a payload in space. A large laser power source would invariably restrict the deployability and affordability of space based ballistic missile defense systems (Pines, 1987; 34). The potential for great mass efficiency (energy emitted per mass of fuel), high beam quality, and thermal characteristics make a chemical laser an ideal candidate for a space based weapons system.

1.2 Motivation To Study Bismuth Bismuth is the heaviest stable diatomic molecule. The spectroscopy and chemical kinetics are only recently being reported, but growing interest in bismuth dimers has sprung from the search for visible lasers that would be applicable to such diverse fields as spectroscopy and weapons systems development.

1.2.1 Optically Pumped Bi₂ Laser. West and Broida developed an optically pumped vapor phase Bi₂ laser in the late 1970's (West, 1978; 283) with laser emission between 650-710nm. This system was refined a few years later (Drosch, 1982; 123) to include laser transitions from 590-790nm at up to 150mw output power. Though this system does not show promise as a high-energy chemical laser for weapons applications, it has already proven its merit in the spectroscopic study of a previously unobserved band system of Sr₂ (Drosch, 1982; 129). The primary application for the optically pumped bismuth laser will likely be as a spectroscopic tool.

1.2.2 Energy Transfer Theories. Currently accepted energy transfer theories depend upon a condition known as adiabaticity, meaning that in the course of a vibrational collision, no net exchange of energy occurs between the vibrating oscillator and the translating particle. A severe stress of such a condition is when the mass of the colliding particle is much less than the active molecule. Bi₂ is the heaviest stable diatomic molecule and a Bi₂-He collision pair would be the best candidate for such a test. These energy transfer theories are fundamental to molecular theory and any departure of theory from experimental observation is critical to spectroscopic research.

1.2.3 Support for NF/BiF(A-X) Chemical Laser Development. The primary reason for the study of Bi₂ is to enhance the development of the NF/BiF(A-X) chemical laser system. The effectiveness of a laser weapons system is primarily based upon the fluence, or beam intensity delivered on target. Fluence is directly proportional to the square of the laser frequency and inversely proportional to the distance to target. The effectiveness of COIL on an airborne platform, operating in the infrared at a wavelength of 1.315μm at a

few hundred miles to the target, is enough to accomplish its primary mission of defense against theater ballistic missiles. However, for space based applications at distances of several thousand miles COIL will be ineffective against intercontinental ballistic missiles. A visible chemical laser is therefore being sought as a weapons system to be deployed in space (Pines, 1987; 34).

One such visible chemical laser under development is the NF/BiF(A-X) laser which has proven operation at 470nm (Bernard, 1993; 2900). This laser would realize a 30-40 fold increase in fluence as compared to an HF laser with an equivalent output power (Perram, 1992). Bismuth dimers are an undesirable by-product of the chemical reaction generating the laser and the electronic quenching of excited BiF by Bi₂ is not well understood (Franklin, 1997; 1-4). The spectroscopic and kinetic studies of bismuth dimers are important research to further the development of this visible chemical laser.

1.3 Problem Statement Pulsed laser excitation and temporally resolved laser induced fluorescence techniques were used in this experiment to investigate fundamental collisional dynamics of molecular bismuth. Eight vibrational levels of the electronically excited A(0⁺_u) state (v'=18 through v'=25) were observed under the influence of buffer gasses with pressures varying from 500mTorr to 5 Torr. All eight vibrational levels were explored for He, while only the last four, v'=22, 23, 24, and 25, were explored for Ne, Ar, N₂, Kr, and Xe. Electronic quenching rates were reported for vibrational levels 18 through 23. Using the temporally resolved fluorescence data, state to state vibrational

energy transfer was studied and compared to popular energy transfer rate theories, including the SSH theory.

1.4 Organization Background theory will be presented in Chapter II beginning with a development of spectroscopy that will be relevant to the Bi₂(A→X) system, followed by a discussion of pulsed laser induced fluorescence techniques, molecular kinetics, and a review of prior work on bismuth dimers. Chapter III will explain the experimental apparatus and report the results of the temporally resolved laser induced fluorescence observed. Chapter IV will compare the extracted electronic quenching rates and discuss the impact of these rates with regard to current theories in molecular kinetics. Chapter V will present the conclusions of this research and suggest future research possibilities on the Bi₂(A→X) system.

II. Theory

The organization of the theory section is designed to present progressive blocks of theory that will be built upon in later sections of this chapter. A general theory of the rovibrational spectra is introduced first, followed by a study of laser induced fluorescence. A section on molecular kinetics is then included with particular emphasis on the experimental investigation to follow. Finally, a presentation of prior research in bismuth dimers will be made focused on laser induced fluorescence experiments of the $\text{Bi}_2(\text{A} \rightarrow \text{X})$ system.

2.1 Rovibrational Spectrum A review of the theory of rovibrational spectroscopy will begin with a treatment of the lowest contribution to the energy of the system, rotation, which when spectrally resolved has a structure that may be analyzed independently of the greater contributors. Upon this foundation, vibrational interactions will be included, with electronic energy last. The diatomic structure of Group V atoms, of which bismuth is one, will be presented. The Hund's cases that explain the interaction of electron spin and orbital angular momenta, a crucial ingredient to the spectra of heavy diatomic molecules, will be shown. The rovibrational spectra of bismuth dimers at high vibrational levels are a specific topic of interest to this work, so the effect of predissociation in rovibrational spectra will be introduced last.

2.1.1 Rotational Theory. The rovibrational spectra of bismuth are optically dense.

Vibrational manifolds and their associated rotational structure tend to blend together throughout the entire excited electronic state to the predissociated levels. Fortunately, the diatomic molecule under investigation is formed of only one isotope, $^{209}\text{Bi}^{209}\text{Bi}$.

Discernment of the rotational structure from the vibrational levels is an important step in recognizing the contributions of rotation on the effect of predissociation and the chemical kinetics under investigation.

2.1.1.1 Rigid Rotor Approximation. The rigid rotor approximation assumes two masses, m_1 and m_2 , are separated by a fixed distance r . The bodies rotate about their center of mass with moment of inertia I and angular frequency ω . The kinetic energy of rotation is equal to

$$E_{\text{rot}} = \frac{1}{2} I \omega^2 \quad (2.1.1)$$

The energy of rotation may be rewritten in terms of the angular momentum \mathbf{L}

$$\mathbf{L} = I \omega \quad (2.1.2)$$

Such that

$$E_{\text{rot}} = \frac{1}{2} \mathbf{L}^2 / I \quad (2.1.3)$$

To transform this classically derived equation into one of quantum mechanical significance, \mathbf{L} is replaced by a quantum mechanical operator $\hbar J$, where \hbar is the basic unit of angular momentum for quantum systems and J is a dimensionless operator.

$$\mathbf{L} \Rightarrow \hbar J \quad (2.1.4)$$

The energy of rotation has therefore been transformed into an operator called the rotational Hamiltonian

$$\mathbf{H}_{\text{rot}} = (\hbar^2/2I) \mathbf{J}^2 \quad (2.1.5)$$

Angular momentum theory gives the solution of \mathbf{H}_{rot} as

$$\mathbf{J}^2 \Psi_J = J(J+1) \Psi_J \quad (2.1.6)$$

Where $J = 0, 1, 2, 3, \dots$ and Ψ_J is the eigenfunction. Only states with angular momentum of magnitude $\hbar \sqrt{J(J+1)}$ are allowed by quantum mechanics, so that quantized values of the rotational energy can be expressed by:

$$E_{\text{rot}} = (\hbar^2/2I) J(J+1) \quad (2.1.7)$$

The energy in rotational levels increases quadratically with J , and the rotational energy levels depend inversely on the moment of inertia I . Thus, the greater the moment of inertia, the more closely spaced are the energy levels. The coefficient of the $J(J+1)$ term determines the spacing of these levels and is known as the rotational constant B .

$$B = \hbar^2/2 I, \text{ in Joules for energy units} \quad (2.1.8a)$$

$$B = \hbar^2/2 h I, \text{ in Hertz for frequency units} \quad (2.1.8b)$$

$$B = \hbar^2/2 h c I, \text{ in cm}^{-1} \text{ for wavenumbers} \quad (2.1.8c)$$

The energy of rotation for a diatomic molecule using the rigid rotor approximation can then be expressed by

$$E_{\text{rot}} = B J(J+1) \quad (2.1.9)$$

A laboratory fixed reference frame can be created by the introduction of external electric or magnetic fields. The component of total rotational angular momentum along the laboratory fixed z axis can be measured. This quantity is usually referred to as M_J , an eigenvalue of the equation:

$$\mathbf{J}_z \Psi_J = M_J \Psi_J \quad (2.1.10)$$

where $M_J = -J, -J+1, \dots, 0, \dots, J-1, J$. Rotational eigenvalues depend on J but are independent of the quantum number M_J , in the absence of external electric or magnetic fields. Thus, each rotational level J is $(2J+1)$ -fold degenerate.

The Maxwell-Boltzmann distribution function describes the ratio of the population of two energy states under thermal equilibrium as:

$$\frac{n_j}{n_i} = \frac{e^{-\varepsilon_j/kT}}{e^{-\varepsilon_i/kT}} = e^{-\Delta\varepsilon/kT} \quad (2.1.11)$$

$n_j, n_i \equiv$ population of the system in states j and i

$\varepsilon_j, \varepsilon_i \equiv$ energy of the states j and i

$\Delta\varepsilon \equiv$ energy difference between state j and i

$k \equiv$ Boltzmann's constant

$T \equiv$ equilibrium temperature of the system

When an energy level has degenerate quantum states the distribution function must include the degeneracies of each state, g_j and g_i .

$$\frac{n_j}{n_i} = \frac{g_j e^{-\varepsilon_j/kT}}{g_i e^{-\varepsilon_i/kT}} = \frac{g_j}{g_i} e^{-\Delta\varepsilon/kT} \quad (2.1.12)$$

For rotational levels the relative population between levels is:

$$\frac{n_J}{n_0} = \frac{(2J+1)e^{-BJ(J+1)/kT}}{(2(0)+1)e^{-B0}} = (2J+1)e^{-BJ(J+1)/kT} \quad (2.1.13)$$

2.1.2 Vibrational Theory. The energy levels of a vibrating molecule can be approximated by treating its motion as a harmonic oscillator. Such an oscillator can be represented as a mass on a spring, as in classical mechanics, with a potential energy that

may be applied to the Schreodinger equation to solve for the quantized energy values of the system. The force of a mass on a spring with spring constant k is:

$$F = -kx \quad (2.1.14)$$

with x representing the distance from the equilibrium position. And, since the force is the spatial derivative of the potential energy,

$$\frac{dV(x)}{dx} = -F(x) = kx \quad (2.1.15)$$

$$V(x) = \frac{1}{2}kx^2 \quad (2.1.16)$$

When this potential is applied to the Schrodinger's equation, the solution describes the quantization of energy values in the vibrating molecule:

$$E(v) = (v + \frac{1}{2})\hbar\nu_0 \quad (2.1.17)$$

where $\nu_0 = \sqrt{k/m}$ is the fundamental frequency of the oscillator. Note that the quantum mechanical formulation also predicts a non-zero energy value for the lowest (ground) state.

Assuming the molecule behaves as a harmonic oscillator, the relative population between vibrational levels as predicted by Maxwell-Boltzmann is:

$$\frac{n_v}{n_0} = \frac{e^{-(v+\frac{1}{2})\hbar\nu_0/kT}}{e^{(\frac{1}{2})\hbar\nu_0/kT}} = e^{-\hbar\nu_0/kT} \quad (2.1.18)$$

The two approximations, the rigid rotor and harmonic oscillator, do not fully characterize the system as vibration and rotation are interrelated. For example, the harmonic oscillator does not allow the molecule to dissociate at large internuclear

separation. Furthermore, the difference in energy between successive states becomes increasingly less with increasing quantum number.

2.1.3 Electronic Excitation Theory And Dunham Expansion. A more suitable representation of the energy states of a diatomic molecule can be found in the Dunham Expansion, which involves power series expansions of the aforementioned approximations. The total energy, E_{tot} , of a diatomic molecule is assumed separable:

$$E_{tot} = E_{ele} + E_{int} + E_{trans} \quad (2.1.19)$$

E_{trans} ≡ The translation energy of the molecule about its center of mass

E_{int} ≡ The internal energy of the molecule, vibration and rotation

E_{ele} ≡ The energy from the electronic excitation of the molecule

Or, alternatively, this separation may be written as:

$$E_{tot} = T_e + G_v + F_v(J) + E_{trans} \quad (2.1.20)$$

T_e ≡ The electronic state of the molecule, as before.

G_v ≡ The energy strictly of its vibrational nature

$F_v(J)$ ≡ Energy from rotation (coupled with its vibration)

The Dunham Expansion generates a series of terms that may be taken to whatever number of terms as suits the desired precision of the calculation. For the vibrational energy:

$$G_v = \omega_e(v + 1/2) - \omega_e\chi_e(v + 1/2)^2 + \omega_e\gamma_e(v + 1/2)^3 + \dots \quad (2.1.21)$$

The factor $\varpi_e \chi_e$ gives a rough value of the anharmonicity of the diatomic molecule. The rotational energy is a power series expansion of the solution to the rotational Hamiltonian:

$$F_v(J) = B_v J(J+1) - D_v J^2(J+1)^2 + H_v J^3(J+1)^3 + \dots \quad (2.1.22)$$

The coefficients of this expansion are also power series expansions of $(v+1/2)$.

$$B_v = B_e - \alpha_e(v+1/2) + \gamma_e(v+1/2)^2 + \delta_e.(v+1/2)^3 + \dots \quad (2.1.23)$$

$$D_v = D_e - \beta_e(v+1/2) + \eta_e(v+1/2)^2 + \dots \quad (2.1.24)$$

$$H_v = H_e - \xi_e(v+1/2) + \dots \quad (2.1.25)$$

The top three equations include a negative sign before the second term (first power) of the expansion so that the second term coefficients, which are nearly always determined as negative values, may therefore be reported as positive. B_v represents the familiar coefficient of the quantized energy levels as provided by the solution of the rotational Hamiltonian. Though the Dunham Expansion is complex in that it involves a large number of terms of separate dependencies, it is very flexible in that any diatomic molecule may be represented by these energy levels provided the coefficients to the expansion terms were appropriately selected. The normal course of obtaining these coefficients is by obtaining spectroscopic data, performing vibrational and rotational assignments, and then fitting the experimental data to the coefficients.

During electronic transitions, there are no selection rules governing the vibrational levels corresponding to that transition. Rotational quantum number, however, may only change by $\Delta J=\pm 1$. There are only two rotational levels that an electronic-vibrational

transition may descend to. This results in two separate branches, P and R, on top of each vibrational transition manifold.

2.1.4 Group V Diatomic Structure. Group V atoms ($Z=N$, P , As , Sb , and Bi) have an outer shell electronic configuration of Znp^3 (where $n=2, 3, 4, 5\dots$). This configuration results in spin orbit term symbols $^4S_{3/2}$, $^2D_{3/2}$, $^2D_{5/2}$, $^2P_{1/2}$, and $^2P_{3/2}$, with $^4S_{3/2}$ at the lowest energy according to Hund's rules.

The electronic wavefunctions are described by a spectroscopic symbol written with the convention $^{2\Sigma+1}\Lambda_\Omega$, where Λ is the total orbital angular momentum, Ω is the total electronic angular momentum along the internuclear axis (the sum of the total orbital angular momentum and electronic spin quantum number), and $2\Sigma+1$ is the spin multiplicity of the state. A wavefunction is described as either gerade or ungerade depending upon the nature of the combination of the atomic orbitals and the resultant symmetry under inversion. Furthermore, a molecular wavefunction is described as either + or - depending upon its symmetry with respect to the permutation operator of quantum mechanics. A ground state molecule with multiplicity 1 (no spin degeneracy), symmetrical with respect to permutation, symmetrical with respect to inversion, and zero total orbital angular momentum will be written as $^1\Sigma_g^+$ with the value for the total electronic angular momentum of zero left off because of its obviousness.

Determination of molecular orbital configuration is customarily performed by a linear combination of atomic orbitals using the MO-LCAO approximation; or Molecular Orbital- Linear Combination of Atomic Orbitals (Brown, 1998; 60). Accordingly, two $^4S_{3/2}$ atoms combine to form σ_g , σ_u , π_g , and π_u molecular orbitals. The homonuclear

diatomic combinations for group V elements results in the series

$(\sigma_g 6S)^2 (\sigma_u 6S)^2 (\sigma_g 6P)^2 (\pi_u 6P)^4$, leaving ${}^1\Sigma_g^+$ as the only ground molecular state (or X-state). The first electronically excited state (or A state) proceeds through a similar development as above with the resultant spectroscopic term 0_u^+ .

Hund investigated angular momentum coupling and described five limiting cases that adequately describe the majority of molecules (Bernath, 1995; 323). Most of group V atoms are described by case (a) in which the electron spin and orbital angular momentum are strongly coupled to the internuclear axis but weakly to each other. For heavy diatomic molecules of the group V atoms, Hund's case (c) is a more suitable approximation (Gerber, 1976; 3410). In this case, spin-orbit coupling is so strong that it cannot be neglected as in case (a) (fine structure splitting ${}^2D_{3/2}$ - ${}^2D_{5/2}$ in atomic bismuth is 4019cm^{-1} , whereas atomic nitrogen is only 8cm^{-1}). The strong coupling means that most of the quantum numbers used to define the spectroscopic term symbols are misleading, and independent electronic states should be labeled purely by their total electronic angular momentum quantum number, Ω , dropping the spin multiplicity and total orbital angular momentum quantum numbers (for example, $B^3\Pi_{0_u^+} \rightarrow B0_u^+$).

2.1.5 Predissociation. Predissociation is possible when vibrational energy levels of a bound electronic state overlap with continuum energy levels from a repulsive (or unbound) state. This can occur for any excited state vibrational level with energy greater than the ground state dissociation energy. The Franck-Condon principle applies to these non-radiative transitions and predissociation is only possible when there is a measurable overlap of bound and un-bound wavefunctions at the same internuclear separation.

Predissociation results in the loss of an excited state molecule in a non-radiative process without an emitted photon and the effect on a sample are a shortening of the excited state lifetime.

Predissociation is important in the spectroscopic and kinetic studies of bismuth dimers as it appears to play a major role in the A-state lifetimes of Bi₂ at high vibrational levels (Blondeau, 1980; 246). The potential energy curve of the repulsive predissociation state of interest (Gerber, 1976; 3414) is not well known, but is believed to cross the potential energy curve of the A state at two points and cause the dissociation of diatomic bismuth into translationally excited ground state bismuth atoms, ⁴S_{3/2}Bi + ⁴S_{3/2}Bi, without the capability of residing in any bound states. Such a state is known as a C⁺ repulsive state (Mulliken, 1960; 248). The dissociation of bismuth atoms from the A state occurs at a much higher energy and results in one ground and one electronically excited atom, ⁴S_{3/2}Bi + ²D_{3/2}Bi.

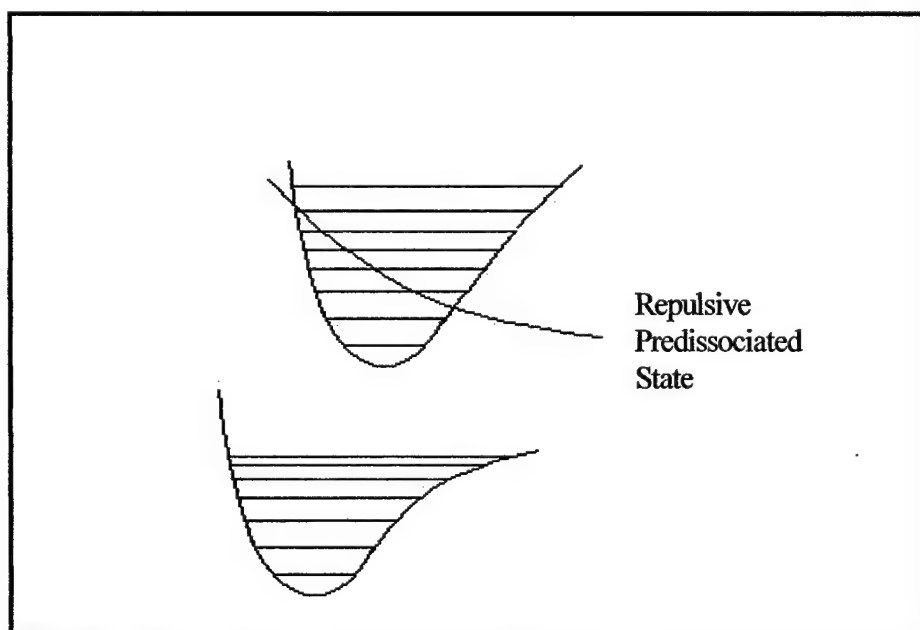


Fig. 2.1. Electronic States of a Diatomic Molecule. A repulsive predissociated state crossing over the electronically excited state.

2.2 Laser Induced Fluorescence The advent of the laser has provided an unparalleled opportunity for spectroscopists to study the nature of matter. The narrow linewidth of a laser source, combined with its comparatively high intensity, enable a scientist to manipulate specific energy levels of a material under study and observe its de-excitation properties. The introduction of wavelength tunability, such as the dye laser, advanced laser spectroscopic techniques further by providing a continuum of energies rather than discrete wavelengths of earlier lasers.

Fluorescence is defined as a set of transitions that occur between states of the same multiplicity. Laser induced fluorescence (LIF) enables a researcher to populate a specific rovibrational state of a species of interest (the parent state), or the vibrational manifold as a whole then conduct measurement of the fluorescence of the initially populated parent state and/or collisionally populated satellite states to determine radiative and non-radiative characteristics of the parent state. Time-dependent fluorescent techniques measure the temporal evolution of the parent and/or satellite states, while time-independent techniques measure the specific wavelengths of fluorescence. The former is usually referred to as temporally-resolved while the latter is known as quantum-resolved or spectrally-resolved fluorescence. Additionally, experiments may be designed that measure both temporally and spectrally simultaneously the fluorescence of an excited species.

Spectrally resolved fluorescence experiments are normally conducted with a CW (continuous wave) laser source and temporally resolved experiments are conducted with pulsed lasers. The advantage of a CW experiment over a pulsed laser experiment is that relative population distributions may be discerned directly by pumping the parent state

and observing the relative intensities of the satellite states. Larger signal intensity is generated in a CW experiment with much greater spectral resolution of the pump transition. A pulsed experiment, however, enables observation of the temporal profiles directly without uncertainty in the time base. Temporal and spectrally resolved experiments are complimentary approaches to ascertain the characteristics of a spectrally excited system. For the purpose of providing background tailored to this thesis, discussion will be limited to time-dependent (i.e. temporally-resolved) laser induced fluorescence techniques.

The excitation of a parent state is dependent on the coupling of the incident energy with the absorption profile of the investigated species. Though the laser, by design, has a very narrow linewidth, it is not infinitely so. The spectral characteristics of the incident laser and the absorption spectra of the investigated material must be understood before characterization of the parent state can be conducted.

In all LIF experiments the effects of Doppler, pressure, and natural broadening of the emitter are present in the observed spectra. Because this experiment focused purely on temporal resolution, as opposed to spectral resolution, the effects of broadening are inconsequential to the observed decay and will be neglected.

Excited states relax to the ground state via collisional, radiative, and collision-less processes. Collisional processes are dependent upon the nature and pressures of the buffer gas used and are intrinsic to the rovibrational state under investigation. An electronically excited vibrational manifold will radiate to a host of ground electronic state vibrational levels and fluorescence intensity invariably appears as a summation of several observed wavelengths.

The fluorescence intensity is:

$$I_f = \sum_{v,w} I_{v,w}^{obs} = \sum_{v,w} \left(\frac{64\pi^4}{3} c v_{v,w}^4 q_{v,w} |\text{Re}|^2 \left(\frac{S_J}{(2J+1)} \right) D(v_{v,w}) N_v \right) \quad (2.2.1)$$

$v_{v,w}$ ≡ transition frequency

$q_{v,w}$ ≡ Franck-Condon factor $|\langle v | w \rangle|^2$

$|\text{Re}|$ ≡ electric dipole moment

S_J ≡ rotational linestrength factor

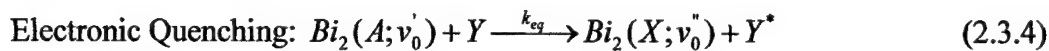
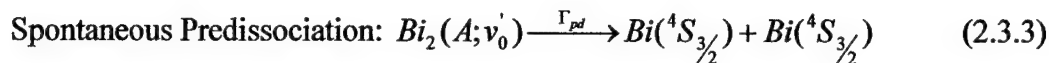
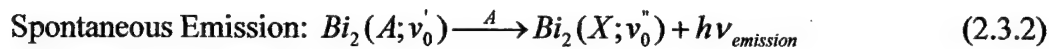
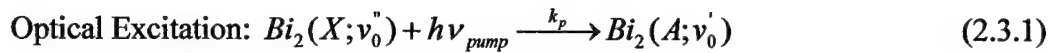
$D(v, w)$ ≡ detection system wavelength dependence

In order to resolve the temporal characteristics of the parent and satellite states, a pulsed laser is necessary rather than a continuous wave laser. Such pulsed laser experiments normally define the initial population of the excited state as a delta function provided the temporal pulse-width is sufficiently small in comparison to the timescale of the observed fluorescence. With regards to the fast, predissociated lifetimes that were observed in this thesis, such approximations are not always valid. Therefore a characterization of the temporal pulse-width and an analysis of the effect on the fluorescence lifetime will be necessary.

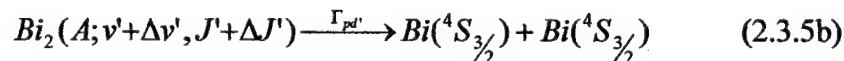
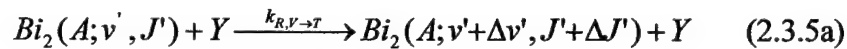
2.3 Molecular Kinetics The section on molecular kinetics will define the processes and reaction rates the system will undergo during excitation and fluorescence. The processes will be used to develop a master rate equation that has a time-dependent solution to be applied to a temporally-resolved fluorescence experiment. Theories of

energy transfer rates will then be presented with emphasis on a few theories that are based upon adiabatic conditions of collisional partners.

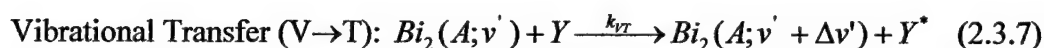
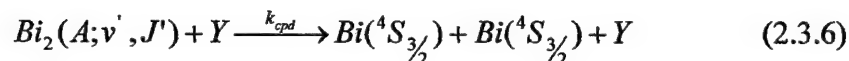
2.3.1 Energy Transfer Processes



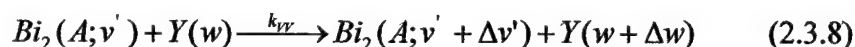
Collisional Predissociation:



or



Vibrational-Vibrational Transfer (V} \rightarrow \text{V}):



In the above equations Y represents a collision partner, Y* an excited collision partner, and Y(w) a molecular collision partner with vibrational quantum number w.

Optical excitation perturbs the thermal population of states by coupling the ground state Bi₂ number density and pump rate constant k_p

$$k_p = \left(\frac{B_{01} I_0}{c} \right) \int_0^{\infty} a(\nu) g_p(\nu) d\nu \quad (2.3.9)$$

B_{01} ≡ Einstein B coefficient of absorption

I_0 ≡ incident laser pump energy

$a(\nu)$ ≡ absorption transition linewidth function

$g_p(\nu)$ ≡ pump laser linewidth function

Selective pumping of a rovibrational level is accomplished when the pump laser linewidth is smaller than and overlapped by the absorption linewidth. Selectivity is questionable when absorption linewidths from multiple rovibrational states overlap each other. Spectrally dense Bi₂ experiences this overlap and the experimenter must take care to ensure the laser energy is coupled into the appropriate vibrational state. For pulsed laser excitation, if the temporal pulsewidth of the laser is short compared to the shortest energy transfer process timescale, the pumping term can be approximated by a delta function centered at t=0. Thus, one may eliminate the source function:

$$N(v')_{t=0} = \delta_{v',v_0} N(v_0')_{t=0} \quad (2.3.10)$$

The radiative lifetime, τ_r , from state v' is related to the spontaneous emission rate, A:

$$\frac{1}{\tau_r(v')} = A(v') = \sum_{v'', J''} A(v', J' \rightarrow v'', J'') \quad (2.3.11)$$

Spontaneous emission is directly proportional to the population in the state so that the temporal evolutions of parent and satellite populations can be monitored by the temporally resolved fluorescence decay.

Spontaneous predissociation is a non-radiative loss process that results in a shortening of the measurable collision-free lifetime of a given excited state. Strong

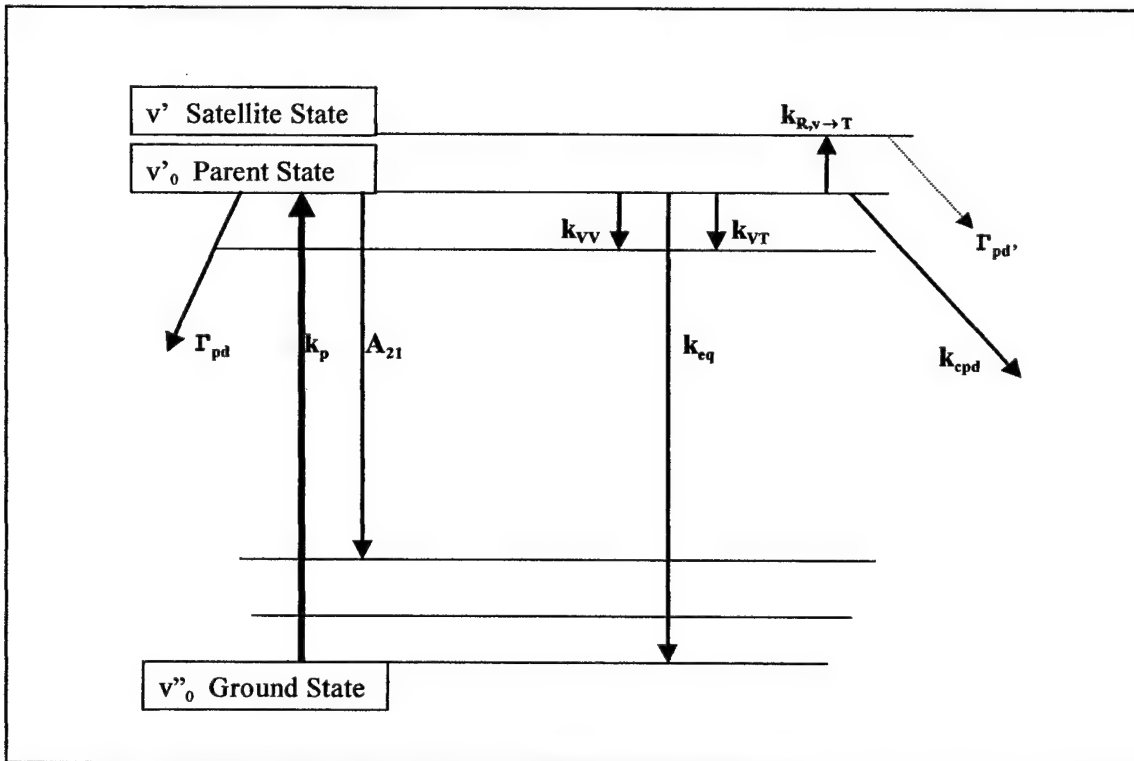


Fig. 2.2. Energy Transfer Processes. Non-collisional processes are on the left and collisional processes are on the right.

predissociation of Bi₂(A) at high vibrational levels is why this vibrational transfer study is of interest. For energy levels well below predissociation, any loss by spontaneous predissociation would be due to quantum tunneling through a large potential barrier and such losses are negligible.

Collisional predissociation is a mechanism that transfers energy to the excited molecule, bringing it to a higher energy state that is then predissociated. Such effects are often referred to as ro-vibrational ladder climbing.

Total vibrational transfer includes vibrational-translational and vibrational-vibrational transfer effects:

$$k_v = k_{vT} + k_{vv} \quad (2.3.12)$$

V-V transfer is only possible with non-atomic buffer gasses as the collision partner must be able to alter its vibrational state. Vibrational transfer depends on the collision partner, the quantum state of the observed specie, and the amount of the energy exchange during collision. Total vibrational transfer out of a single vibrational state to all other vibrational levels for collision partner Y is:

$$k_v^Y(v) = \sum_{\Delta v} k_v^Y(v \rightarrow v + \Delta v) \quad (2.3.13)$$

Electronic quenching refers to the removal of Bi₂(A) to any lower electronic state. Resonant electronic exchange refers to the direct exchange of Bi₂A(0⁺_v) energy to a nearly resonant excited electronic state of the collision partner. This electronic exchange can occur across any of the vibrational manifold in the excited state to vibrational manifolds in the ground state. k_q is defined as the sum of rates due to electronic quenching, resonant electronic exchange, and vibrational ladder climbing to predissociated states.

$$k_q = k_{eq} + k_{ee} + k_v \quad (2.3.14)$$

The term Γ_0 will be used to describe the sum of all non-collisional processes.

2.3.2 Master Rate Equation

The master rate equation (MRE) can be expressed as follows

$$\begin{aligned} \frac{dN(A; v)}{dt} &= S\delta_0(v)N(A; v) - \sum_Y k_q^Y(v)YN(A; v) - \sum_Y k_v^Y(v \rightarrow v + \Delta v)YN(A; v) \\ &+ \sum_Y \sum_{\Delta v} k_v^Y(v + \Delta v \rightarrow v)YN(A; v + \Delta v) \end{aligned} \quad (2.3.15)$$

Summation over Y allows for energy transfer collisions with multiple buffer species. For the purpose of this experiment, the buffer species is overwhelmingly homogeneous and the summation over Y can be neglected.

The last term of the MRE allows for collisional transfer into state v from all other states v+Δv which can be written using simplifications first proposed by Perram (Perram, 1986; 33).

$p = (A;v)$; observed vibrational level

$p_0 = (A;v_0)$; parent vibrational level

$q = (v+\Delta v)$; label for indexed vibrational level

$$W_{pq} = \sum_Y k^Y_v (q \rightarrow p) Y ; V \rightarrow T \text{ rate constant from } q \rightarrow p$$

$$R_{pq} = W_{pq} - \delta_{pq} (\sum_l W_{lp} + \Gamma_0(p) + \sum_M k^M_q (p) M) ; \text{energy transfer rate matrix}$$

δ_{pq} = Kronecker delta function

The MRE can then be written in tensor notation as

$$\frac{dN_p}{dt} = S\delta_{pp_0} + R_{pq} N_q \quad (2.3.16)$$

2.3.3 Time-Dependent Solution. The time dependent solution to the master rate equation is easily obtained by simplification and integration (Perram, 1986; and Franklin, 1997). The MRE can be separated into a series of observed vibrational levels:

$$\frac{dX_p}{dt} = R_{pq} X_q \quad (2.3.17)$$

$$X_p(0) = \delta_{pp_0} \quad (2.3.18)$$

$$X_p = \frac{N_p}{N_{p_0}} \quad (2.3.19)$$

Summing the MRE over all rovibrational states:

$$X_T = \sum_P X_P \quad (2.3.20)$$

$$\begin{aligned} \frac{dX_T}{dt} = & -\sum_P \Gamma_0(p) X_P - \sum_Y \sum_P k_q^Y(p) Y X_P \\ & - \sum_Y \sum_p \sum_q k_v^Y(p \rightarrow q) Y X_p \\ & + \sum_Y \sum_p \sum_q k_v^Y(q \rightarrow p) Y X_q \end{aligned} \quad (2.3.21)$$

A further assumption can be made such that $\Gamma_0(p)$ and $k_q(p)$ are independent of state p .

The last two terms exactly cancel:

$$\sum_Y \sum_p \sum_q k_v^Y(p \rightarrow q) Y X_p = \sum_Y \sum_p \sum_q k_v^Y(q \rightarrow p) Y X_q \quad (2.3.22)$$

with the result that the MRE can be expressed as:

$$\frac{dX_T}{dt} = -(\Gamma_0 + \sum_Y k_q^Y Y) X_T \quad (2.3.23)$$

A solution to the above equation is easily obtained by integrating with respect to time:

$$X_T = \text{Exp}(-t/\tau) \quad (2.3.24)$$

$$\ln(X_T) = -t/\tau \quad (2.3.25)$$

$$\frac{1}{\tau} = \Gamma_0 + \sum_Y k_q^Y Y \quad (2.3.26)$$

The Stern-Vollmer technique is based upon equation [2.3.26], (Stern, 1919; 183).

This time-dependent solution to the MRE is appropriate only if the collision free decay rate, Γ_0 , and the quenching rate, k_q , are independent of state, and if there are only single

collision conditions. With multiple collision conditions, the decay from a given state will represent the eigenvalue of that state and may be totally unrepresentative of the total removal from that state (Perram, 1986; 50).

2.3.4 Energy Transfer Rates. Gas kinetic rates, adiabaticity, and detailed balance are fundamental concepts implemented in energy transfer theories. The gas kinetic rate is used in molecular theory as a baseline to compare and contrast collision processes in an experiment. The theory assumes that all molecules involved in a collision are hard spheres of fixed radii. A collision cross section is first defined as a sum of the cross-sectional areas of the colliding spheres (Kondrat'ev, 1964; 214):

$$\sigma_g = \pi(r_1 + r_2)^2 \quad (2.3.27)$$

where r_1 and r_2 represent the radii of the spheres of the colliding particles. An average relative speed, v_{12} is defined as in thermal physics:

$$v_{12} = (8kT / \pi\mu)^{1/2} \quad (2.3.28)$$

μ ≡ reduced mass of the collision pair, $(m_1+m_2)/m_1m_2$

k ≡ Boltzmann constant

T ≡ temperature of the gas

The rate constant for a gas kinetic bimolecular collision is:

$$k_g = \sigma_g v_{12} \quad (2.3.29)$$

The probability of any event to occur during the collision is:

$$P = \frac{\sigma_{\text{event}}}{\sigma_g} \quad (2.3.30)$$

σ_{event} ≡ cross section for the kinetic process of interest.

Table 2.1 describes gas kinetic rate constants obtained from Franklin.

Table 2.1. Gas Kinetic Collision Parameters for Bi₂ (Franklin, 1997; A-2).

Collision Partner	Cross-Section A ²	Reduced Mass AMU	Velocity (300K) cm/sec	Gas Kinetic Rate Constant (cm ³ /molec-sec)
He	48.3	3.96	1.26x10 ⁵	7.03x10 ⁻¹⁰
Ne	51.8	19.3	5.72x10 ⁴	3.41x10 ⁻¹⁰
Ar	61.0	36.5	4.16x10 ⁴	2.84x10 ⁻¹⁰
Kr	62.4	69.8	3.01x10 ⁴	2.13x10 ⁻¹⁰
Xe	68.7	99.9	2.51x10 ⁴	1.95x10 ⁻¹⁰
N ₂	63.6	26.2	4.91x10 ⁴	3.12x10 ⁻¹⁰

The principle of detailed balance states that when a system reaches equilibrium, the forward and reverse reactions occur at the same rate (Steinfeld, 1999; 24). This principle may be used to generate a relationship between the rates of two consecutive vibrational levels:

$$k_v(v-1 \rightarrow v) = k_v(v \rightarrow v-1) \exp(-\frac{\Delta E_{v,v-1}}{KT}) \quad (2.3.31)$$

The principle of detailed balance is often useful in rate matrix calculations in which V-T transitions to upper vibrational manifolds may be neglected because of the large exponential factor (large spacing between vibrational levels).

Adiabaticity is a useful description of two colliding bodies, defined such that in the course of a vibrational collision, no net exchange of energy occurs between the vibrating oscillator and the translating particle. A classical analogy to this condition is inelasticity between colliding partners in a momentum transfer. A collision will be adiabatic if the mean collision time is greater than the period of the vibrating oscillator,

$$d/v > 1/v_0 \quad (2.3.32)$$

d=interaction distance

v=average relative speed

v_0 =vibration frequency

Since a V-T transfer must create a net exchange in energy, only non-adiabatic conditions would be sufficient for such transfers. Therefore, vibrational transfers will most evident under conditions of strong long-range interactions, small mass collision partners, or small vibrational frequency.

2.3.4.1 Landau-Teller Theory. Under Landau-Teller theory, the long range attractive portion of the potential was neglected and the repulsive portion of the potential was assumed to be the only potential that would affect vibrational energy transfer (Landau, 1936; 35).

$$V(r)=V_0 \text{Exp}(-\alpha r) \quad (2.3.33)$$

$$\alpha=2 \pi v_0/v$$

A probability for vibrational energy transfer from $v'=1$ to $v'=0$, P_{10} , was calculated using time-dependent perturbation theory, resulting in the expression:

$$P_{10} = \text{Exp}[-3(2\mu\pi^4 v^2/\alpha^2 k_B T)^{1/3}] \quad (2.3.34)$$

The matrix elements for collisional V-T transitions are proportional to the matrix elements for radiative transitions. For the harmonic oscillator, the Hermite polynomials allow for the selection rule $\Delta v=\pm 1$, and a scaling of transition probabilities with the equation:

$$P_{v,v-1} = v P_{10} \quad (2.3.35)$$

The above equation leads to the useful scaling equation of V-T rates:

$$k_{vib}(v, v-1) = v k_{vib}(1,0) \quad (2.3.36)$$

It will be useful in the next discussion to appreciate that the logarithm of the probability is proportional to $\mu^{1/3}$.

2.3.4.2 Schwartz, Slawsky, Herzfeld (SSH) Theory. The SSH theory has been used extensively to compare experimentally determined V-T transfer rates (Schwartz, 1952; 1951). Since the attractive portion of the intermolecular potential was neglected in the Landau-Teller theory, the SSH theory includes an attractive term, ϵ , which effectively increases the relative translational energy and therefore, the V-T transfer probabilities.

$$V(r) = V_0 \text{Exp}(-\alpha r) - \epsilon \quad (2.3.37)$$

The quantum-mechanically derived SSH theory predicts the probability for V-T transfer from $v'=1$ to $v'=0$ as

$$P(1,0) = \sigma(1,0)/\sigma_g = M(\theta'/\theta)(\theta'/T)^{1/6} \text{Exp}[-1.5(\theta'/T)^{1/3} + (\theta/2T) + (\epsilon/k_B T)] \quad (2.3.38)$$

$$\theta' = \mu 4\pi^2 L^2 \omega^2 / k_B$$

$$\theta = hc\omega_0 / kT$$

$$M = \sqrt{\frac{2\pi}{3}} \frac{2m_a^2 m_b m_c}{(m_b + m_c)(m_a + m_b)^2 \mu}$$

$$\mu = \frac{m_a(m_b + m_c)}{m_a + m_b + m_c}$$

$\sigma_g \equiv$ gas kinetic cross section

$L \equiv$ interaction length

For moderately coupled systems, $\frac{m_a}{KT} > 1$, the reduced mass dependence in the

exponential θ' factor dominates and the natural logarithm of V-T probability, $\ln[P(1,0)]$, decreases linearly with $\mu^{1/3}$. With smaller vibrational spacing and, therefore, larger V-T probabilities, $P(1,0) \propto \mu^{1/6}$.

In developing the probability for V-T transfer $P(1,0)$ the SSH theory assumes a non-impulsive collision:

$$\csc h^2(\pi\varpi_e L/v) \cong 4 \exp(-2\pi\varpi_e L/v)$$

For strongly coupled systems, $\varpi_e/kT < 1$, this assumption fails. If one assumes a small attractive term, $\varepsilon/kT \approx 0$, then SSH theory may be used to derive interaction lengths from the observed probabilities (Franklin, 1999; 5762). Interaction lengths for very impulsive collisions will be impossibly large and the SSH theoretical prediction for V-T transfer will fail.

2.4 Prior Work on Bismuth Dimers Potential energies of the A and X states of bismuth, useful in the construction of RKR potential curves, were reported over the last two decades. (Gerber, 1976; 3410 and Babaky, 1997; 71). Gerber has reported laser excitation spectra and rotation structure (Gerber, 1982; 415), and other work by Gerber has shown an electronic transition of atomic bismuth at 472.2nm (Gerber, 1976; 3420). A systematic study of lifetime evolution with v' under electronic quenching LIF experiments has shown important decrease of A state lifetime near $v'=22$ and $v'=34$ due to predissociation (Blondeau, 1980; 246).

An optically pumped, vapor phase Bi2 laser was developed by West and Broida in the late 1970's (West, 1978; 283), demonstrating A→X absorption from 540-580nm with

laser emission between 650-710nm. This system was refined a few years later (Drosch, 1982; 123) to include 150 laser transitions from 590-790nm while pumped at 514nm ($v''=1, J''=197 \rightarrow v'=16, J'=198$) from an Argon laser source. Output power was observed at up to 150mw at 1-2 Torr of Argon buffer gas pressure. Vibrational assignments for laser transitions were reported for several v' levels: 9, 16, 17, 19, 20, 21, 24, 31, 34.

A chemically-pumped NF/BiF(A-X) laser has been operational since the early 1990's and shows great promise as a chemical laser weapons system (Benard, 1993; 2900 and Barrow, 1996; 725). The NF/BiF(A-X) laser operates at a wavelength of 470nm by using metastable NF($a1\Delta$) to electronically excite BiF(A). BiF dimers are created by trimethylbismuthine ($\text{Bi}(\text{CH}_3)_3$) which has the undesirable effect of leftover reactant rapidly quenching the excited BiF molecules. J. M. Herbelin has shown that an order of magnitude improvement in excited BiF was achievable by substitution of metallic bismuth for trimethylbismuthine (Herbelin, 1986; 25). In this reaction, Bi atoms are the bismuth donors for generated BiF with Bi_2 dimers as an unnecessary product of the reaction. The potential quenching of electronically excited BiF(A) by Bi_2 in the lasing cavity is of considerable interest. Spectroscopic and kinetic studies of bismuth dimers have recently been performed (Franklin, 1997), with the effects of predissociation on $\text{Bi}_2(\text{A})$ and an emphasis on higher vibrational levels conducted by Dolezal in 1998 (Dolezal, 1999).

Dolezal performed research on the collisional quenching of $\text{Bi}_2(\text{A})$ using self-quenching and out-gassed products as collisional partners for levels $v'=8$ to $v'=39$ for pressures of 10mTorr to 150mTorr with k_q reported only for $v'=21$ and $v'=22$. A set of

predissociative rate constants were reported for these levels as were a Deslander's table and excitation spectra with vibrational assignments. The current study is a supplement to this previous work, focusing on the few states near predissociation and the implementation of rare gas collision partners.

Electronic quenching is best observed at relatively high pressures where a thermalized distribution has been achieved. The observed quenching rate will rise rapidly as the total pressure is reduced as a non-thermal distribution will have greater electronic quenching than a thermal distribution.

Total observed fluorescence is directly proportional to the excited state number density regardless of the detection efficiencies of the various radiated states. At long times the fluorescence decay is exponential (as in equation [2.3.24]) as the system has been able to thermalize. The process of experimentally determining quenching rates is to perform an exponential fit of temporally-resolved fluorescence decay out to several lifetimes. The electronic quenching rates are then averaged over several states.

III. Experimental Apparatus

3.1 Introduction The present study was undertaken to expand the chemical kinetics database for the Bi₂A(0⁺_v) state with emphasis on the vibrational levels near predissociation. The experimental setup is identical to the work performed by Dolezal, and is common to this field of study.

3.2 Experimental Setup The fluorescence cell was a six-way stainless steel cross with 3.8cm diameter arms of 20cm length. Four horizontal arms had quartz windows mounted on their ends. The bottom arm contained a stainless steel feed-through with two parallel 12cm length copper electrodes positioned lengthwise through the bottom arm of the cross. The electrodes had 0.5inch deep, 0.0625inch diameter holes drilled to accept the ends of a coiled tungsten filament. The filament was used to heat bismuth granules in an aluminum oxide crucible to provide for a bismuth vapor sample to fluoresce. About 5g of bismuth granules (Fluka, 99.998% purity) were placed in the 1cm tall by 1cm diameter crucible that fit snugly inside of the coiled center of the tungsten filament. The tungsten filament was carefully bent to align with the two copper electrodes and be firmly placed inside the small holes of the electrodes. The height of the tungsten filament ends were shortened and bent such that the top of the aluminum oxide crucible was approximately 1cm below the bottom of the center of the cross and positioned as close as possible to the center of the vertical axis of the cross. For the purpose of illustration, the vertical axis is defined as the direction of the bottom to the top; the longitudinal axis is aligned through

two horizontal arms and serves as the optical axis of the pump laser, and the lateral axis is at a right angle to the longitudinal axis, through the other two horizontal arms, and serves as the optical axis for the fluorescence detection (see figure 3.1).

The copper electrodes of the electrical feed-through extended outside of the stainless steel bottom and were attached to a Hewlett Packard 6453A DC Power Supply,

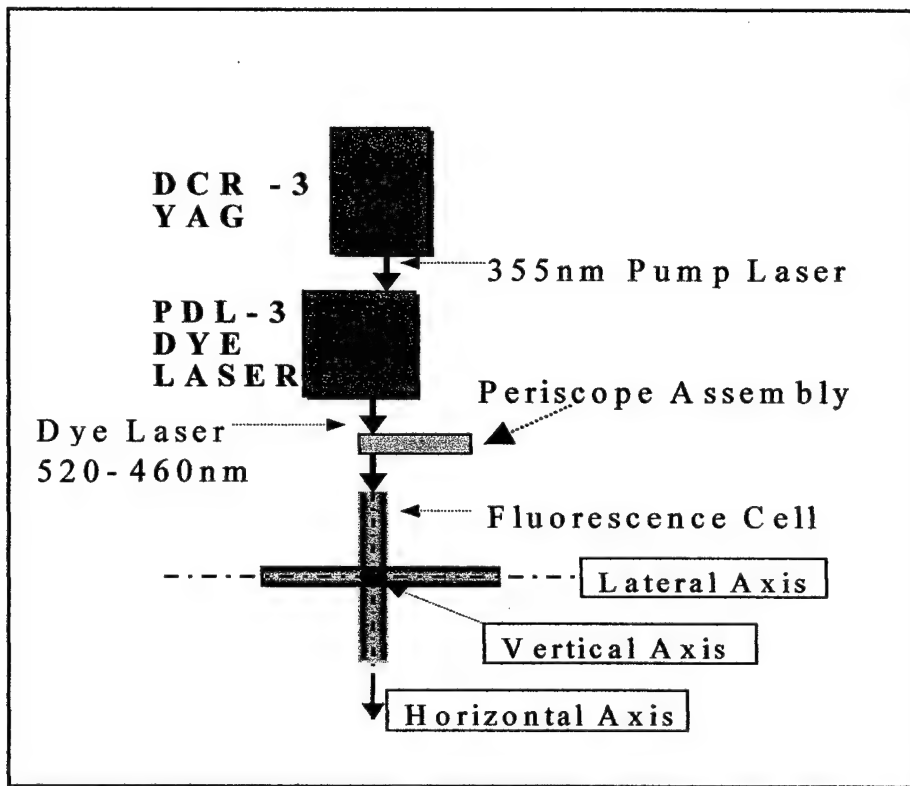


Figure 3.1. Definition of Axes. Top View of Excitation System Set-up.

normally operated at 3V DC with 30-40 amps current (see figure 3.2). The power supply delivered approximately 110 watts to the tungsten filament in order to heat the bismuth sample to 900K. Bismuth has a high melting point (544K) and does not generate appreciable vapor pressures until 900K is maintained. At that temperature bismuth produced vapor pressures of about 2.5mTorr while 60 mole % of the vapor was bismuth dimer with the remainder atomic bismuth (Fischer, 1966:375).

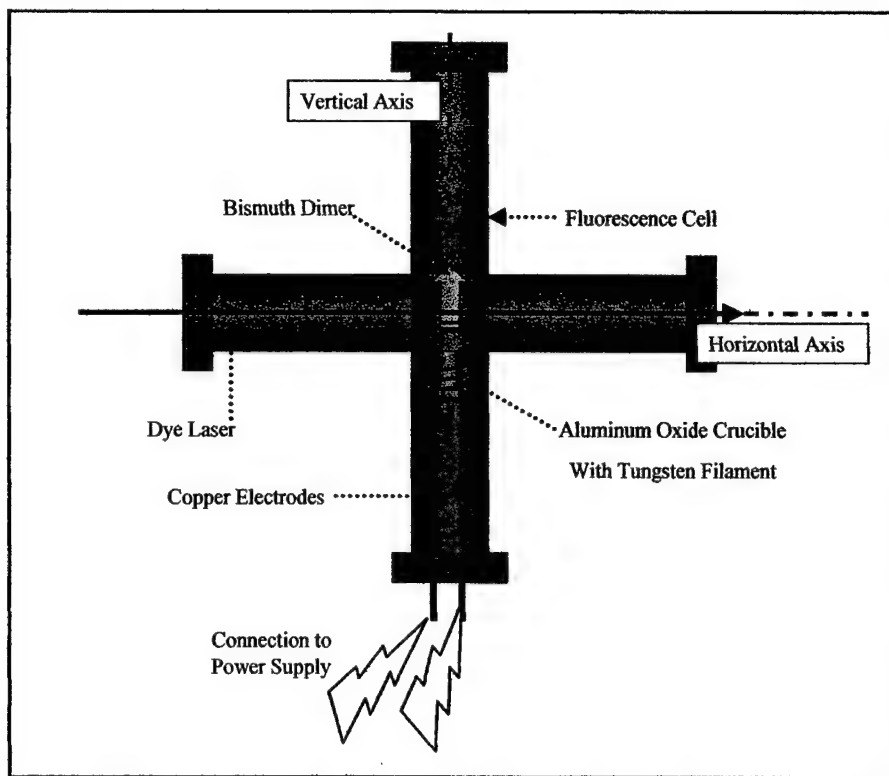


Figure 3.2. Location of Aluminum Oxide Crucible in Fluorescence Cell.

One of the two lateral segments, furthest from the photo multiplier tube assembly, contained two 1/8inch drilled holes, one containing a valve by which to introduce research grade buffer gases into the cell (see figure 3.3). The other hole had attached an MKS Baritron Model 390 capacitance barometer with a range of 0-10 Torr, displaying pressure on an MKS Type 270 signal conditioner. The cell was evacuated with a Varian SD300 mechanical pump that was capable of an ultimate pressure of \approx 5mTorr. The pump was connected to the top arm of the cell by a large diameter stainless steel vacuum tube and mechanical vacuum valve. The minimum sustained pressure of the cell was 17mTorr with a cell leak rate of 4-5mTorr/hour during and after operations. A leak rate of 0.5mTorr/minute was observed when the fluorescence cell was cool. Most of the leak

rate subsided when the copper gaskets connecting the components of the cross expanded under heat.

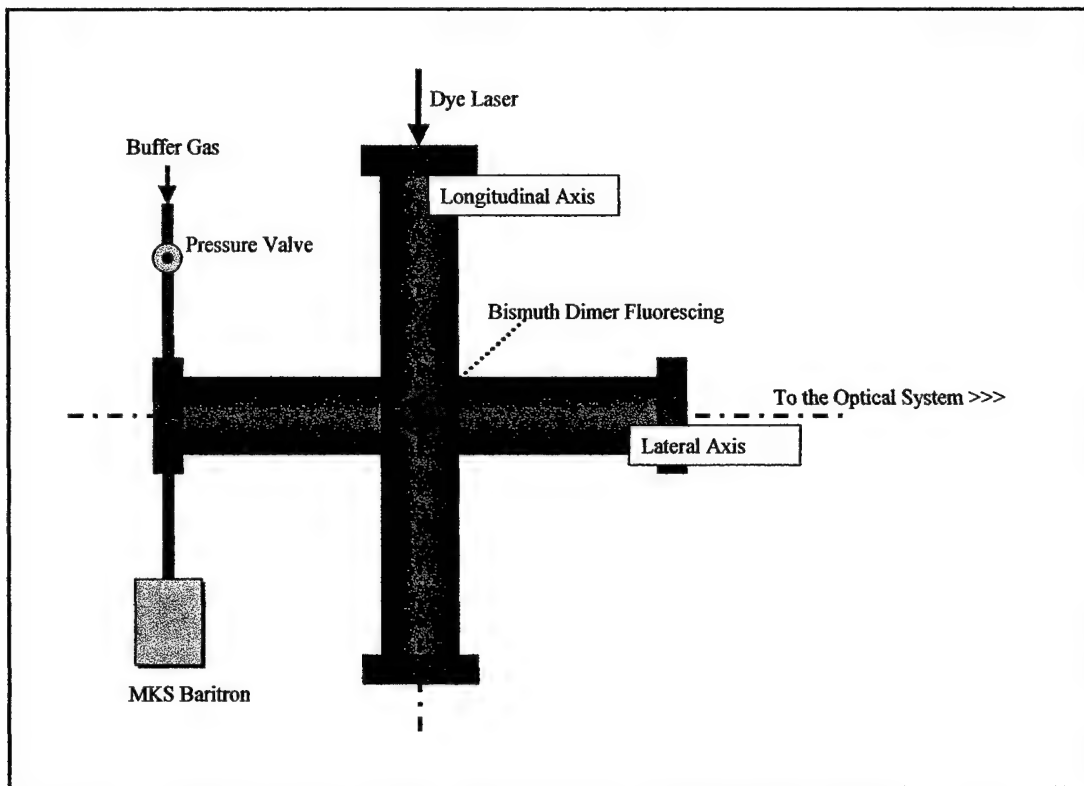


Figure 3.3. Location of Manometer and Buffer Gas Valve.

The longitudinal arm segments were used to pass laser pulses through the cross from a dye laser and periscope apparatus. Laser excitation was provided by a Spectra Physics Quanta-Ray PDL-3 Pulsed Dye Laser pumped by a Spectra Physics DCR-3 Nd:YAG laser (lasing at 1064nm) with a HG harmonic generator and a PHS-1 prism harmonic separator. The harmonic generator was adjusted so as to maximize output of its frequency-tripled 355nm UV pulse. The measured output of the Nd:YAG was 150mJ/pulse at 20 pulses per second in frequency tripled configuration. The manufacturer's specification of the DCR-3 pulse width at 355nm was 5-6nsec. The PDL-3 laser was arranged in longitudinally pumped configuration to generate a dye laser in the

aft end of the laser (as opposed to its side). The dye laser amplifier and oscillator were filled with the manufacturer's recommended molarities of Coumarin-480 and Coumarin-500 (Exciton) dye. The output of the dye laser was 15mJ/pulse when operated with Coumarin-480 (C-480) and 25mJ/pulse when operated with Coumarin-500 (C-500). C-500 dye was used to excite vibrational levels $v'=18, 19, 20$, and 21 with Helium buffer gas while C-480 was used to excite vibrational levels $v'=22, 23, 24$, 25 for all the buffer gases. The output of the dye laser was directed through a prism periscope arrangement to raise the beam to the height of the center of the cross (about 30cm above the optical bench).

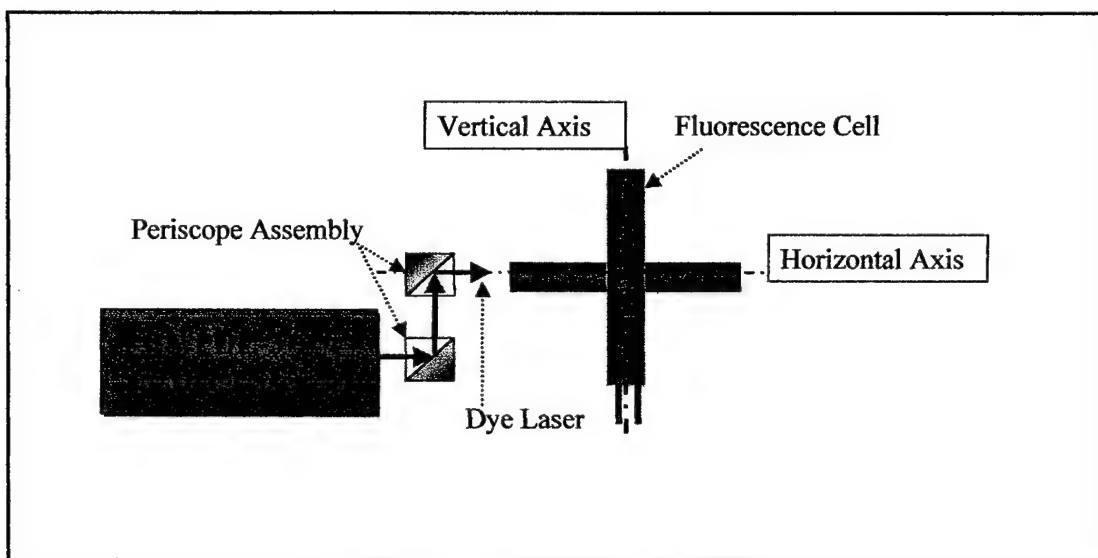


Figure 3.4. Periscope Assembly.

Side fluorescence emissions (LIF) were detected along the lateral axis at a right angle to the laser (longitudinal) axis, on the horizontal arm opposite the Baritron and buffer gas input valve (see figure 3.4). A two-lens system was used to collect and focus the fluorescence emissions. The first lens was a 250mm focal length Newport KPX-202 2 inch diameter lens centered on the lateral axis of the cross approximately 60mm from the

quartz window of the horizontal arm of the cross. This lens was placed exactly one focal length from the fluorescence line at the center of the cell, such that the isotropically

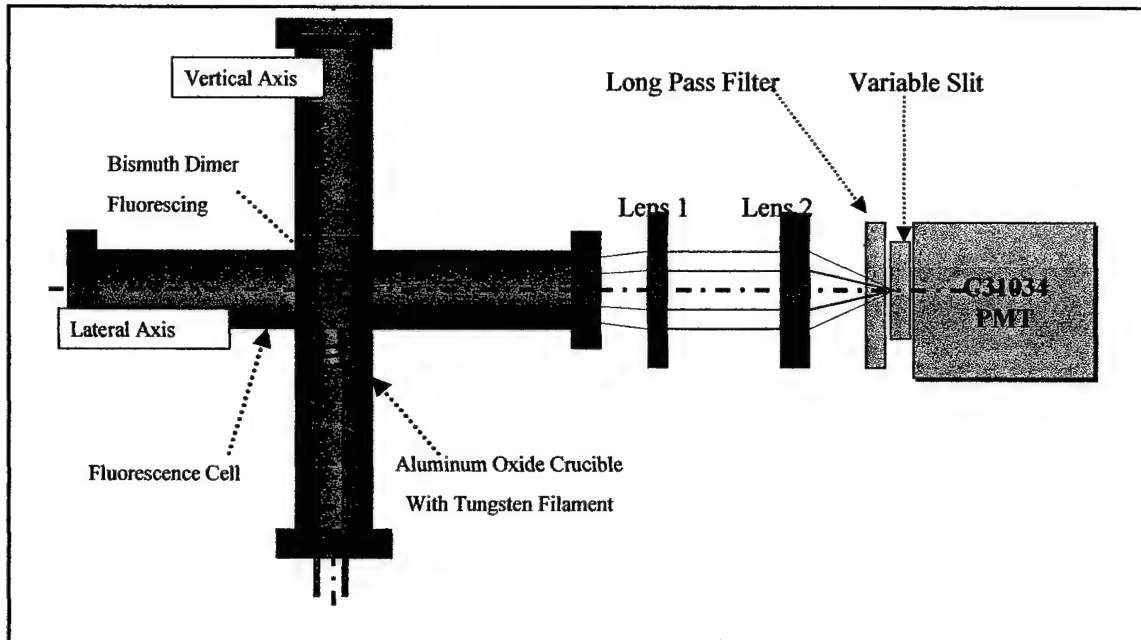


Figure 3.5. Identification of Optical System Components.

radiated fluorescence would be collected and collimated laterally by the lens. The second lens, a 75.6mm focal length Newport KPX-181 2 inch diameter lens, was centered about the lateral axis of the cross ~15cm laterally from the first lens. The second lens was positioned to accept the collimated fluorescence emissions of the first lens, and focus the energy on the PMT. This successfully increased the amount of signal delivered to the PMT while eliminating background laser scatter that would now be off axis of the two-lens system and would not focus.

A Burle Photo Multiplier Tube Model C31034 was positioned on two vertically adjustable lab-jacks at approximately a focal length away from the second lens. Against the entrance window of the PMT was placed a horizontally opening variable rectangular slit that covered all but a small rectangular opening of the PMT window. Using a ruby

rod positioned at the intersection of all three axes at the center of the cell and pumping the rod with the dye laser in order for it to fluoresce, the optical system (the two lenses, rectangular slit, and PMT) was finely positioned to focus the ruby fluorescence onto the center of the entrance slit. In front of the rectangular slit, between the slit and second lens, was placed an LL-600-S-T118 long pass interference filter to attenuate the scattered laser light that would otherwise overwhelm the observation of fluorescence. The filter and horizontal slit were used to minimize collection of scattered laser and ambient light while maintaining a strong fluorescence emission signal.

The PMT was powered via a high voltage BNC cable by a Stanford Research Systems Model PS325 power supply set at negative polarity and typically operated at 1200 volts. The PMT signal output was directed into an EG&G Instruments Model 5185 Wideband Preamplifier via a radio frequency shielded RG-6/U cable. The pre-amplifier was set to 50Ω impedance to match the RG-6/U cable, and a signal gain of 100. The pre-amplifier output signal was transmitted via a second radio frequency (RF) shielded cable to channel one of a LeCroy Model 9450 350MHz Digital Oscilloscope.

A TND-100 photo detector was positioned at the bottom of the periscope assembly to observe the dye laser pulses. This detector was used as the trigger for the oscilloscope by transmitting the detection signal via a third RF shielded cable to channel two of the LeCroy 9450. Observation of fluorescence decay on the oscilloscope was conducted at $0.5\mu\text{sec}/\text{div}$ for the first four vibrational levels ($v'=18, 19, 20, 21$) and at $0.1\mu\text{sec}/\text{div}$ for the final four vibrational levels ($v'=22, 23, 24, 25$). An averaging function was used to increase signal to noise ratio with 5000 sweeps for the helium buffer gas and 2000 sweeps for all other gases.

The optical system was aligned further to increase fluorescence signal prior to recording the first data set. This alignment was unchanged throughout the course of the experiment.

3.2.1 Bismuth Production and Maintenance of Pressure The current of the power supply was adjusted at the beginning of a data collection set (complete characterization of four vibrational levels of a buffer gas) such that the signal intensity was strong enough to provide good data, yet the rate of bismuth production slow enough to last for the entire three to four hour data set. The current on the power supply was kept at \approx 35amps for all fluorescence data obtained, and was not changed during the course of the collection.

There were three sources and one loss mechanism for gasses within the cell. The two primary sources were the added buffer gas and the bismuth vapor production. Buffer gas flowed into the cross from the lateral arm furthest from the photo multiplier tube while bismuth vapor flowed upward from the heated crucible just below the center of the cross. The third source was the leak rate of ambient air into the cross. As this leak rate was very low (around 4mTorr/hour) and assumed to be an isotropic source within the cross, its effects on the production of bismuth are negligible. The loss mechanism was the mechanical pump that pulled gases through the top arm of the cross. The sources and loss created an elongated plume of Bismuth vapor that rose from the aluminum oxide crucible up through the center of the cross into the path of the laser excitation pulse. The flow of buffer gases had the effect of pushing the plume slightly so that the maximum concentration of bismuth was slightly off center of the vertical axis. The buffer gas also had a cooling effect on the bismuth vapor, which quickly returned to solid and plated before reaching the top of the cross.

During alignment of the pulsed laser system it was determined that the maximum fluorescence intensity in the plume is found between 2-3cm above the crucible. The plume, however, changes shape with any change in the pull from the vacuum pump or in the addition of buffer gas. The change in plume shape results in a slight difference in signal intensity as different pressures of gas are maintained in the cell. Laser alignment and calibration was conducted at 2500mTorr Helium buffer gas at 35 amps power supply delivered to the filament. Since the aluminum oxide crucible and tungsten filament radiate in the visible spectrum when heated to 900K, it is important to keep the top of the crucible below the field of view of the PMT through the two lenses. Placement of the crucible 1cm below the bottom of the cross satisfies this requirement while still enabling the excitation laser to reach the maximum fluorescence yield in the bismuth plume.

Before beginning data collection, the purification of gas in the cell was performed. After the cross had reached ultimate pressure, the vacuum valve was closed and the cross pressurized with the research grade buffer gas to ~100Torr. After a few seconds the vacuum valve was opened and the cross evacuated to its ultimate pressure. This cycle was repeated three times. The purpose of this was to decrease the molarities of other gasses in the cell and aid out-gassing. After the third evacuation, the crucible power supply was turned on to 10A DC current with maximum opening of the vacuum pump valve. The crucible and bismuth sample were heated for about two minutes before the current was turned up to 20A. Each successive increase in current aided the out gassing of the bismuth sample as impurities with boiling points less than bismuth were bled off. After two additional minutes at 20A, the power supply was turned up to its

normal operating current of 35amps and the cross re-purified with three sequential saturations of research grade buffer gas as before.

The vacuum valve was opened just enough to maintain ultimate pressure in the cell and it was never closed beyond this point throughout the data collection. This ensured that there was no build-up of bismuth sample impurities or out-gassed impurities in the fluorescence cell. With these methods imposed, along with the initial purification of the cell as explained in the previous paragraph, electronic quenching of any gases other than the buffer gas was completely negligible. Also, since the minimum pressure of buffer gas used in this experiment was 500mTorr, and the vapor pressure of the bismuth sample at 900K was ~2.5mTorr for a minimum ratio of gases of 200:1, any effect of self-quenching by atomic or diatomic bismuth may also be neglected. Although the bismuth dimer is created at a temperature of 900K, it is overwhelmed by at least 200:1 ratio of buffer gas entering the cell at room temperature (300K) and the latter value will be used for all computations in this experiment.

The pressure in the fluorescence cell was often unstable, and constant monitoring required to provide valid measurement. To prevent errors from inaccurate or changing pressure in the cell, all fluorescence data was obtained with less than 0.5% variation in pressure. See Appendix B for a discussion of errors.

Table 3.1. Research Grade Buffer Gasses

BUFFER GAS	GRADE	PURITY
Helium (He)	5.5	99.999995%
Neon (Ne)	5.0	99.999990%
Argon (Ar)	5.0	99.999990%
Krypton (Kr)	5.0	99.999990%
Xenon (Xe)	4.7	99.99997%
Nitrogen (N₂)	5.0	99.999990%

3.3 Experimental Alignment and Characterization The experimental apparatus was characterized and calibrated before commencing with the experiment. The first characteristic to be studied was the spectral transmittance of the PMT and the LL-600-S-T118 long pass interference filter. The GaAs PMT has a uniform, broad spectral response that extends evenly from 900nm to 250nm. The PMT will accurately record the intensity of energy received over the entire band. The filter, however, was placed in front of the PMT and blocked all radiation of wavelength lower than ~600nm. As represented in Figure 3.6, the transmittance of the filter rises smoothly and has a relatively uniform transmittance from ~620nm past the 900nm limit of the PMT. The transmittance effects of the PMT and filter are combined to produce a band pass of wavelengths from 600nm to 900nm. Since, the response is even throughout this band, there will be no spectral transitions favored by the optical system that may cause errors in interpreting the fluorescence data.

The dye laser beam was shaped by mechanical action of the optics inside the PDL-3 dye laser. The dye laser produced an elliptically shaped beam of approximately

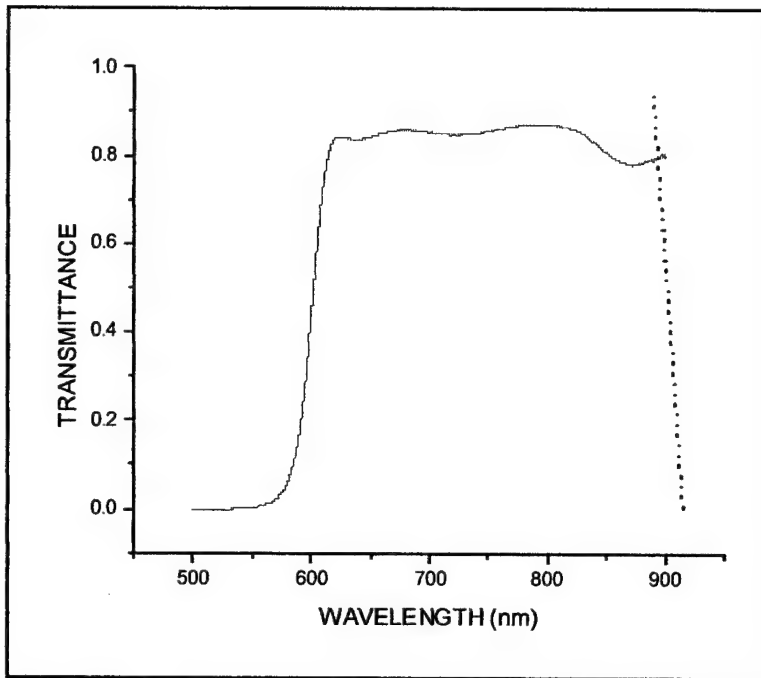


Figure 3.6. Characterization of the Optical System Spectral Response.

The solid curve is the transmittance of the LL-600 filter, and the dashed line is the transmittance cutoff of the C31034 PMT.

1mm width and 3mm in height at the center of the fluorescence cell (at the exact location of the bismuth vapor plume). The manufacturer reported a spectral width of $<0.05\text{cm}^{-1}$ (Spectra Physics, 1-10) and spectral widths of $\sim 0.07\text{cm}$ have been experimentally determined on this dye laser (Melton, 1992; 6667).

The dye laser was determined to have a $+0.3\text{\AA}$ deviation of its indicated wavelength with respect to the Deslanders values experimentally determined for the excited state vibrational levels (Dolezal, 1999). This error was determined by locating the maximum of signal intensity in the $v'=25$ manifold and comparing this indicated wavenumber with the bandhead wavenumber recorded on the Deslanders table. The indicated wavelength on the dye laser is a product of the order of the diffraction grating and the pump wavelength (Spectra-Physics). Table 3.2 shows the vibrational levels pumped, their reported wavenumbers, calculated indicated wavelengths and the actual

Table 3.2. Dye Laser Indicated Wavelengths.

Vibrational Level	Reported Wavenumber cm ⁻¹ (Dolezal,1999)	Diffraction Order (Spectra-Physics)	Calculated Wavelength Indicated (Å)	Actual Wavelength Indicated (Å)	Difference (actual-calculated) (Å)
v'=18	19993.73	5	25007.8	25007.8	0
v'=19	20114.16	5	24858.1	24858.1	0
v'=20	20233.39	5	24711.6	24712.2	0.6
v'=21	20352.05	5	24567.5	24568.2	0.7
v'=22	20469.68	6	29311.6	29312.4	0.8
v'=23	20587.01	6	29144.6	29145.3	0.7
v'=24	20703.46	6	28980.7	28981.4	0.7
v'=25	20818.68	6	28820.3	28820.6	0.3

wavelengths indicated by the dye laser during the experiment. To minimize the effect of multiple level pumping, wavenumbers were chosen further along the vibrational manifold (higher J values) from the bandhead, decreasing the spectral absorption into neighboring vibrational manifolds. Such departures were conducted for levels v'=20 through v'25 at ~0.4Å from reported bandheads and no departures were made for v'=19, and v'=18.

As in figure 3.7, the temporal pulse width of the dye laser resembles a triangular profile with a full width at half maximum (FWHM) of 17.5ns. The extent of the pulse as measured from trigger to a return to baseline (or, full width at full maximum, FWFM) is ~50nsec. Any approximations of the energy rate processes that replace the initial population of the parent state with a delta function must be under the consideration of the temporal profile, which is of the order of decay rates for vibrational level 25.

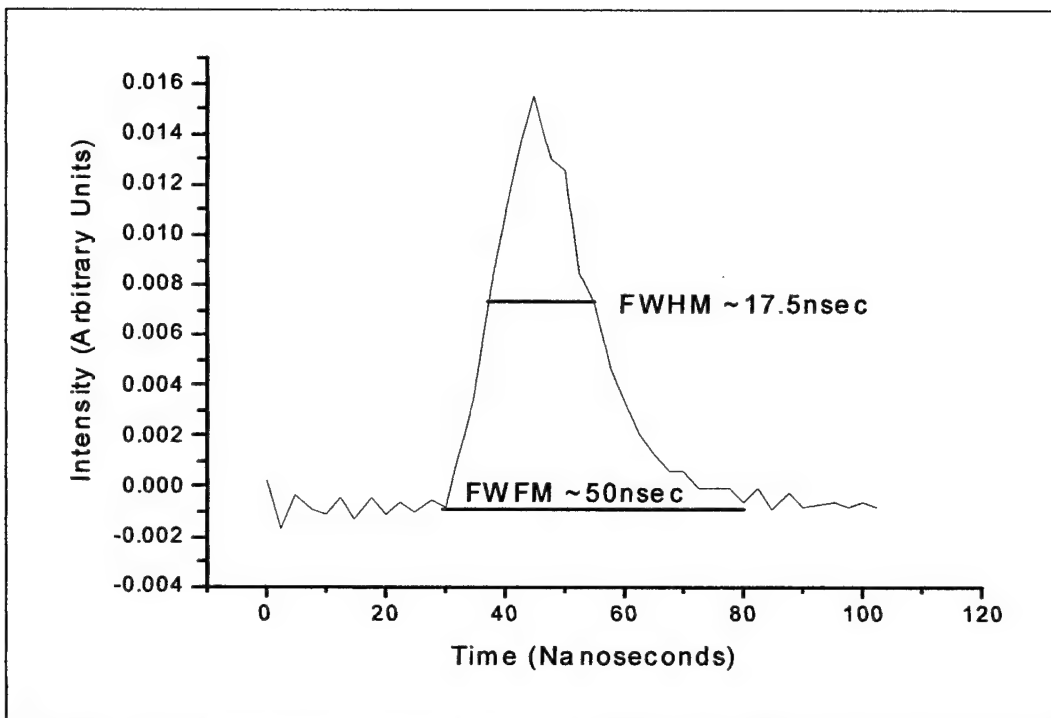


Figure 3.7. Temporal Profile of the Laser Pulse. As observed through oscilloscope in the experimental arrangement.

The oscilloscope recorded noise whenever the YAG pump laser was in operation. The noise is most likely radio-frequency noise from the YAG firing circuits coupled into the electronics of the measurement system (see Figure 3.8). The noise appears in the trace prior to the pre-trigger, and for a short time thereafter (usually 12-20ns). The noise was varying in intensity and in its temporal distribution. Averaging over several thousand sweeps did not eliminate the noise from the data (i.e. its temporal profile did not change during the course of the averaging), yet all attempts at removing the noise by digital filter methods failed. Several attempts were made during the course of the experiment to minimize and eliminate the noise source by electrical grounding, faraday caging critical components, and physically repositioning equipment around the laboratory. Initially, the source of the noise disappeared but returned later and was observed in some data sets.

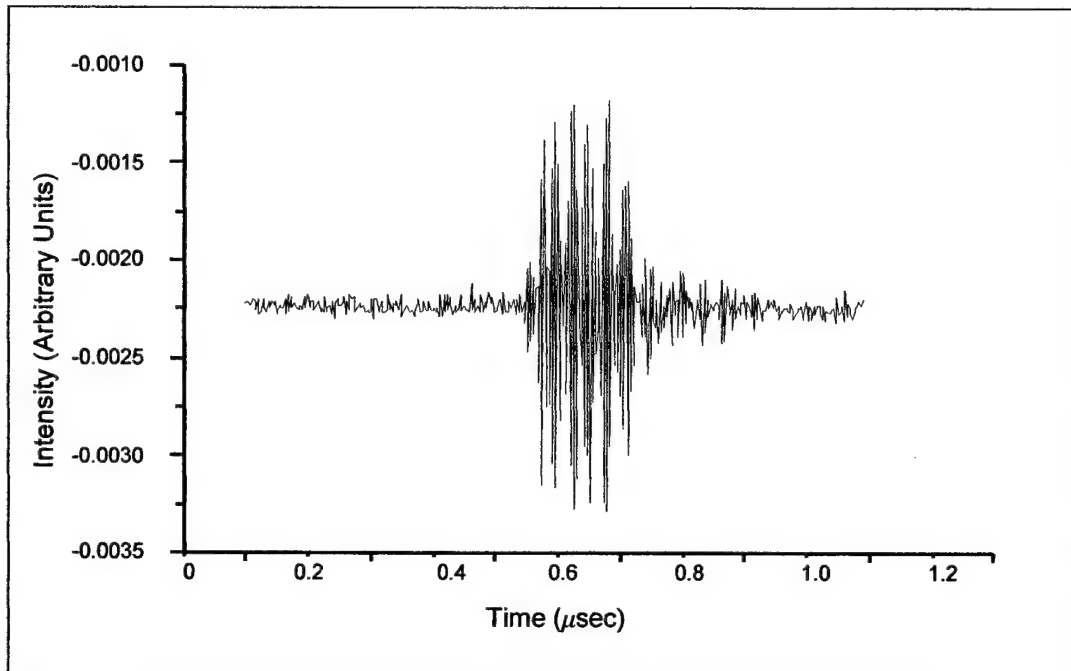


Figure 3.8. Radio-Frequency Noise Observed by Oscilloscope.

Some of the fluorescence data, therefore, is tainted by radio frequency noise. The effect of this noise is negligible for large amplitude fluorescence spectra of considerable lifetime (such as the lower vibrational levels). The noise is damaging, however, for higher vibrational levels that have less signal intensity and drastically larger decay rates.

3.4 Obtaining Fluorescence Data Fluorescence data are obtained systematically throughout the data acquisition of all buffer gasses to mitigate the propagation of systematic errors. The process of preparing the fluorescence cell has been discussed previously in this chapter. Once the cell has proper vapor pressures of bismuth and a stable pressure of buffer gas, the acquisition of data begins. The pressure, laser intensity, crucible power supply, photomultiplier tube voltage, and setting of the oscilloscope are all strictly maintained during the course of a data set. Only the pressure of the cell is

changed during an entire buffer gas characterization by manipulation of the buffer gas inlet valve and the vacuum pump feed valve. The reproducibility of the system characteristics over several days of experimentation is necessary to accurately compare data obtained from different vibrational levels and different buffer gas species.

After the fluorescence data is averaged on the LeCroy 9450 digital oscilloscope, the data file is transferred by serial port to an acquisition computer in the laboratory. The data file is imported into a spreadsheet that enables TableCurve software to extract the data. The method of sectioning data to obtain decay rate information is a potential source of systematic error. Therefore, the sectioning method was carefully scrutinized for its validity and accuracy and applied strictly to all fluorescence data. (See the discussion of errors in Appendix A).

3.4.1 Observation of Multiple Fluorescence Lifetimes. Because of the overlapping of rotational structures between different vibrational levels, as reported in spectrally resolved LIF experiments (Dolezal, to be published), the pump laser may populate vibrational levels other than the intended level. The fluorescence of two or more vibrational manifolds may be apparent in the acquired data. If the manifolds experience decay at different lifetimes, the data will not appear as a single exponential but as a sum of exponentials. Extraction of the decay lifetime of the intentionally pumped level will be a much more difficult task than with observation of one lifetime. Accordingly, a single exponential fit to a sum of exponentials may be acquired but with significant error in the reported lifetime. A summary of errors (Appendix A) demonstrates that these single exponential fits will still provide accurate quenching rates when extrapolated from a Stern-Volmer plot.

Prevention or mitigation of multiple-level pumping is still advantageous to the experiment and can be accomplished most assuredly by increasing the spectral resolution of the laser source to pump a specific J level that has minimal overlap with a J level from any other vibrational manifold (see Figure 3.9). Such an experiment will be reviewed in Chapter V. For this experiment, such spectral resolution was not practical and the method employed to minimize the effect of multiple level pumping was to pump along the desired vibrational manifold slightly lower in wavenumber from the band-head (towards higher J values), thereby increasing the distance from other bandheads of other vibrational manifolds. Because of the non-linear rotational structure of a vibrational manifold, the ratio of absorption into the primary level versus into secondary levels is significantly reduced.

Multiple-level pumping is not the only circumstance that generates a series of exponentials in fluorescence decay. V-T transfer is also prevalent in this collisional study and population of higher and lower states than the pumped vibrational manifold is possible (and more probable than multiple-level pumping). Unfortunately, it is impossible to find a level that one can be assured of is free of V-T transfer and multiple-level pumping and still is useful in this analysis.

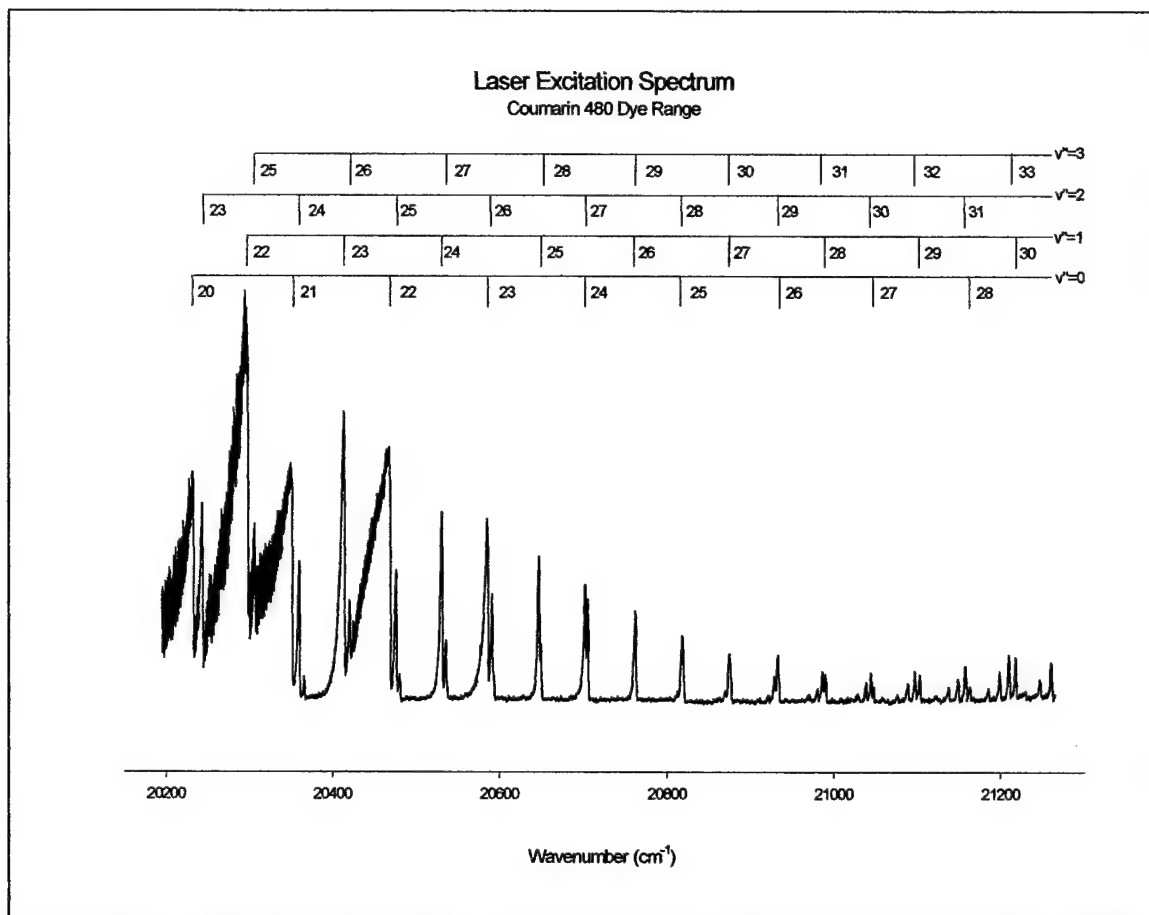


Figure 3.9. Laser Excitation Spectra and Vibrational Level Assignments (Dolezal, 1999).

But, since the data to be obtained is at vibrational levels at and around predissociation, increasing vibrational levels will bring about greatly increasing decay rates purely by the implementation of spontaneous and collisional predissociation. A lower state fluorescence decay observation may contain the higher vibrational level decays, but these will decay to negligible populations well before the lower state fluorescence has significantly diminished. Thus, when the data is sectioned appropriately to remove the initial short lifetime fluorescence spectra, all that remains is a long lifetime spectra of predominantly the primary fluorescence decay of interest.

3.4.2 Mathematical Method Used To Extract Fluorescence Data. If fluorescence decay contains emissions from more than one level, mathematical methods may be employed to extract useful, accurate information from a sum of exponentials. The best option available for this experiment is to generate a lifetime at a level that is either not a product of multiple level pumping, or is in some other way not significantly multiple exponential. This lifetime can be used in a multiple exponential fit when the lifetime is reasonably expected to be one of the terms in the sum of exponentials.

For example, a decay rate is recorded for level A and is determined to be a single exponential lifetime:

$$I=I_0 \text{Exp}(-A*t) \quad (3.4.1)$$

If a measured decay rate B is to be analyzed, the fit will consist of a sum of exponentials such as:

$$I= I_0\{E \text{Exp}(-A*t) + F \text{Exp}(-B*t)\} \quad (3.4.2)$$

The coefficients E and F are the relative proportions of fluorescence in the data and contain valuable information about the population of the two states A and B. A will be held constant at the pre-determined value and the variable B will be fit to the new fluorescence curve.

The approximation of fitting the decay curves to a sum of a few levels is appropriate if the relative magnitudes of the coefficients of the secondary exponentials are small with respect to the primary (or fitted) exponential. For this analysis, a single exponential fit is obtained for all vibrational levels. For levels $v'=22$ through $v'=25$ a progression of multiple exponential fits is obtained to more accurately characterize the fluorescence decay. $v'=22$ is extracted purely by a single exponential (though it should

contain some V-T populations of neighboring levels and some minor population from multiple-level pumping) and this decay is established as a baseline for the next series of fits. The extraction of quenching rates from $v'=22$ are still accurate as will be described in Appendix B.

The next vibrational level, $v'=23$, is fitted to a double exponential as in [3.4.2]. Characterization of each buffer gas occurred at discrete intervals of pressure. Within each pressure increment, fluorescence was observed for all four vibrational levels. Therefore, the pressure in the fluorescence cell was relatively constant during each interval of pressure, and the lifetime of $v'=22$ at each discrete pressure can be reasonably applied to the double exponential fit (that is to say, there was very little pressure-dependent linear departure of the decay rate of $v'=22$ from that observed in the $v'=22$ fluorescence to what would be observed in the $v'=23$ fluorescence since the pressures remained the same).

Single and multiple exponential fits were conducted for all buffer gases for $v'=24$ and $v'=25$. All fluorescence decay rates observed (for example, see Figure 3.10) were on the order of the temporal resolution of the experiment and the temporal width of the dye laser pulse. Analysis of the data is, therefore, prone to inaccuracy and all quenching rates for the last two levels have been discarded.

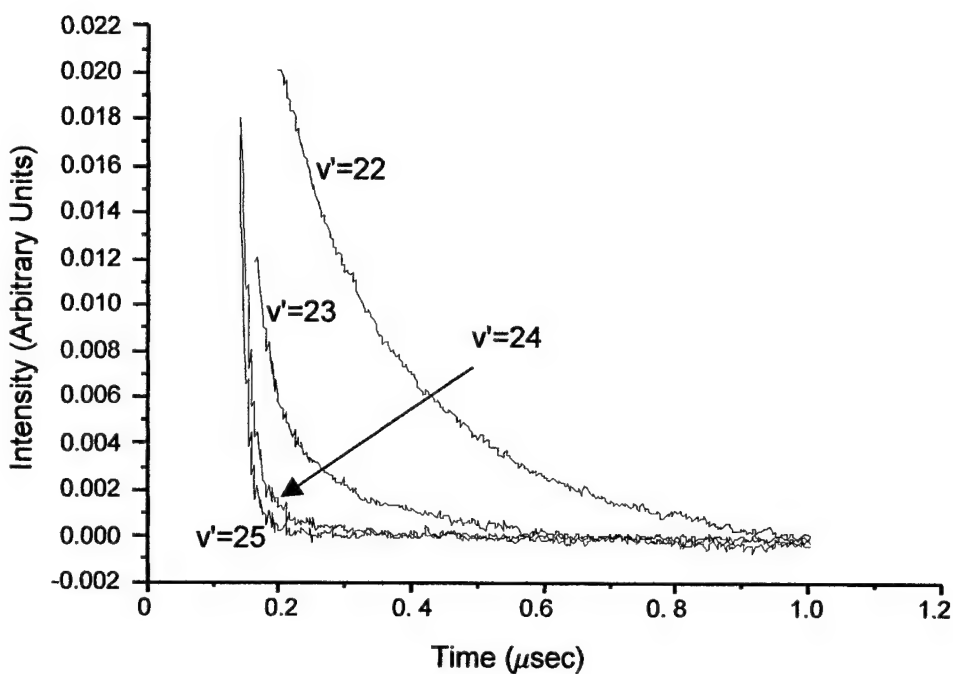


Figure 3.10. Fluorescence Decay Curves for Helium Buffer Gas, $\sim 3000\text{mTorr}$, $v'=22$ through $v'=25$.

A thorough description of the experimental apparatus has been presented along with the results of the system alignment and calibration. The process of obtaining fluorescence decay measurements has been discussed along with the mathematical methods necessary to accurately extract the pressure dependent decay rates.

IV. Results and Discussion

4.1 Introduction This experiment supplements extensive research in this area by Michael Dolezal, who performed spectrally resolved, temporally resolved fluorescence of vibrational levels $v'=8$ through $v'=39$ using out-gassed vapors at pressures from 15-150mTorr. A complete set of predissociated rate constants were reported along with three sets of excitation spectra. For this study, temporally resolved laser induced fluorescence was observed for vibrational levels $v'=18$ through $v'=25$ with six buffer gasses at pressures ranging from 500mT to 5 Torr. Electronic quenching rates have been determined and are reported.

4.2 Electronic Quenching of $\text{Bi}_2\text{A}(\theta^+_u)$

4.2.1 Quenching by Helium of Vibrational Levels $v'=18, 19, 20, 21$. Temporally resolved fluorescence was first obtained for the four lower vibrational levels of the A state ($v'=18, 19, 20, 21$) using helium buffer gas and C-500 laser dye. Fluorescence decay was observed at 5000 sweeps of the oscilloscope with pressure variances of less than 0.5%. The exponential lifetimes were extracted for long (thermalized) times with extraction from 800ns to the end of the data at 5000ns (Figures 4.1 and 4.2). The peak of the fluorescence pulse was observed at 565ns when the oscilloscope was triggered at 10.2% (510ns). This results in the first 235ns of the fluorescence pulse being eliminated from observation by the exponential fit routines. The high signal to noise ratio yielded r^2 values (coefficients

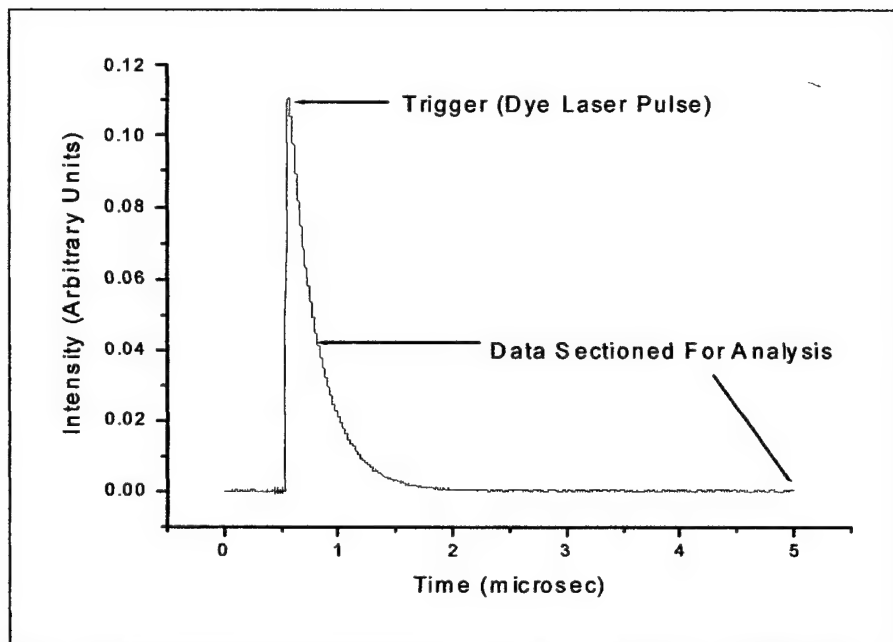


Figure 4.1. Typical Fluorescence Curve, Helium Buffer Gas, ~3000mTorr, $v'=18$.
Range of data sectioned for analysis is indicated.

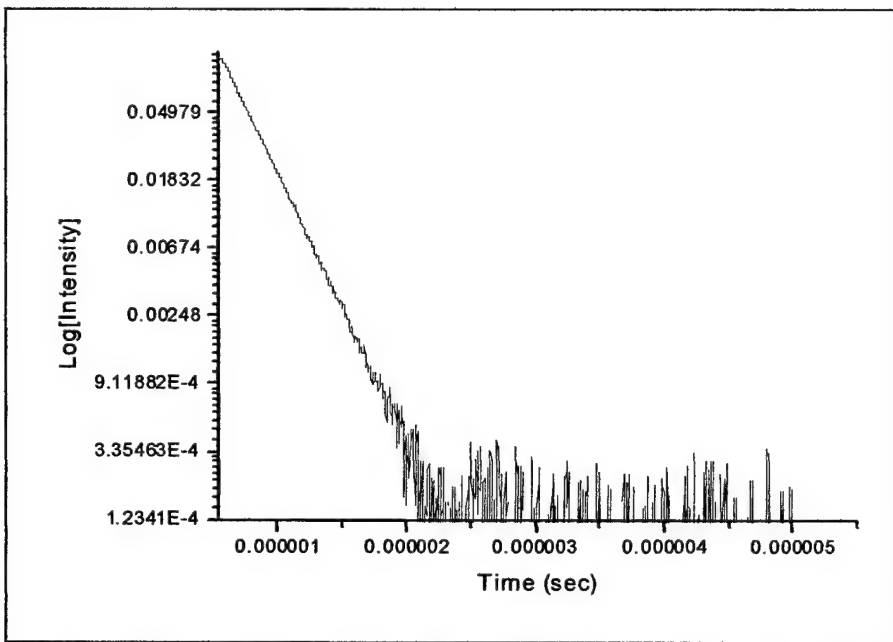


Figure 4.2. Logarithm Plot of Fluorescence Curve.
The data shown is the same as in figure 4.1

of determination) of typically 0.999+. Only single exponential fits were made to this data set (Appendix A). A typical residual plot is shown in figure 4.3.

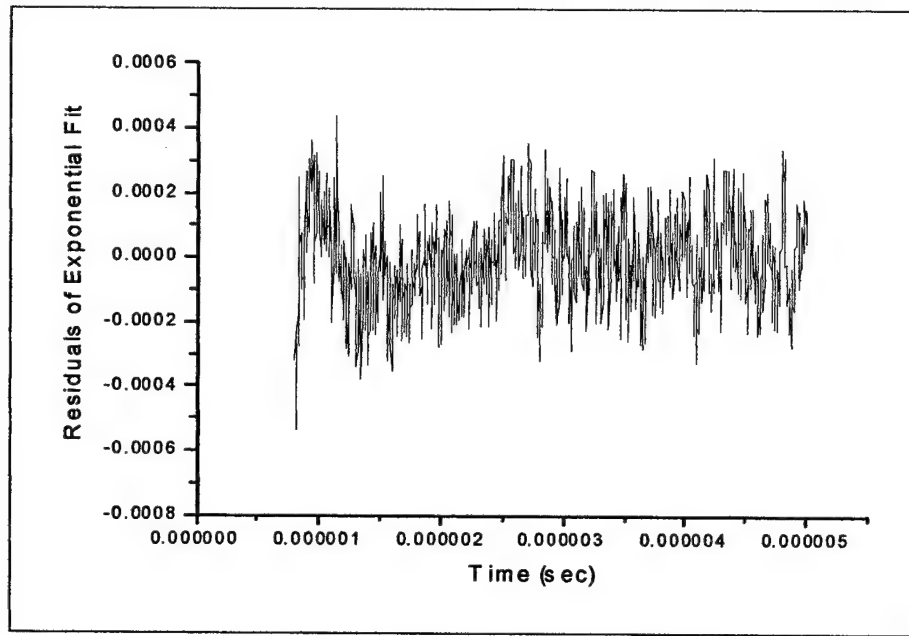


Figure 4.3. Residuals to Exponential Fit.
The data set used is the same as in figure 4.1.

The electronic quenching rates were obtained via Stern-Volmer plots (equation 2.3.26) and are displayed in figures 4.4-4.7. There is very little difference in the electronic quenching or collision free decay rate for these levels and a combined plot is shown in figure 4.8. A simple average for these quenching rates was performed to yield the result of $712.62 \text{ mTorr}^{-1}\text{sec}^{-1}$ ($2.21 \times 10^{-11} \text{ cm}^3 \text{ molecules}^{-1} \text{ sec}^{-1}$). The collision free lifetimes of these levels should be free of the effects of spontaneous predissociation. A simple average of the collision free lifetime was performed with the result of $1.7 \pm 0.2 \times 10^6 \text{ sec}^{-1}$. This is comparable to the reported radiative rate of $1.6 \times 10^6 \text{ sec}^{-1}$ (Blondeau, 1980; 246).

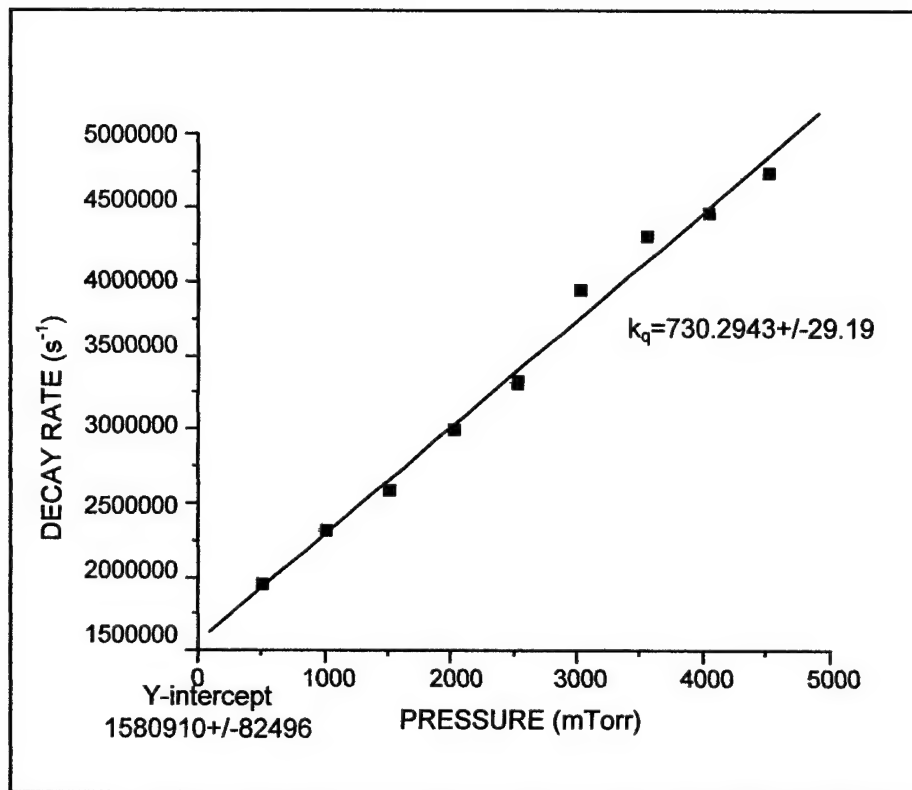


Figure 4.4. Stern-Volmer Plot, Pressure versus Decay Rate, for He buffer gas, $v'=18$

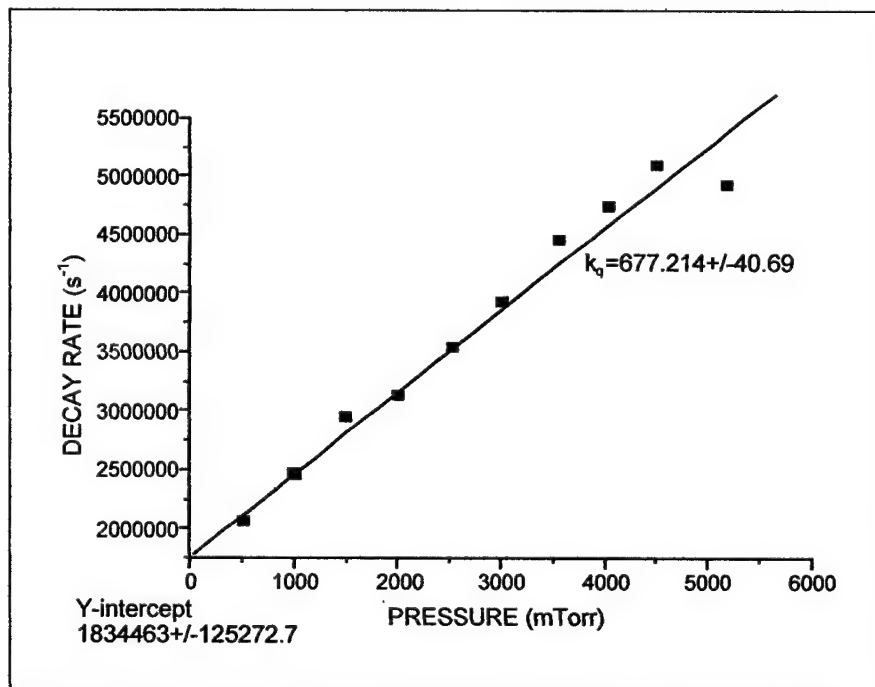


Figure 4.5. Stern-Volmer Plot, Pressure versus Decay Rate, for He buffer gas, $v'=19$

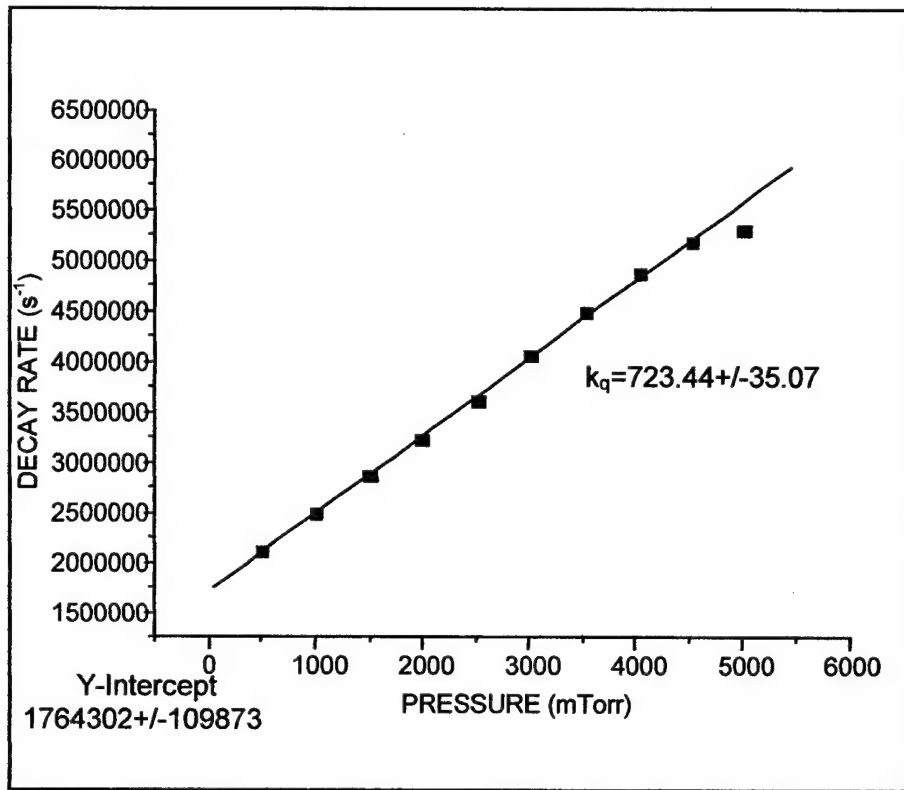


Figure 4.6. Stern-Volmer Plot, Pressure versus Decay Rate, for He buffer gas, $v'=20$.

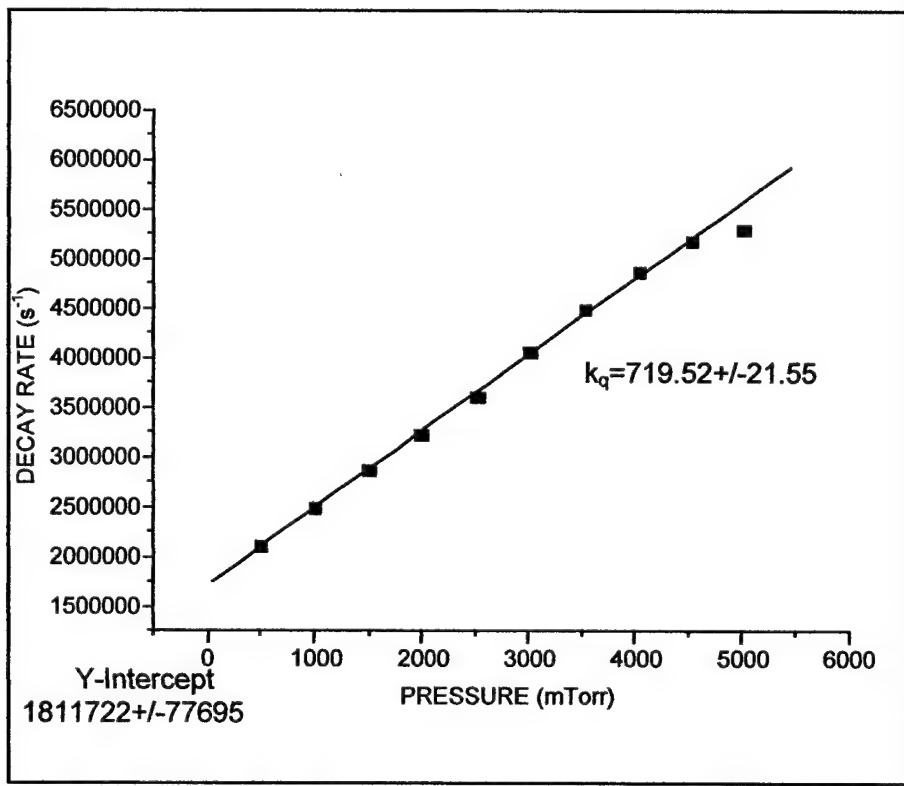


Figure 4.7. Stern-Volmer Plot, Pressure versus Decay Rate, for He buffer gas, $v'=21$.

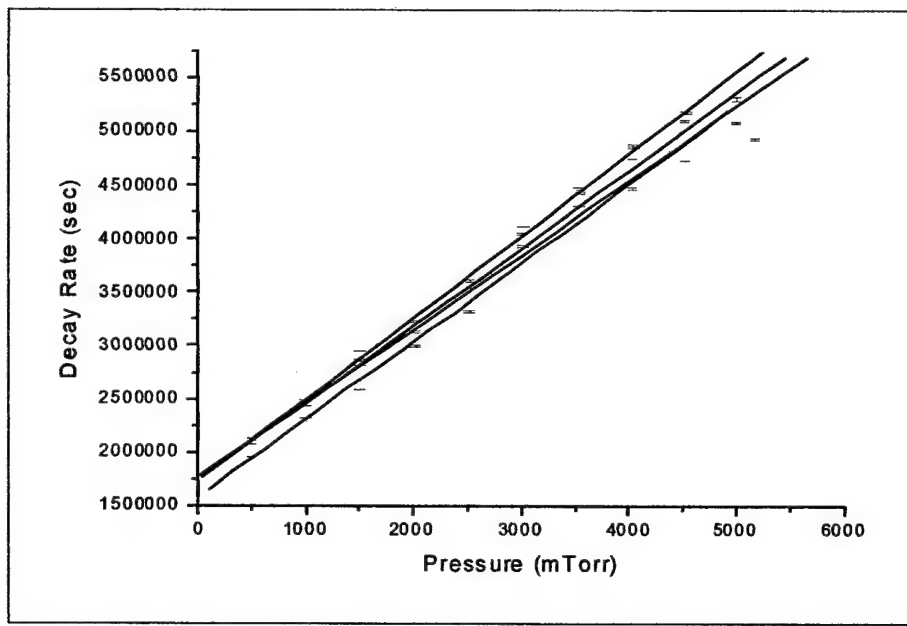


Figure 4.8. Stern-Volmer Plot, He buffer gas, $v'=18, 19, 20, 21$.

4.2.2 Quenching by Helium of Vibrational Levels $v'=22, 23, 24, 25$. Fluorescence

was then observed for the four higher vibrational levels ($v'=22, 23, 24, 25$), using C-480 laser dye, observation at 5000 sweeps, with pressure variance of less than 0.5%. The oscilloscope was set to 0.1 μ sec/div with the original 10.2% pre-trigger left the same. The oscilloscope was then triggered at 102ns, with fluorescent peak observed at 135ns. Increased decay rate due to predissociation was sudden at $v'=23$. Decay rate increased dramatically through $v'=25$.

4.2.2.1 Single Exponential Fits to Observed Fluorescence. Exponential fits were performed initially using single exponentials. The data sets for $v'=22$ were sectioned to 200ns and out to the end of the data at 1000ns. The data sets for $v'=23$ were sectioned to 165ns in order to recover more of the fluorescence observation. The data sets for $v'=24$ were sectioned to 145ns and for $v'=25$ at the peak of the fluorescence at 135ns. Sectioning of the data any further severely restricts the ability of the curve-fitting algorithm to extract an exponential decay, as the fluorescence decay of $v'=25$ at

5000mTorr, for example, returns to baseline before 250ns. Though a high signal to noise ratio should have been maintained from the previous data set of levels 18-21, the observed data appears noisy, particularly for $v'=23$, with r^2 of the exponential fits ranging from 0.947 to 0.993.

The electronic quenching rate for $v'=22$ was identical to the rates observed for $v'=18$ through $v'=21$ (figure 4.6). The collision free decay rate, however, was almost double. The radiative lifetime has not changed appreciably with the change in vibrational level (Blondeau, 1980; 246). The rise in collision free decay rate is the result of spontaneous predissociation at this higher vibrational level. The rate of spontaneous predissociation can be estimated simply by subtracting the radiative decay rate from the observed collision free decay rate. The resulting predissociated rate is approximately $1.27 \times 10^6 \text{ sec}^{-1}$. The J-dependent $k'_{pd}(J)$ value for $v'=22$ as determined by Dolezal is $\sim 2000 \text{ sec}^{-1}$. An estimate in the rotational level can be extracted by dividing the rate k_{pd} observed here by the $k'_{pd}(J)$ value and then taking the square root.

$$k_{pd} = \Gamma_0 - \Gamma_{rad} = k'_{pd} J(J+1) \approx k'_{pd} J^2 \quad (4.1)$$

$$\sqrt{\frac{k_{pd}}{k'_{pd}}} \approx J \quad (4.2)$$

$\Gamma_0 \equiv$ experimentally determined collision-free decay rate

$\Gamma_{rad} \equiv$ reported radiative decay rate

$k_{pd} \equiv$ calculated predissociative decay rate

The resultant J value of 25 is certainly reasonable upon consideration of the location along the vibrational manifold that the dye laser is pumping.

The Stern-Volmer plot of the single exponential fits to $v'=23$ yields a negative quenching rate (figure 4.7). This is not feasible for high pressures where the vibrational state is thermalized and must be rejected. An analysis using multiple exponentials must be conducted and compared to the single exponential fits before reporting the quenching rates and collision free decay rates.

4.2.2.2 Multiple Exponential Fits to Observed Fluorescence. Stern-Volmer plots for the vibrational levels 23, 24, and 25 under single exponential fits yielded r^2 values of 0.415, 0.336, and 0.395 respectively. There was very little linear correlation between the data points. For $v'=22$, however, the Stern-Volmer plot yielded a linear fit with r^2 of 0.962. Far better linear fits were obtained when the data points were extracted via multiple exponential fits. Coefficients of determination, r^2 , of 0.876, 0.804, and 0.908 were obtained for levels 23, 24, and 25, respectively. The ability to obtain better linear correlation to the data points is indicative of the strength of the multiple exponential fit routine (Figures 4.10, 4.11, and 4.12). For the purpose of analysis of the electronic quenching by helium, only the multiple exponential fits will be reported.

The collision free decay rates of the multiple exponential fits increased dramatically from 2.83E+6 for $v'=22$, to 2.38E+7 for $v'=23$, and as high as 8.72E+7 for $v'=25$. The radiative rate has been observed to remain the same throughout the levels under investigation. The rapid rise in collision free decay rate is the result of spontaneous predissociation as discussed in [4.2.2.1]. An analysis similar to that used in the previous section was conducted and is reported here in Table 4.1.

All the approximate rotational values are reasonable pump locations along the vibrational manifold. The collision free decay rates and approximate rotational levels

Table 4.1. Collision Free Lifetimes and Approximate Rotational Levels, He Buffer Gas.

v'	Collision Free Lifetime (Γ_0) (10^6 s $^{-1}$)	Radiative Rate (1/ τ_r) (10^6 s $^{-1}$)	Predissociative Rate (k_{pd}) (10^6 s $^{-1}$)	Predissociative Rate Coefficient (k_{pdJ}) (s $^{-1}$)	Approximate Rotational Level (J)
22	2.84±0.15	~1.56	1.27	2000	25
23	23.9±0.9	~1.56	22.3	14000	40

should not change with the introduction of different buffer gas species. Thus, these values will serve as useful guidelines for the interpretation of the error in Stern-Volmer linear fits for future data.

The observed electronic quenching rates for $v'=23$, 24, and 25 are much greater than for vibrational levels 22 and below. While quenching rates for the lower levels are around 700 mTorr sec $^{-1}$, for the upper three levels, quenching rates of 1589 to 4305 mTorr sec $^{-1}$ were observed. All decay rates observed for helium buffer gas at $v'=24$ and $v'=25$ are on the order of the temporal pulse width of the dye laser. The extracted data is, therefore, prone to large error, and only data for vibrational levels 18 through 23 will be reported in this thesis. The electronic quenching rates for helium buffer gas are reported in Table 4.2. All other buffer gasses under study experience decay rates at a higher rate than helium and data was summarily discarded at vibrational levels above $v'=23$.

Table 4.2. Electronic Quenching Rates by Helium Buffer Gas.

v'	Quenching Rate k_q (mTorr sec $^{-1}$)	Standard Error (mTorr sec $^{-1}$)	Quenching Rate $k_q \times 10^{13}$ k_q (cm 3 molec $^{-1}$ sec $^{-1}$)	Standard Error $\times 10^{13}$ (cm 3 molec $^{-1}$ sec $^{-1}$)
18	730.29	±29.19	226.75	±9.063
19	677.21	±40.69	210.27	±12.63
20	723.44	±35.07	224.63	±10.89
21	719.52	±21.55	223.41	±6.676
22	732.16	±51.77	227.33	±16.07
23	3367	±447	1045	±139

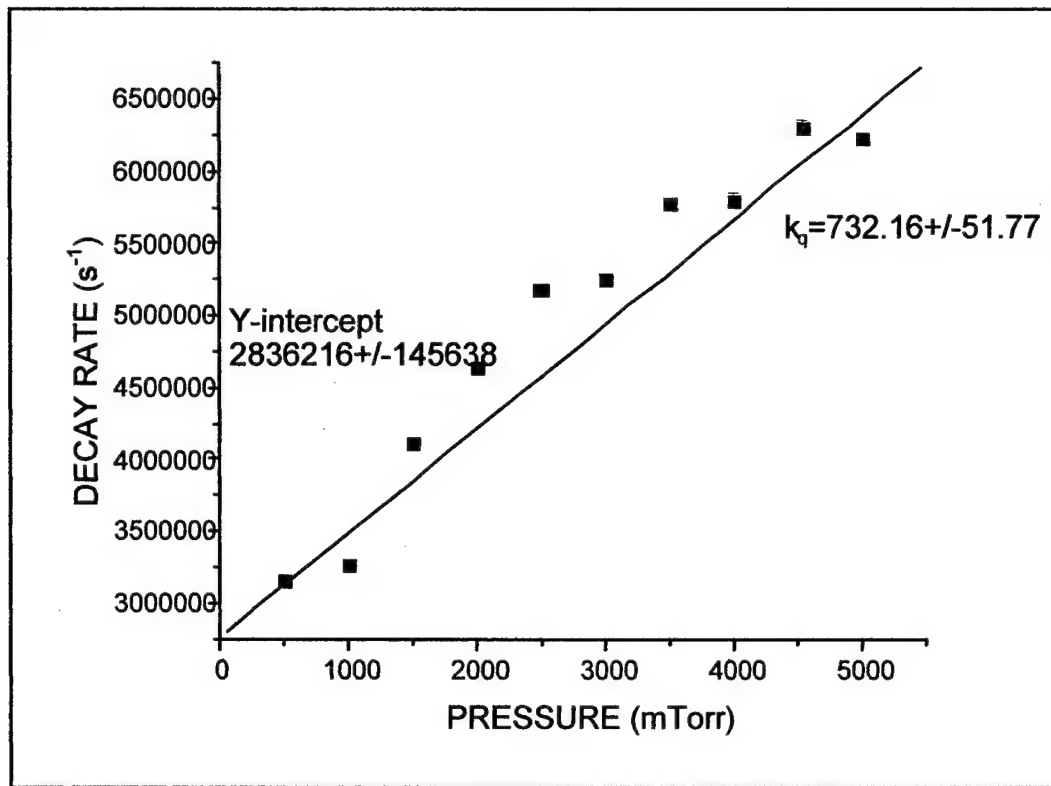


Figure 4.9. Stern-Volmer Plot, Single Exponential Fit, He buffer gas, $v' = 22$.

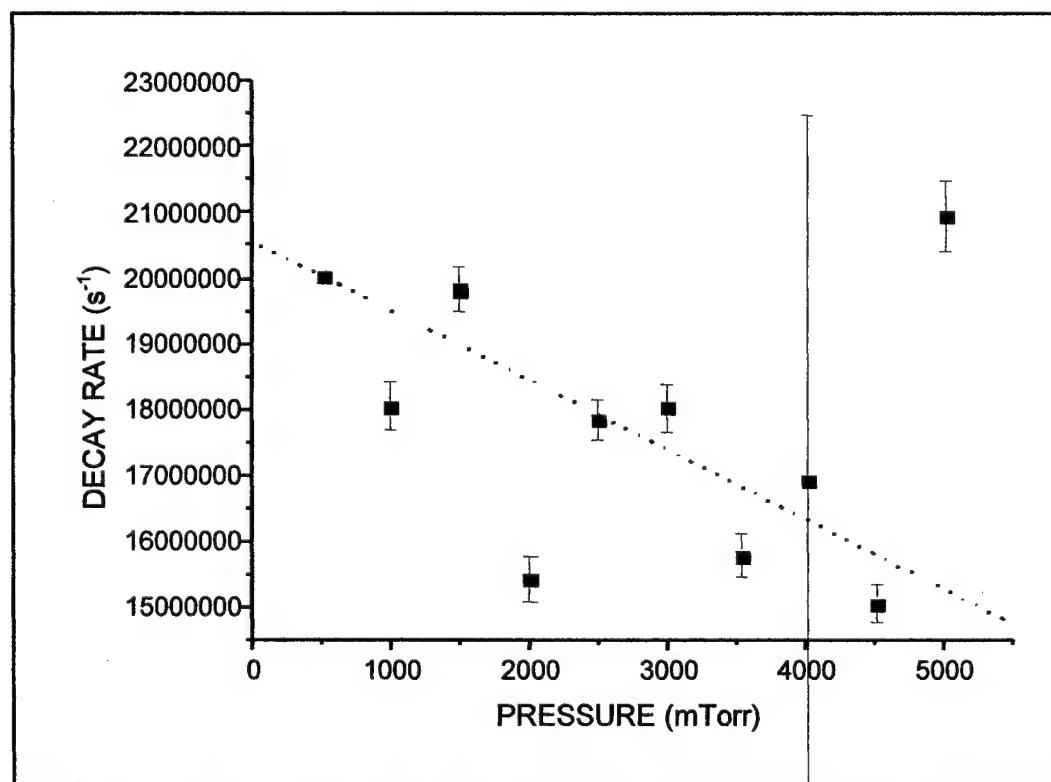


Figure 4.10. Stern-Volmer Plot, Single Exponential Fit, He buffer gas, $v' = 23$.

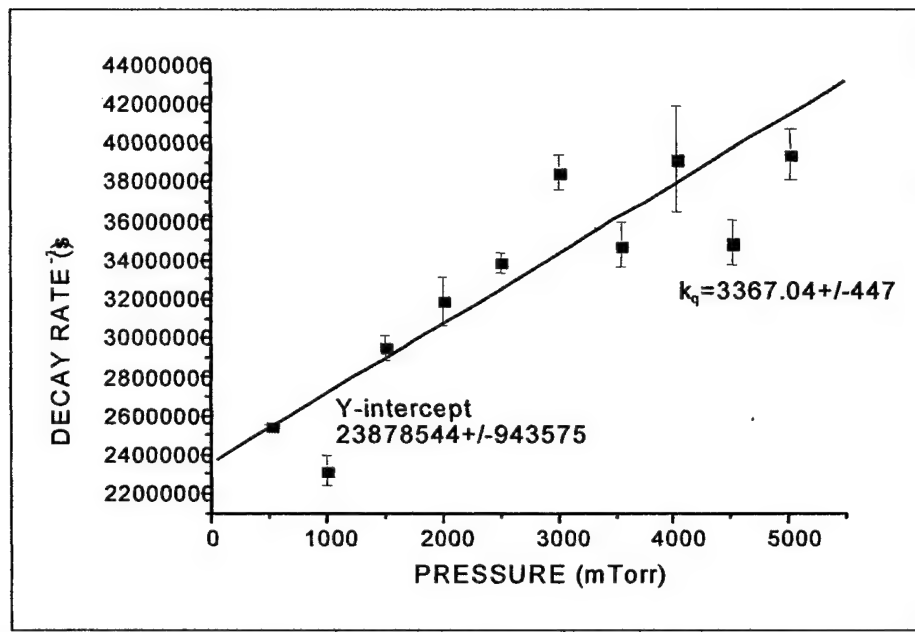


Figure 4.11. Stern-Volmer Plot, He buffer gas, $v'=23$, Double Exponential Fit.

4.2.3 Quenching by Neon of Vibrational Levels $v'=22, 23$. Electronic quenching by neon buffer gas was sectioned at the same location in the oscilloscope trace and observed at the same oscilloscope settings as before for with helium buffer gas, with the only exception that averages were obtained for 2000 sweeps as opposed to 5000. The decreases in sweeps results in a lower signal to noise ratio in the observed fluorescence. As before, the data sets for $v'=22$ were sectioned to 200ns and out to the end of the data at 1000ns. The data sets for $v'=23$ were sectioned to 165ns in order to recover more of the fluorescence observation. These settings remained the same throughout the rest of the experiment for all remaining buffer gasses.

4.2.3.1 Single Exponential Fits to Observed Fluorescence. The single exponential fits obtained for neon were quite good, with the coefficients of determination for $v'=22$ of the order of those obtained for helium buffer gas (0.994-0.999+). The range of r^2 values for $v'=23$ were similar to those obtained for $v'=22$, with $v'=23$ containing a larger

number of values at the bottom of the range indicating less consistent correlation with single exponential fits.

The Stern-Volmer plot for $v'=23$ (Figure 4.13) indicates a negative quenching rate. As before, data of this sort is considered erroneous at these high pressures and is discarded. The Stern-Volmer plot for $v'=22$, Figure 4.12, provided a linear fit with $r^2=0.968$, collision-free decay rate comparable to the data obtained for helium, but with a quenching rate significantly higher than that obtained for helium at the same level, $903\pm62\text{mTorr sec}^{-1}$. Analysis of the multiple exponential fits will need to be conducted before a determination of the electronic quenching rate of neon buffer gas at $v'=23$.

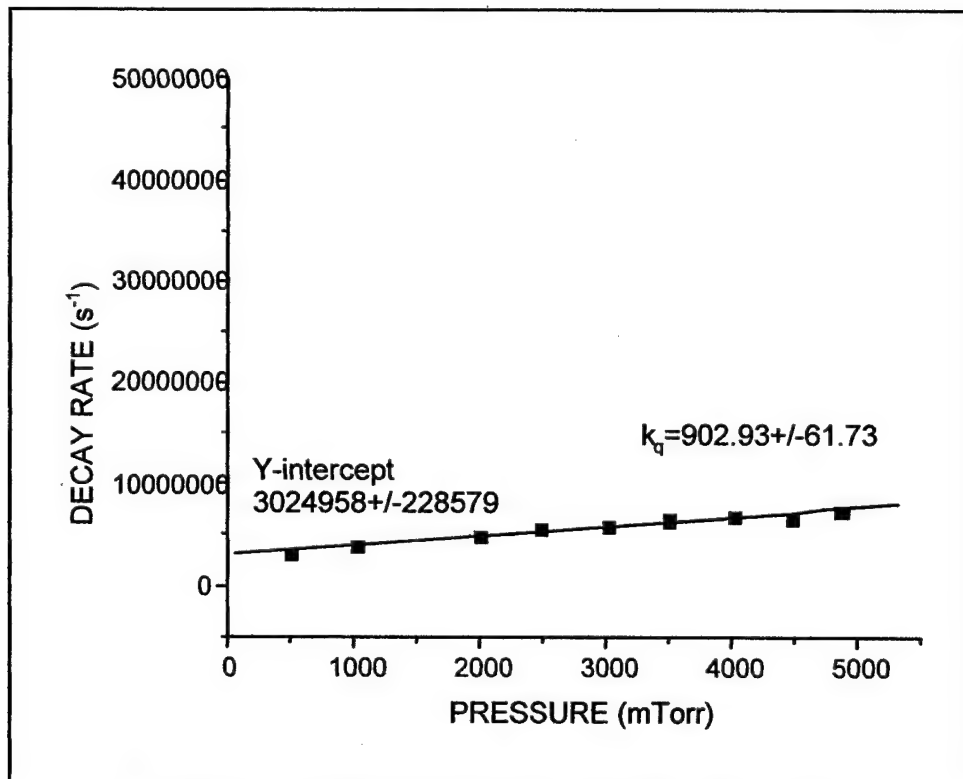


Figure 4.12. Stern-Volmer Plot, Ne buffer gas, $v'=22$

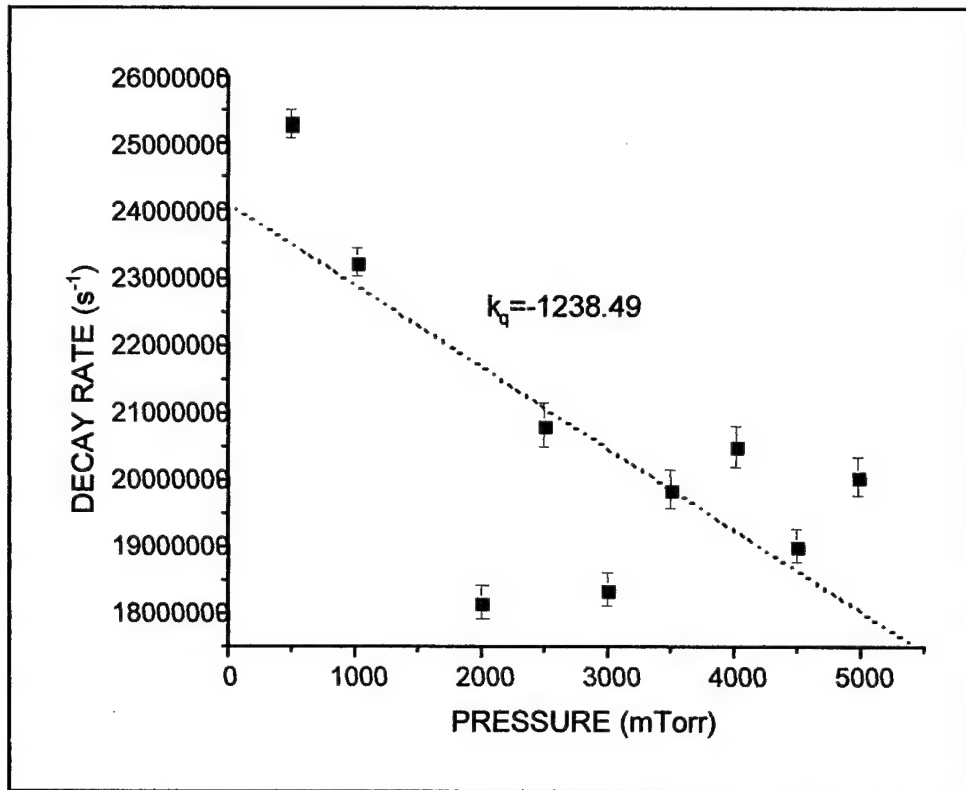


Figure 4.13. Stern-Volmer Plot, Ne buffer gas, $v'=23$

4.2.3.2 Multiple Exponential Fits to Observed Fluorescence. Multiple exponential fits were obtained using the same methods discussed with helium buffer gas in section [4.2.2.2]. The approximate rotational levels extrapolated from the collision free decay rates of the linear Stern-Volmer fits were within 1-2 rotational levels of those extrapolated from the helium data set (see Table 4.3). The quenching rates are reported in table 4.4.

Table 4.3. Collision Free Lifetimes and Approximate Rotational Levels, Ne Buffer Gas.

v'	Collision Free Lifetime (Γ_0) (10^6 s ⁻¹)	Radiative Rate ($1/\tau_r$) (10^6 s ⁻¹)	Predissociative Rate (k_{pd}) (10^6 s ⁻¹)	Predissociative Rate Coefficient (k_{pdj}) (sec ⁻¹)	Approximate Rotational Level (J)
22	3.02 ± 0.23	~ 1.56	1.46	2000	27
23	25.8 ± 1.7	~ 1.56	24.2	14000	41

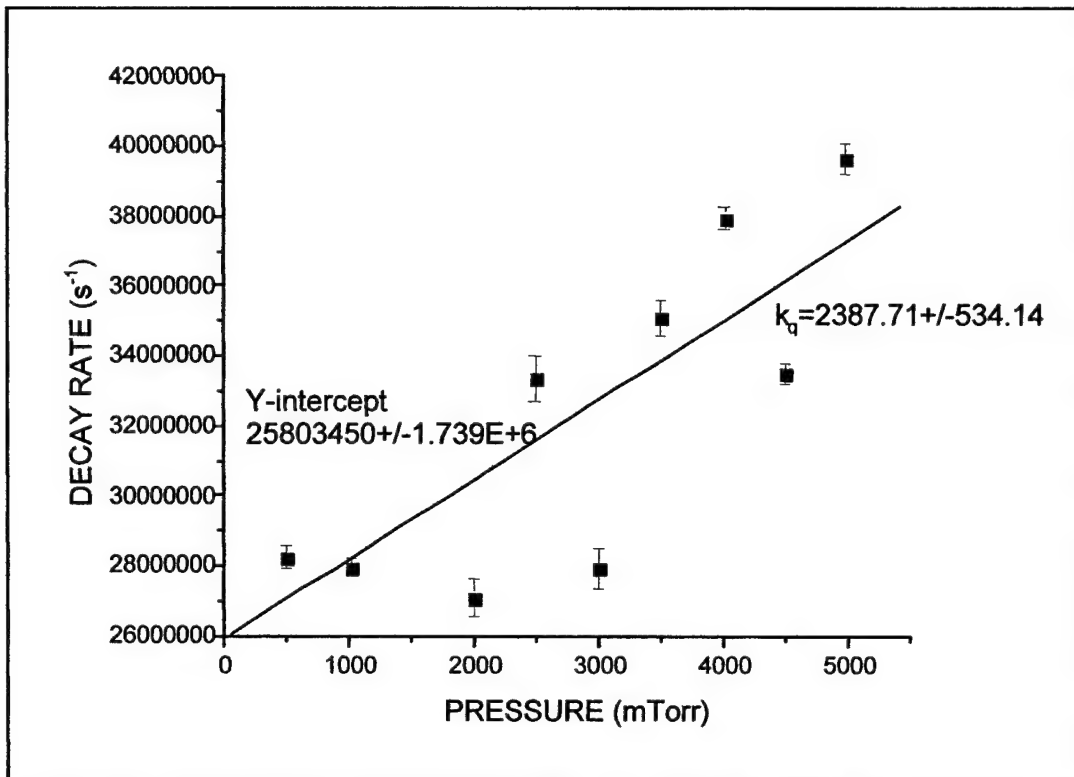


Figure 4.14. Stern-Volmer Plot, Ne buffer gas, $v'=23$, Double Exponential Fit.

Table 4.4. Electronic Quenching Rates by Neon Buffer Gas.

v'	Quenching Rate k_q (mTorr sec ⁻¹)	Standard Error (mTorr sec ⁻¹)	Quenching Rate $k_q \times 10^{13}$ k_q (cm ³ molec ⁻¹ sec ⁻¹)	Standard Error $\times 10^{13}$ (cm ³ molec ⁻¹ sec ⁻¹)
22	902.9	± 61.7	280.4	± 19.2
23	2387	± 534	741.2	± 165

4.2.4 Quenching by Nitrogen Dimers of Vibrational Levels $v'=22, 23$. The electronic quenching by diatomic nitrogen is unique for the buffer gasses studied in that its molecular structure supports V-V, vibrational to vibrational coupling, which may enhance the observed electronic quenching rates.

4.2.4.1 Single Exponential Fits to Observed Fluorescence. The single exponential fits $v'=22$ fluorescence data yielded coefficients of determination from 0.995-0.998+ with a linear Stern-Volmer fit of 0.975. The data for $v'=23$ was similar to neon with respect to the r^2 of its Stern-Volmer fit and slightly better than neon with respect to the r^2

values of the individual data points, but had inadequate linear correlation in the data, with a linear fit to the Stern-Volmer plot of $v'=23$ generating an r^2 of 0.558. Multiple exponential analysis will be necessary to extract the electronic quenching rates of the highest three levels.

The collision free lifetime of $v'=22$ was slightly higher than neon and helium. A corresponding approximate J value of 29 is obtained which is higher than J=25 obtained for helium at $v'=22$. This rise in collision-free decay rate cannot be attributed to the use of a different buffer gas and must be indicative of error in the extrapolation, or a systematic error in the conduct of the experiment. The electronic quenching rate is dramatically higher than helium or neon, 2586 ± 146 mTorr sec⁻¹. Since the molecular mass of nitrogen dimer at 28 amu is not appreciably larger than the atomic mass of neon, 20 amu, the increase in electronic quenching is likely due to the effect of V-V transfer.

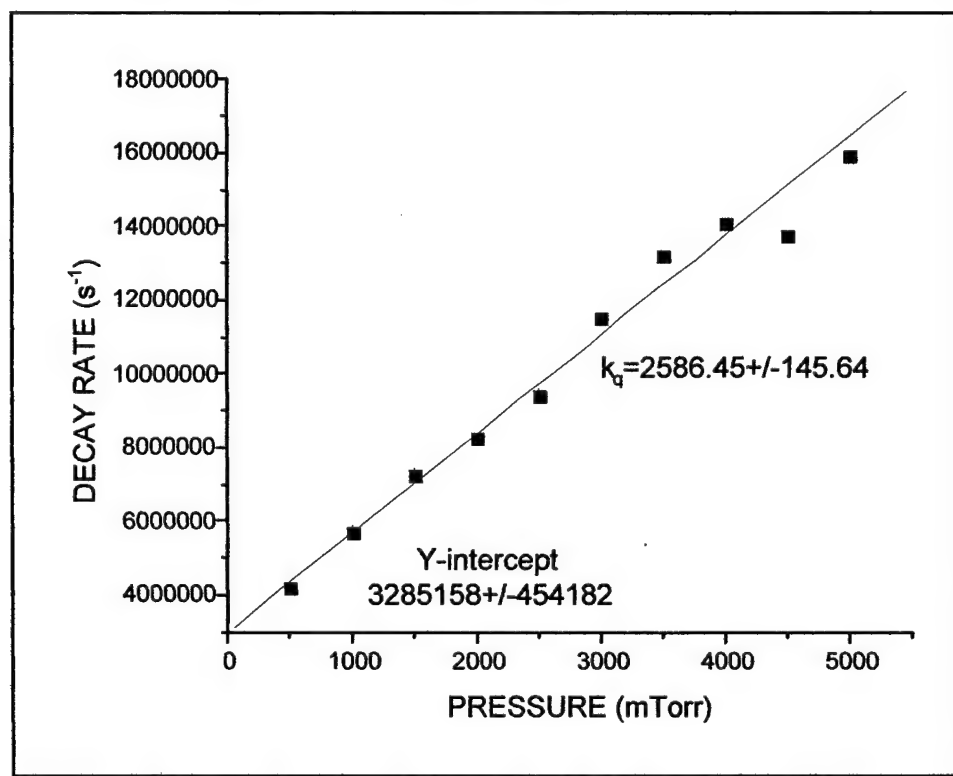


Figure 4.15. Stern-Volmer Plot, N_2 buffer gas, $v'=22$

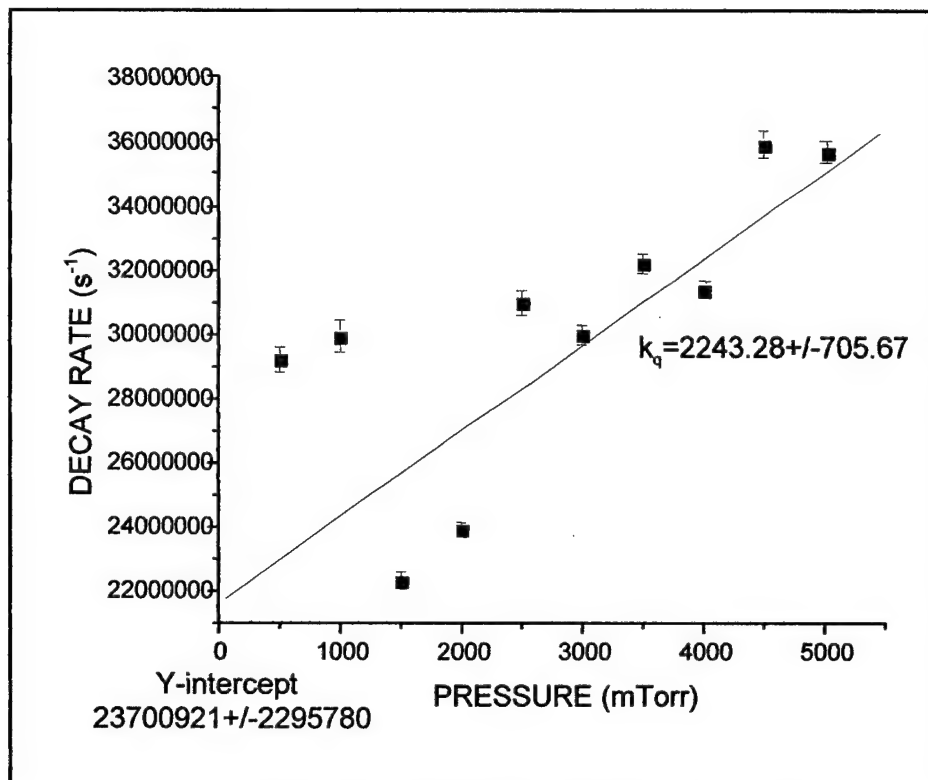


Figure 4.16. Stern-Volmer Plot, N₂ buffer gas, v'=23

4.2.4.2 Multiple Exponential Fits to Observed Fluorescence. Multiple exponential fits obtained for level 23 fared much better in terms of coefficients of determination than for single exponential fits, with an r^2 value of 0.7338 obtained for the linear fit to Stern Volmer plot. The collision free decay rates obtained from the fits provided approximate J-levels that were within 5 levels for v'=23. As reported in the previous sub-section, the approximate J-level for v'=22 was 4 levels higher than that estimated from the helium data set. The extrapolated linear fits are reasonable, although errors may be present in v'=22 and v'=23.

Table 4.5. Collision Free Decay Rate and Approximate Rotational Levels, N₂ Buffer Gas.

v'	Collision Free Decay Rate (Γ_0) (10^6 s^{-1})	Radiative Rate ($1/\tau_r$) (10^6 s^{-1})	Predisassociative Rate (k_{pd}) (10^6 s^{-1})	Predisassociative Rate Coefficient (k_{pd}) (sec^{-1})	Approximate Rotational Level (J)
22	3.29 ± 0.45	~ 1.56	1.73	2000	29
23	29.7 ± 3.4	~ 1.56	28.1	14000	45

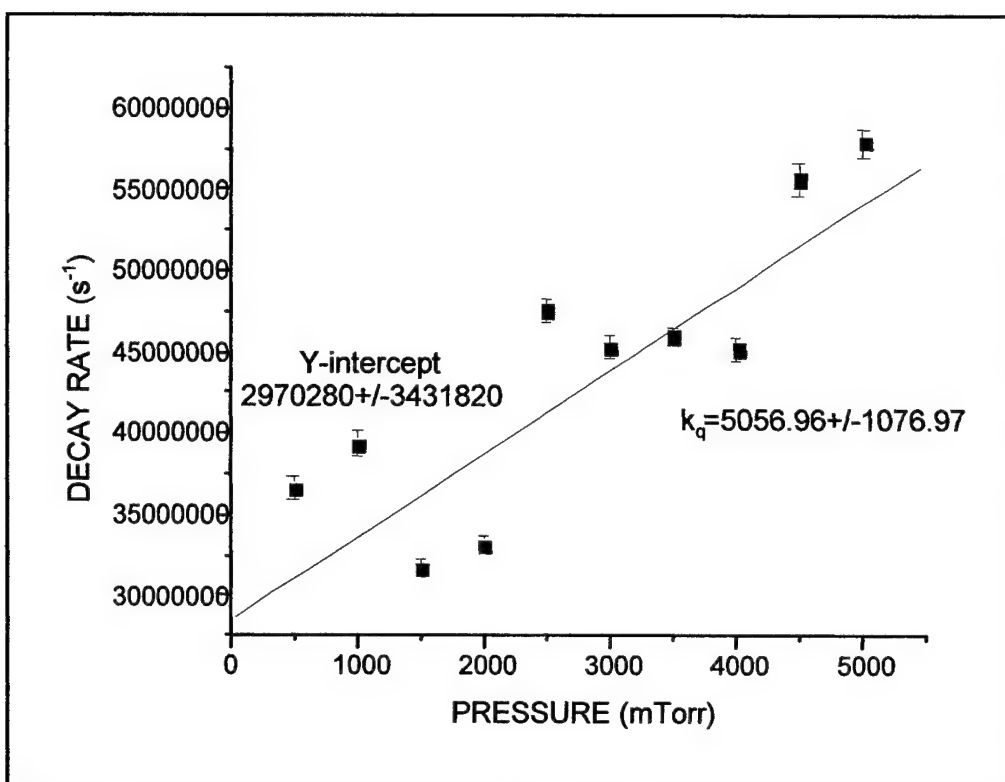


Figure 4.17. Stern-Volmer Plot, N₂ buffer gas, v'=23, Double Exponential Fit.

Table 4.6. Electronic Quenching Rates by Nitrogen Buffer Gas.

v'	Quenching Rate k _q (mTorr sec ⁻¹)	Standard Error (mTorr sec ⁻¹)	Quenching Rate k _q × 10 ¹³ k _q (cm ³ molec ⁻¹ sec ⁻¹)	Standard Error × 10 ¹³ (cm ³ molec ⁻¹ sec ⁻¹)
22	2586	±146	803.0	±45.3
23	5057	±1077	1570	±487

4.2.5 Quenching by Argon of Vibrational Levels v'=22, 23. The electronic quenching rates of helium, neon, and diatomic nitrogen have been previously reported. Their respective atomic (and molecular) masses are 4.0, 20.2, and 28.0 while argon is significantly higher at 39.9 amu. The effects of increasing atomic mass of the collision specie on the fluorescence decay should be evident beginning with argon, and continue with krypton (83.8 amu) and xenon (131.3 amu).

4.2.5.1 Single Exponential Fits to Observed Fluorescence. The single exponential fits to v'=22 were obtained with coefficients of determination ranging from 0.994-

0.999+, and fits to $v'=23$ had smaller values of r^2 but comparable to those obtained with helium. A linear fit to a Stern-Volmer plot of $v'=22$ produced an r^2 of 0.9786 with a collision free decay rate considerably less than that obtained from helium. The estimated rotational level for $v'=22$ was 21, 4 levels lower than that obtained for helium.

Electronic quenching of argon buffer gas at vibrational level 22 is extracted from a Stern-Volmer plot at 2139 ± 112 mTorr sec⁻¹. This quenching rate is slightly less than nitrogen yet more than twice the rate for neon and three times the rate for helium. The increase of quenching rate with atomic mass produces an obvious conclusion of the dependency of k_q on the mass of the colliding specie. Furthermore, because nitrogen dimer is less massive than argon yet maintains a higher quenching rate, the molecular structure is solely responsible for the increased rate. The increase may be the result of V-V transfer or an increase in V-T coupling of the bismuth dimer and buffer specie. Stern-Volmer plots of both levels are shown in figures 4.18 and 4.19.

4.2.5.2 Multiple Exponential Fits to Observed Fluorescence. Multiple exponential fits to $v'=23$ data produced a much better linear correlation of the Stern-Volmer plot, with $r^2=0.843$. The multiple exponential fit to $v'=23$ generates a quenching rate of 4217 ± 688 mTorr sec⁻¹, in between the results for helium and nitrogen (figure 4.20). The collision free lifetimes are reported in table 4.7, and the quenching rates reported in table 4.8.

Table 4.7. Collision Free Decay Rate and Approximate Rotational Levels, Ar Buffer Gas.

v'	Collision Free Decay Rate (Γ_0) (10^6 s ⁻¹)	Radiative Rate ($1/\tau_r$) (10^6 s ⁻¹)	Predisassociative Rate (k_{pd}) (10^6 s ⁻¹)	Predisassociative Rate Coefficient (k_{pdJ}) (sec ⁻¹)	Approximate Rotational Level (J)
22	2.47 ± 0.44	~1.56	0.91	2000	21
23	22.8 ± 1.9	~1.56	28.1	14000	39

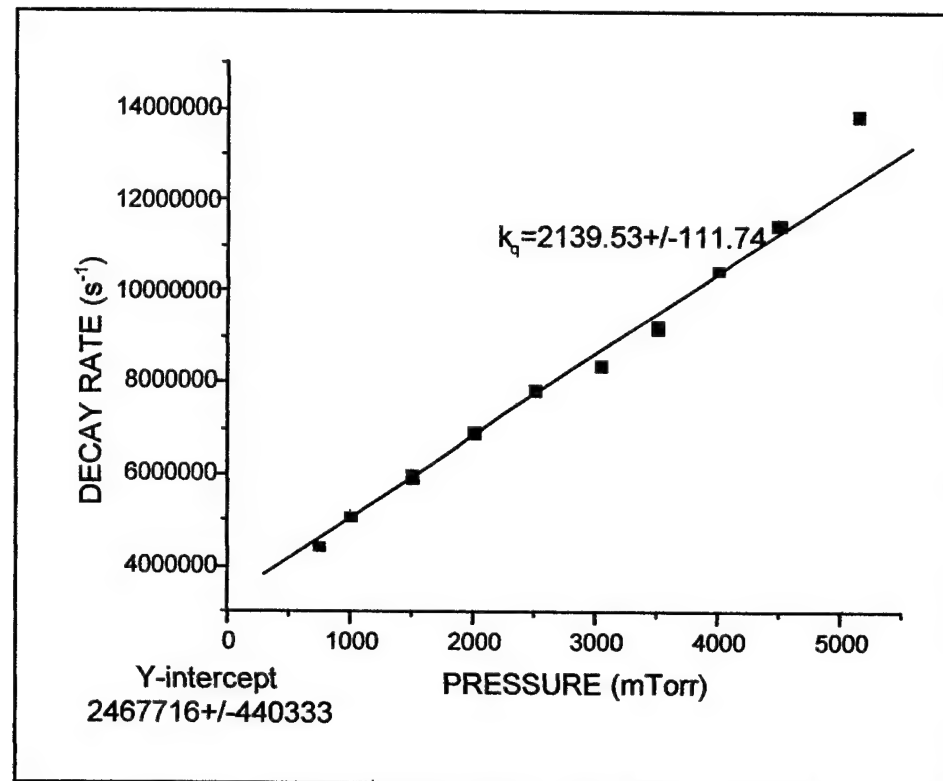


Figure 4.18. Stern-Volmer Plot, Ar buffer gas, $v'=22$.

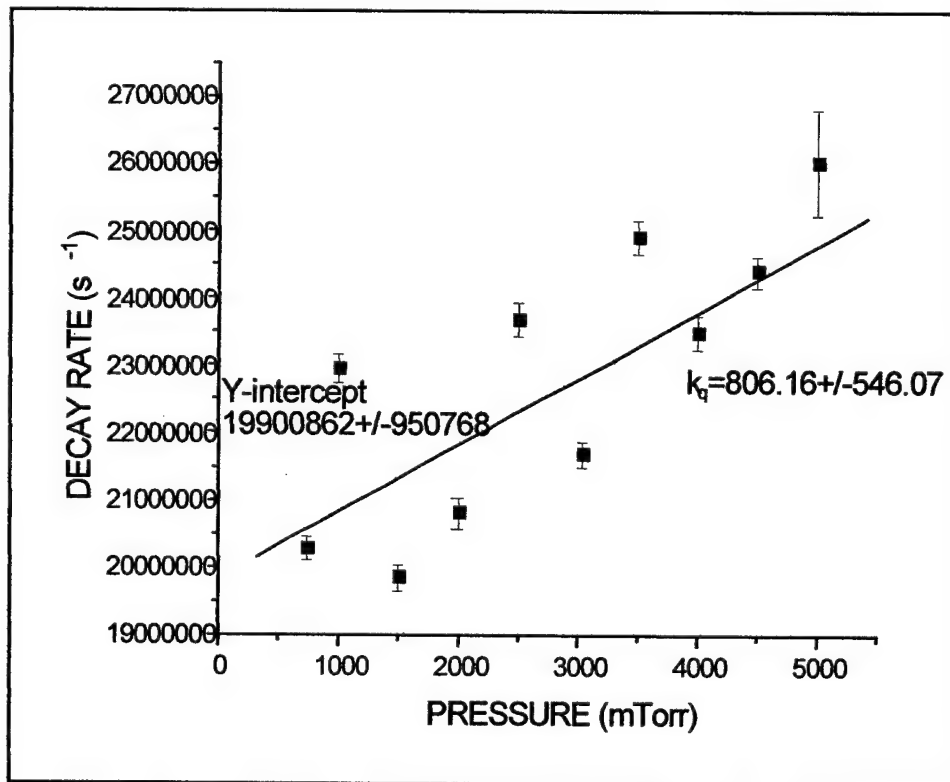


Figure 4.19. Stern-Volmer Plot, Ar buffer gas, $v'=23$.

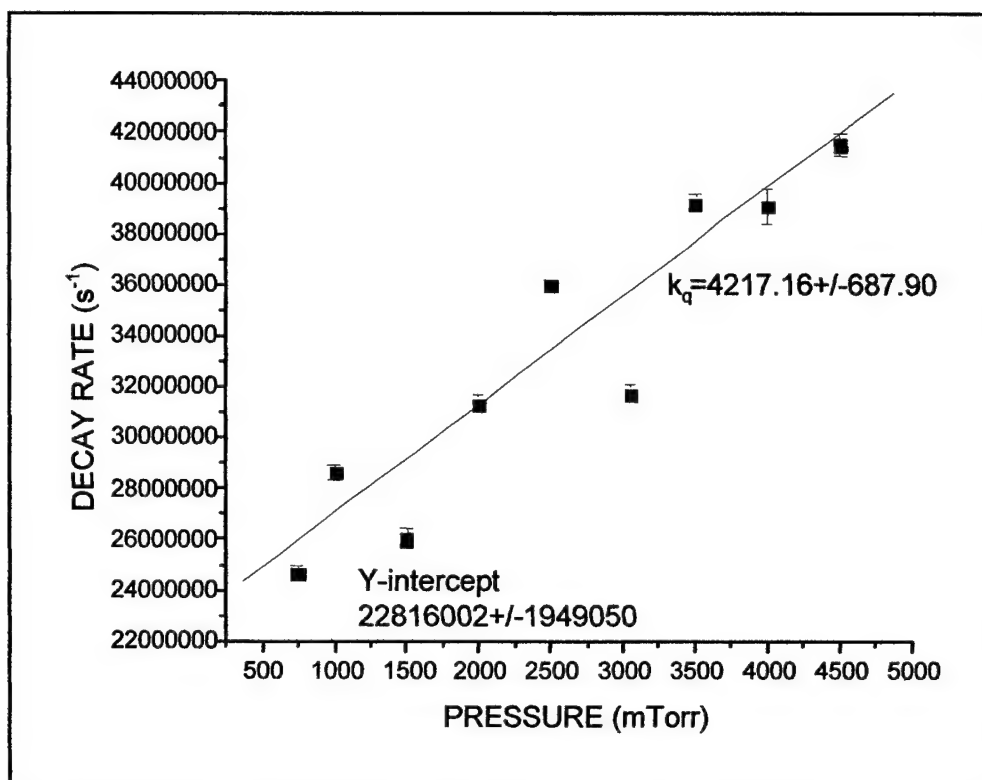


Figure 4.20. Stern-Volmer Plot, Ar buffer gas, $v'=23$, Double Exponential Fit.

Table 4.8. Electronic Quenching Rates by Argon Buffer Gas.

v'	Quenching Rate k_q (mTorr sec $^{-1}$)	Standard Error (mTorr sec $^{-1}$)	Quenching Rate $k_q \times 10^{13}$ k_q (cm 3 molec $^{-1}$ sec $^{-1}$)	Standard Error $\times 10^{13}$ (cm 3 molec $^{-1}$ sec $^{-1}$)
22	2140	± 112	664.5	± 34.8
23	4217	± 688	1309	± 214

4.2.6 Quenching by Krypton of Vibrational Levels $v'=22, 23$. Krypton is more than twice the atomic weight of argon yet this experiment has observed very similar quenching rates between the two species. Conclusions that may be drawn about the quenching rates that are based upon the increasing atomic mass must take this data into consideration.

4.2.6.1 Single Exponential Fits to Observed Fluorescence. The single exponential fits to the $v'=22$ data set were applied to a Stern-Volmer plot (figure 4.21) with a linear fit of $r^2=0.9868$. The linear plot was based upon data points that were extracted from

exponential fits with r^2 ranging from 0.993 to 0.997+, demonstrating less correlation to the exponential fits than with any other data set obtained. The collision free decay rate obtained from the Stern-Volmer plot of $v'=22$ was 3.27×10^6 sec, very similar to nitrogen buffer gas, and corresponding to a rotational level of 29, four levels higher than obtained from helium. The quenching rate was comparable to argon with a rate of 2057 mTorr sec⁻¹. A quenching rate for such a high atomic mass would be expected to be higher than argon (with less than half the atomic weight of krypton). The single exponential fits obtained for $v'=23$ yielded poor Stern-Volmer plots with the resultant r^2 of linear fits 0.195 (figures 4.22).

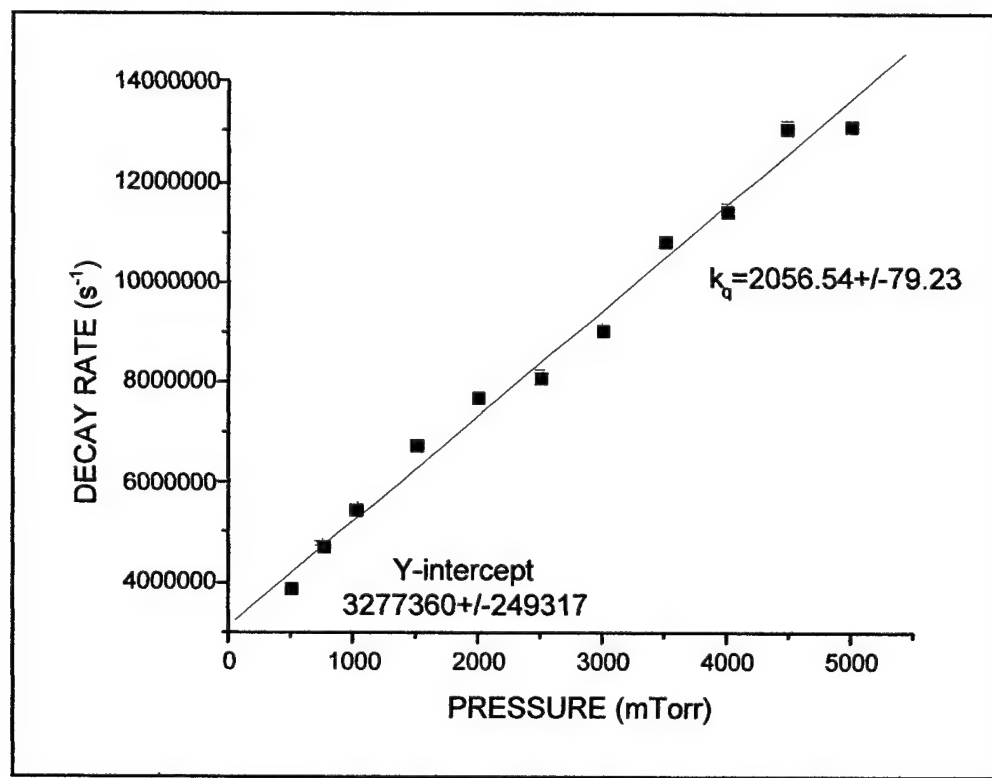


Figure 4.21. Stern-Volmer Plot, Kr buffer gas, $v'=22$.

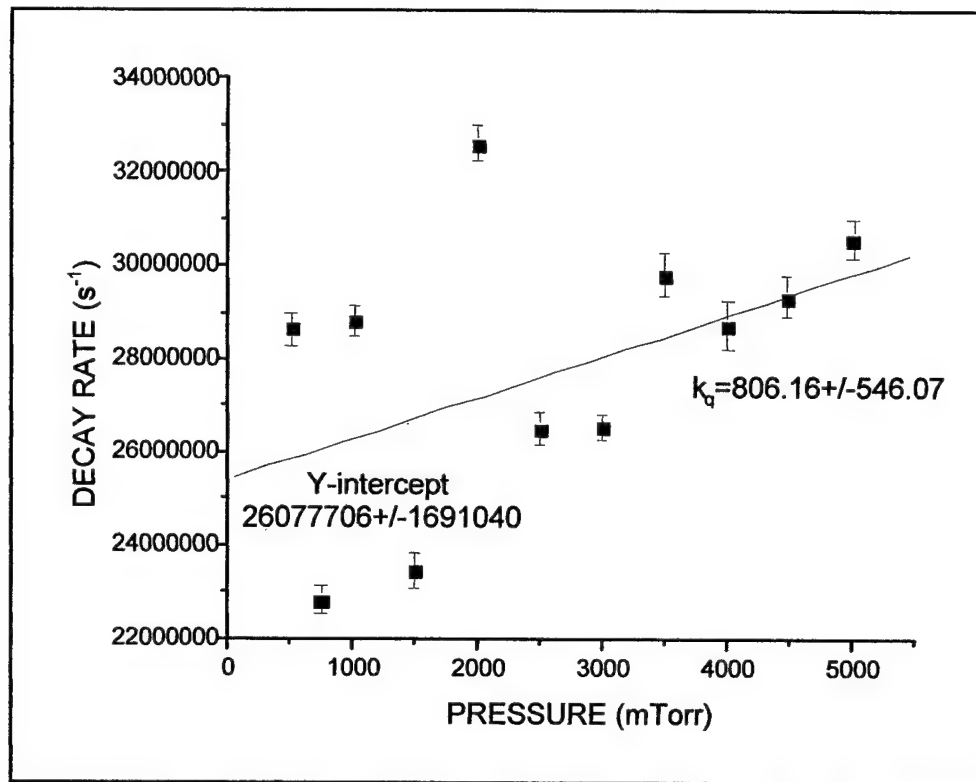


Figure 4.22. Stern-Volmer Plot, Kr buffer gas, $v'=23$.

4.2.6.2 Multiple Exponential Fits to Observed Fluorescence. Vibrational level 23

showed nominal improvement in the Stern-Volmer plot (with a r^2 of 0.248) but still with significantly poor results.

Table 4.9. Collision Free Decay Rate and Approximate Rotational Levels, Kr Buffer Gas.

v'	Collision Free Decay Rate (Γ_0) (10^6 s^{-1})	Radiative Rate ($1/\tau_r$) (10^6 s^{-1})	Predisassociative Rate (k_{pd}) (10^6 s^{-1})	Predisassociative Rate Coefficient (k_{pdJ}) (sec^{-1})	Approximate Rotational Level (J)
22	3.28 ± 0.25	~ 1.56	1.72	2000	29
23	29.7 ± 2.5	~ 1.56	28.1	14000	45

Table 4.10. Electronic Quenching Rates by Krypton Buffer Gas.

v'	Quenching Rate k_q (mTorr sec ⁻¹)	Standard Error (mTorr sec ⁻¹)	Quenching Rate $k_q \times 10^{13}$ k_q (cm ³ molec ⁻¹ sec ⁻¹)	Standard Error $\times 10^{13}$ (cm ³ molec ⁻¹ sec ⁻¹)
22	2057	± 79.2	638.7	± 24.6
23	1669	± 968	518.2	± 301

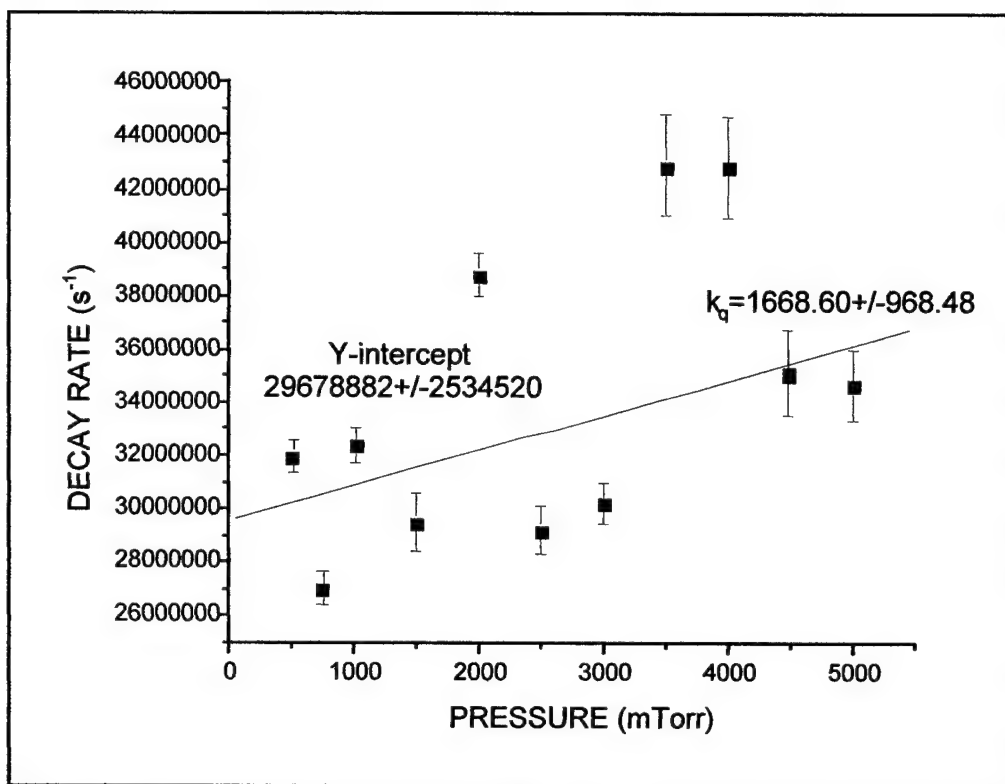


Figure 4.23. Stern-Volmer Plot, Kr buffer gas, $v'=23$, Double Exponential Fit.

4.2.7 Quenching by Xenon of Vibrational Levels $v'=22, 23$. The final buffer gas under study of this experiment was xenon. With an atomic mass of 131.3 amu xenon is nearly one-third the mass of bismuth dimer with a molecular weight of 418. The results for the single exponential plots were excellent for $v'=22$ and $v'=23$. The multiple exponential fit slightly improves the result for $v'=23$. The electronic quenching rates begin higher than any other buffer specie under observation and increase with $v'=23$.

4.2.7.1 Single Exponential Fits to Observed Fluorescence. The single exponential fits for $v'=22$ demonstrated excellent linear correlation under a Stern-Volmer plot, with a coefficient of determination of 0.964. The observed collision free decay rate was the highest recorded under this study for that vibrational level, with a value of $3.69 \times 10^6 \text{ sec}^{-1}$ corresponding to rotational number 33, eight levels higher than reported for helium. This may indicate systematic error in the measurement. The quenching rate for $v'=22$ was

$2739 \text{ mTorr sec}^{-1}$, the highest for any specie observed at that vibrational level. The single exponential fits for vibrational level 23 were comparatively good, with a collision free lifetime of 2.06×10^7 (estimated rotational level of 37, compared to helium with 40) and a quenching rate of $3431 \text{ mTorr sec}^{-1}$.

Table 4.11. Collision Free Lifetimes and Approximate Rotational Levels, Xenon.

v'	Collision Free Lifetime (Γ_0) (10^6 s^{-1})	Radiative Rate ($1/\tau_r$) (10^6 s^{-1})	Predisociative Rate (k_{pd}) (10^6 s^{-1})	Predisociative Rate Coefficient (k_{pdj}) (sec $^{-1}$)	Approximate Rotational Level (J)
22	3.69 ± 0.62	~ 1.56	2.13	2000	33
23	21.4 ± 1.1	~ 1.56	19.9	14000	38

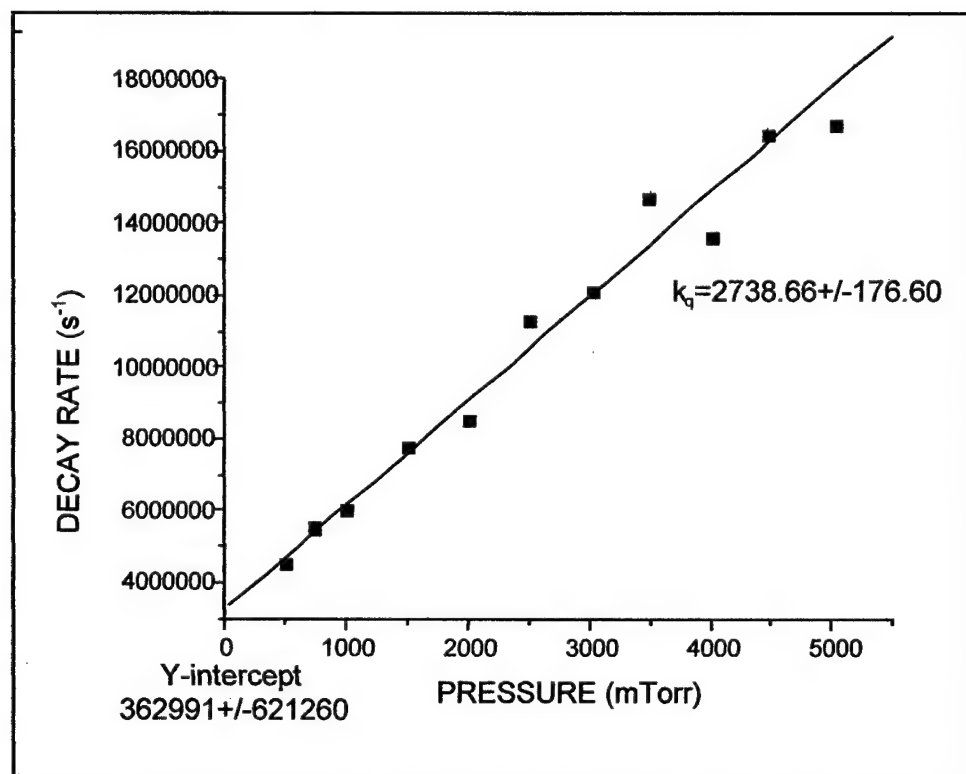


Figure 4.24. Stern-Volmer Plot, Xe buffer gas, $v'=22$.

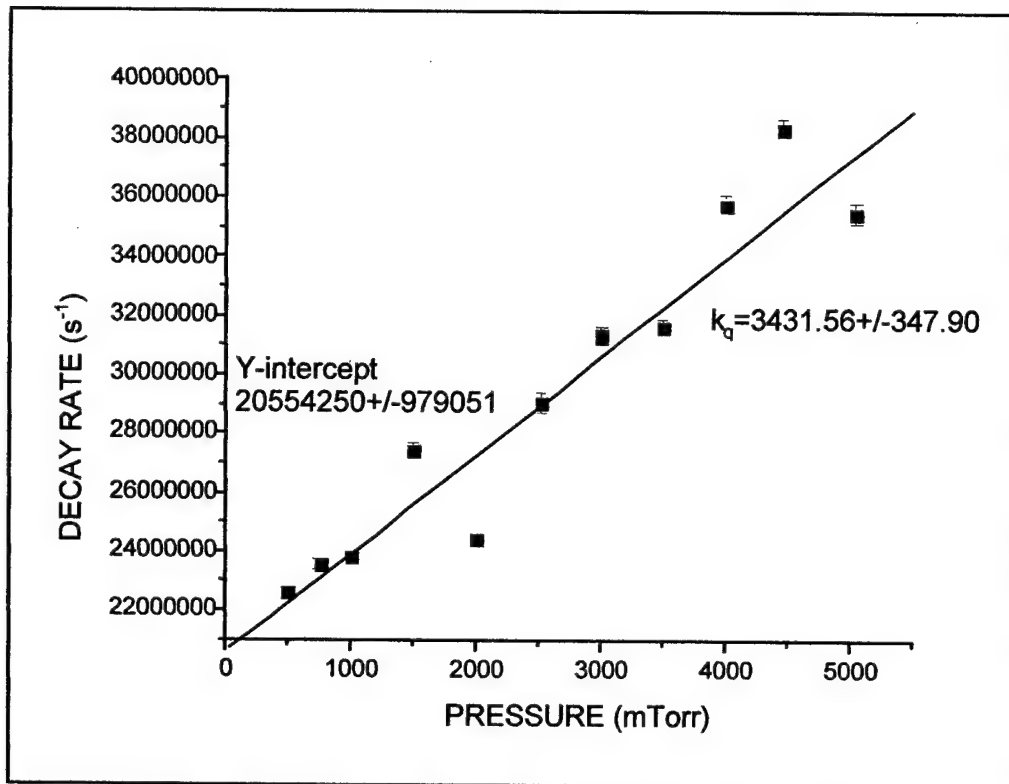


Figure 4.25. Stern-Volmer Plot, Xe buffer gas, $v'=23$.

4.2.7.2 Multiple Exponential Fits to Observed Fluorescence. The collision free lifetime for $v'=23$ corresponds to an estimated rotational level of 38, two levels lower than the same vibrational manifold under helium buffer gas. A quenching rate of 5033 mTorr sec⁻¹ is observed which is almost double the rate for the lower vibrational level. In order to make sense of these quenching rates and the relationships between buffer gasses and the extracted rates, comparisons must be drawn between data sets of the same vibrational levels, and furthermore, between data sets of the same buffer gas. These comparisons will be addressed in the next section.

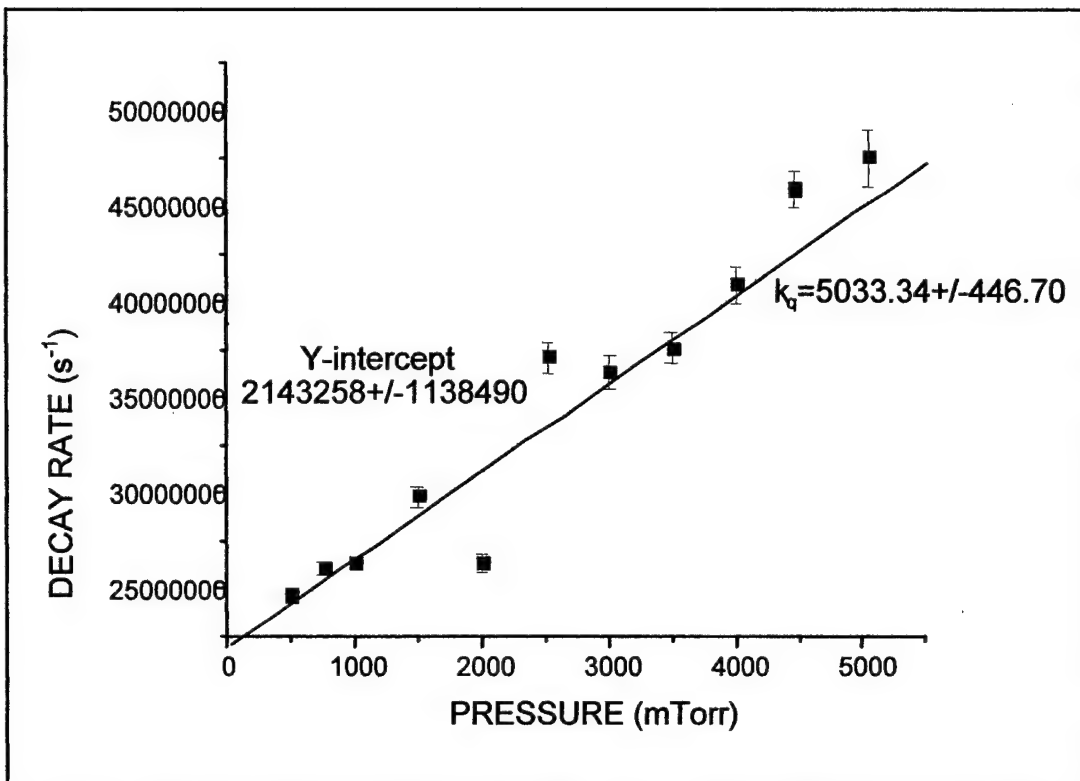


Figure 4.26. Stern-Volmer Plot, Xe buffer gas, $v'=23$. Double Exponential Fit.

Table 4.12. Electronic Quenching Rates by Xenon Buffer Gas.

v'	Quenching Rate k_q (mTorr sec $^{-1}$)	Standard Error (mTorr sec $^{-1}$)	Quenching Rate $k_q \times 10^{13}$ k_q (cm 3 molec $^{-1}$ sec $^{-1}$)	Standard Error $\times 10^{13}$ (cm 3 molec $^{-1}$ sec $^{-1}$)
22	2739	± 177	850.5	± 55.0
23	5033	± 447	1563	± 139

4.3 Qualitative Comparison of Stern-Volmer Plots The following qualitative comparisons seek a different approach to the analysis of the data by examining two Stern-Volmer plots at the same time and attempting to reach conclusions regarding the progression of the electronic quenching rates. Comparisons will be made by examining the two vibrational levels reported ($v'=22$ and 23) for all buffer gases under study.

4.3.1 Vibrational Level 22. Figure 4.27 displays the cumulative Stern-Volmer plots of all buffer gasses for vibrational level 22. Each data set has an obvious linear pressure dependency with a trend towards a common y-intercept (collision-free lifetime). The

convergence towards the same collision free lifetime is an important feature to verify the results of the extracted quenching rates. Any significant deviation of y-intercept of a linear slope would be suspect, and probably result in the discarding of the data set from further analysis. Each data set was fit to a linear function with r^2 values greater than 0.965.

The progression of buffer gasses in the figure demonstrate that atomic (or molecular) masses are the primary factor in determining the quenching rate as the slope of the data sets increase from He, through Ne, Kr, and up to Xe. Distinctly out of place, with regard to mass of the colliding specie, are N₂ and Ar. With the molecular mass of nitrogen dimer about one-third the atomic mass of krypton, the appearance of the nitrogen data set to closely match the data set of krypton must be the result of enhanced quenching of bismuth dimers by the nitrogen buffer gas. The mechanism has not been explored in this thesis, but may be related to V-V transfer. The atomic mass of argon is less than half of the atomic mass of krypton, yet generated significantly greater quenching of bismuth dimers and is comparable to the effect of xenon, more than four times as massive. Because atomic structures cannot support molecular interactions, such as V-V transfer, the most probable mechanism for the increase in quenching is electron-electron interaction. The mechanism for this increased quenching is also not explored in this thesis.

To ascertain the electronic quenching probability, equation [2.3.30] must be applied along with table 2.1 (Gas Kinetic Collision Parameters).

$$P = \frac{\sigma_{event}}{\sigma_g} \quad (2.3.30)$$

$$P = \frac{\sigma_{\text{event}}}{\sigma_g} = \frac{\sigma_{\text{event}} v_{12}}{\sigma_g v_{12}} = \frac{k_{\text{event}}}{k_g} \quad (4.3.1)$$

$$P_q = \frac{k_q}{k_g} \quad (4.3.2)$$

The probability of quenching is determined by dividing the quenching rate by the gas kinetic rate. These values are generated in table 4.13, and quenching probabilities are plotted with respect to the reduced mass, μ , in figure 4.31.

Table 4.13. Electronic Quenching Probabilities, $v'=22$.

Buffer Gas	Reduced Mass μ (amu)	Quenching Rate $k_q \times 10^{13}$ ($\text{cm}^3 \text{ molec}^{-1} \text{ sec}^{-1}$)	Gas Kinetic Rate $k_g \times 10^{10}$ ($\text{cm}^3 \text{ molec}^{-1} \text{ sec}^{-1}$)	Probability P_q
He	3.96	227.3 ± 16.1	7.03	0.0323 ± 0.0023
Ne	19.3	280.4 ± 19.2	3.41	0.0822 ± 0.0056
Ar	36.5	664.5 ± 34.8	2.84	0.2340 ± 0.0123
Kr	69.8	638.7 ± 24.6	2.13	0.2998 ± 0.0115
Xe	99.9	850.5 ± 55.0	1.95	0.4362 ± 0.0282
N ₂	26.2	803.0 ± 45.3	3.12	0.2574 ± 0.0145

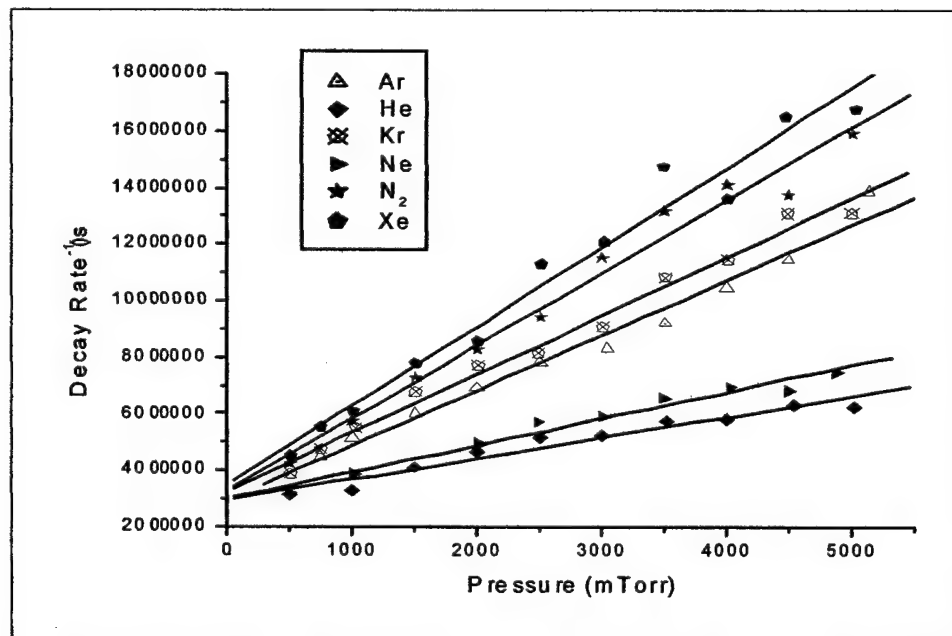


Figure 4.30. Stern-Volmer Summary of all Buffer Gasses, $v'=22$.

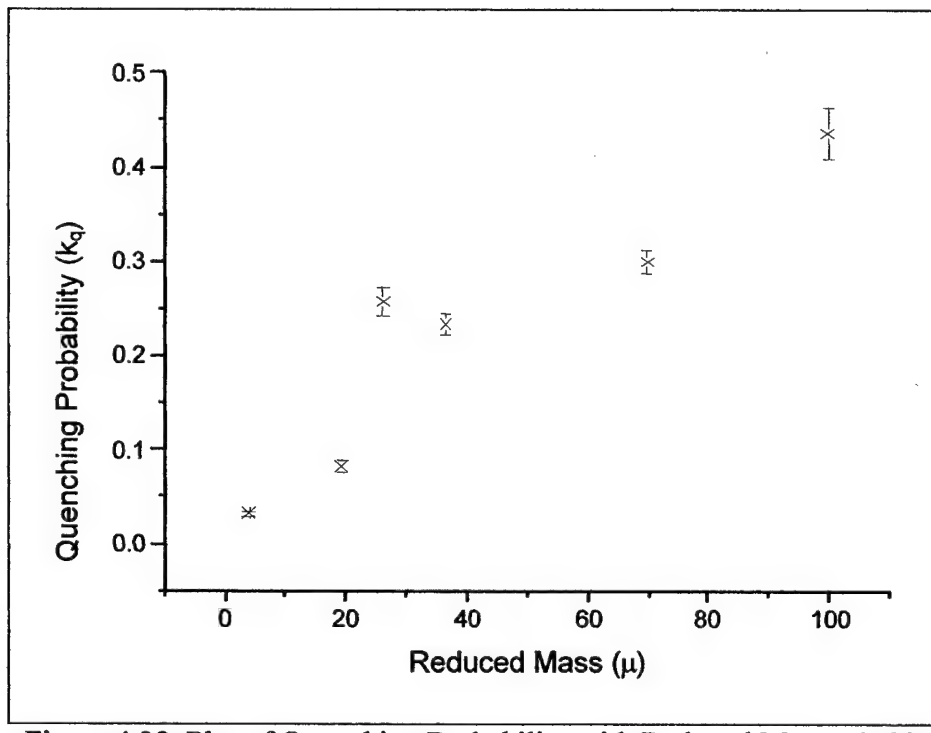


Figure 4.28. Plot of Quenching Probability with Reduced Mass, $v'=22$.

4.3.2 Vibrational Level 23. A similar analysis for vibrational level 23 does not reproduce as obvious of results. All data sets appear to have generally linear properties about a large deviation from an average of the sets. Xenon is clearly evident at the top of the data set and demonstrates its significant departure from linearity. Of all the buffer gasses studied, only krypton was concluded to have insufficient accuracy to be reportable in this thesis. The pressure dependent relationships show a similar collision free lifetime without significant deviations. The quenching rates are very similar and less defined as in the previous vibrational level. A statement similar to the one made in the last subsection regarding the mass dependencies and the anomalous behavior of nitrogen and argon cannot be made in this example.

As in the previous section, electronic quenching probabilities have been calculated and are reported in table 4.14 and plotted with respect to reduced mass in figure 4.31.

Table 4.14. Electronic Quenching Probabilities, $v^*=23$.

Buffer Gas	Reduced Mass μ (amu)	Quenching Rate $k_q \times 10^{13}$ ($\text{cm}^3 \text{ molec}^{-1} \text{ sec}^{-1}$)	Gas Kinetic Rate $k_g \times 10^{10}$ ($\text{cm}^3 \text{ molec}^{-1} \text{ sec}^{-1}$)	Probability P_q
He	3.96	1045 ± 139	7.03	0.1486 ± 0.0198
Ne	19.3	280.4 ± 19.2	3.41	0.2174 ± 0.0484
Ar	36.5	664.5 ± 34.8	2.84	0.4609 ± 0.0754
Xe	99.9	850.5 ± 55.0	1.95	0.8015 ± 0.0713
N ₂	26.2	803.0 ± 45.3	3.12	0.5032 ± 0.1561

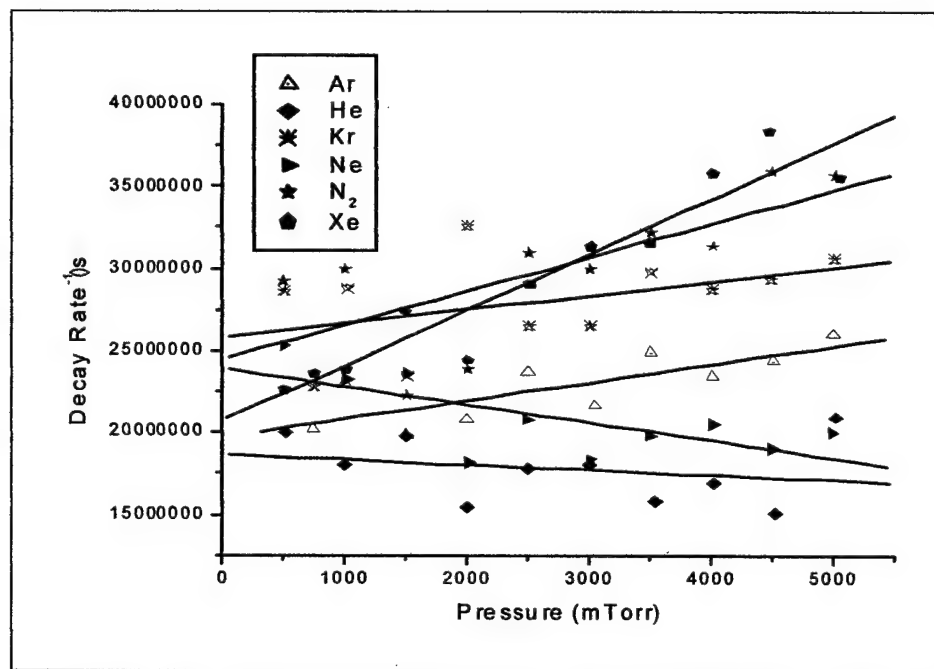


Figure 4.32. Stern-Volmer Summary of all Buffer Gasses, $v^*=23$.
Single exponential fits only.

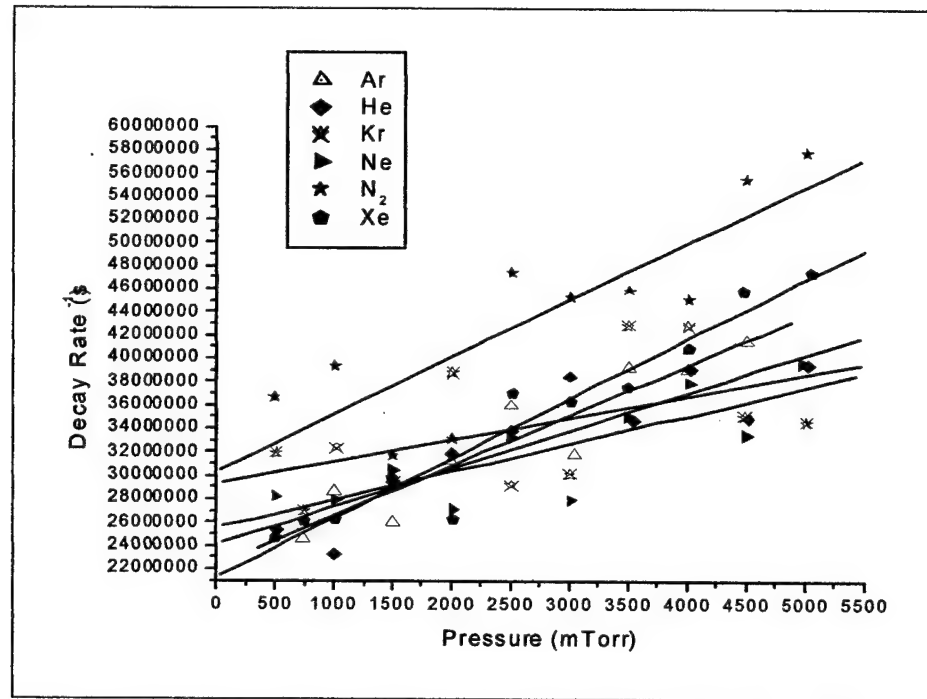


Figure 4.30. Stern-Volmer Summary of all Buffer Gasses, $v'=23$.
Double exponential fits only.

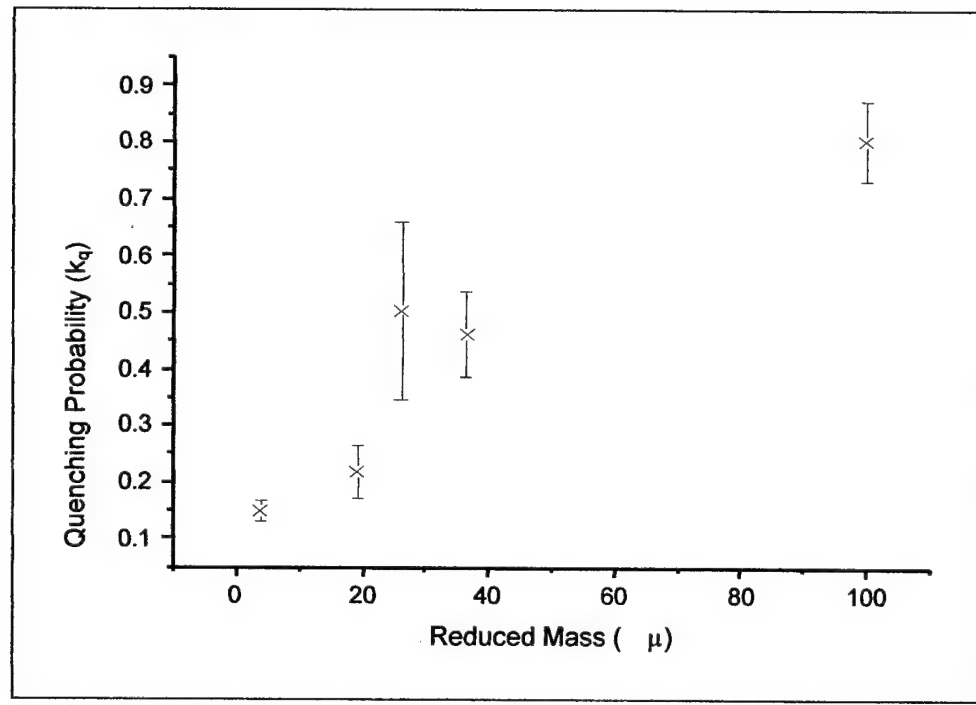


Figure 4.31. Plot of Quenching Probability with Reduced Mass, $v'=23$.

4.4 Conclusions Temporally resolved laser induced fluorescence was observed for vibrational levels $v'=18$ through $v'=25$ with helium buffer gas, and for vibrational levels $v'=22$ through $v'=25$ with neon, argon, krypton, xenon, and diatomic nitrogen buffer gasses at pressures ranging from 500mT to 5 Torr.

4.4.1 Report of Electronic Quenching Rates. After careful analysis and close scrutiny of the resulting data, electronic quenching rates are to be reported for vibrational levels $v'=18$ through $v'=23$. The following table 4.13 represents only the analysis of vibrational levels under quenching by buffer gasses that were concluded to be accurate representations of the electronic quenching of bismuth dimers.

Table 4.15. A Summary of Electronic Quenching Rates.

v'	Buffer Gas	Quenching Rate $k_q \times 10^{13}$ @300K ($\text{cm}^3 \text{ molec}^{-1} \text{ sec}^{-1}$)	Standard Error $\times 10^{13}$ @300K ($\text{cm}^3 \text{ molec}^{-1} \text{ sec}^{-1}$)
22	Helium	227.3	± 16.1
22	Neon	280.4	± 19.2
22	Nitrogen	803.0	± 45.3
22	Argon	664.5	± 34.8
22	Krypton	638.7	± 24.6
22	Xenon	850.5	± 55.0
23	Helium	1045	± 139
23	Neon	741.2	± 165
23	Nitrogen	1570	± 487
23	Argon	1309	± 214
23	Xenon	1563	± 139

The quenching rates for $v'=22$ ranged from 227.3 to $850.5 \times 10^{13} \text{ cm}^3 \text{ molec}^{-1} \text{ sec}^{-1}$, and $v'=23$ rates ranged from 741.2 to $1570 \text{ cm}^{-1} \text{ molec}^{-1} \text{ sec}^{-1}$.

V. CONCLUSIONS

5.1 Summary of Electronic Quenching Rates Previous research in this area was performed by spectrally resolved, temporally resolved fluorescence of vibrational levels $v'=8$ through $v'=39$ using out-gassed vapors at pressures from 15-150mTorr. For this experiment, temporally resolved laser induced fluorescence was observed for vibrational levels $v'=18$ through $v'=25$ with helium buffer gas, and for vibrational levels $v'=22$ through $v'=25$ with neon, argon, krypton, xenon, and diatomic nitrogen buffer gasses at pressures ranging from 500mT to 5 Torr. The quenching rates for $v'=22$ ranged from 227.3 to $850.5 \times 10^{-13} \text{ cm}^3 \text{ molec}^{-1} \text{ sec}^{-1}$, and $v'=23$ rates ranged from 741.2 to 1570 $\times 10^{-13} \text{ cm}^3 \text{ molec}^{-1} \text{ sec}^{-1}$. The quenching rates for $v'=24$ and $v'=25$ were not resolvable with this apparatus.

5.2 Further Studies This temporally resolved laser induced fluorescence experiment may be enhanced significantly by improving the temporal resolution of the data collection. The oscilloscope used had a clock speed of 300MHz, providing a temporal resolution of only 3.3ns. There would only be a handful of data points per e-fold of decay for the higher predissociated levels under this resolution. With fewer available points to provide for the necessary fitting, the extracted quenching rates and V-T data are prone to error. An oscilloscope with a clock speed of 2GHz on the other hand, will provide a resolution 6.5 times greater and enable more accurate representation of the fluorescence decay in the data.

Further study of the collisional dynamics of predissociated states should involve some aspect of spectral resolution. By excitement of a parent predissociated state and subsequent monitoring of the collisionally populated satellite states, proper V-T transfer analysis may be conducted. The lack of spectral resolution in this experiment inhibited any observation of this effect and the determination of the accuracy of various popular molecular theories.

Appendix A: Report of Fluorescence Lifetimes

A.1 Vibrational Level 22, Single Exponential Fits The following data is obtained by single exponential fits and reported in mTorr pressure and sec⁻¹ of decay rate.

Table A.1. He, v'=22.

HELIUM	v'=22	Single Exponential Fit	
Pressure	r2	Decay	Decay Std Err
501	0.99943649	3143584.1	4108.7
1002	0.99793723	3260193.2	9227.8
1502	0.99956771	4102595.2	16543.6
2003	0.99752681	4639825.5	35302.2
2493	0.9982401	5180386.2	32426.4
3000	0.99850483	5240142.5	30242.4
3515	0.99745996	5764993	41691.7
4004	0.99756006	5790924.8	51526.7
4545	0.99666361	6297397.4	50432.7
5015	0.99829504	6224923.1	14931.9

Table A.2. Ne, v'=22.

NEON	v'=22	Single Exponential Fit	
Pressure	r2	Decay	Decay Std Err
500	0.99942481	3173644.5	16610.5
1016	0.9981988	3879174.2	32290.2
1500	0.99865381	44344157.2	26222.1
2007	0.99827649	4950352	37150.2
2485	0.99864188	5709011.8	37213.9
3015	0.99889033	5892510.2	34420
3500	0.99411071	6559038.5	85350
4024	0.99857919	6941982.8	41379.6
4492	0.9986973	6809818.6	14563.8
4876	0.99837419	7448739.1	18719.7

Table A.3. Ar, v'=22.

ARGON	v'=22	Single Exponential Fit	
Pressure	r2	Decay	Decay Std Err
743	0.99917656	4469398.3	23928
1000	0.99985886	5116636.4	10926.4
1506	0.99905825	5992586.6	31848.2
2002	0.99968599	6910441.4	19539.4
2497	0.99966024	7797661.6	22105.9
3047	0.99952708	8331713.8	26536.4
3510	0.99920147	9214402.4	31217
4003	0.99916918	10472304	35543.7
4495	0.99946973	11442344	30721.1
5138	0.99499453	13850950	135645.2

Table A.4. Kr, v'=22.

KRYPTON	v'=22	Single Exponential Fit	
Pressure	r2	Decay	Decay Std Err
501	0.99665736	3887429.9	44306.3
750	0.99619464	4754510.4	52074.2
1028	0.99444071	5499178.3	69335.1
1499	0.99534574	6771100.6	72678.5
2006	0.99390006	7711211.2	91581.7
2496	0.99310905	8142208.8	101856.2
3006	0.99715016	9082295.4	73899.4
3510	0.99717113	10844929	83721.2
4005	0.99494158	11459005	116843.7
4493	0.99490169	13097409	131002.1
5002	0.99736029	13124977	96010.2

Table A.5. Xe, v'=22.

XENON	v'=22	Single Exponential Fit	
Pressure	r2	Decay	Decay Std Err
500	0.99893044	4535183.9	26458.5
750	0.99875631	5543833.7	32216.1
1000	0.99885217	6075646.6	32461
1500	0.99868977	7799436.2	41597.2
2002	0.99836098	8544124.3	50433.8
2515	0.99927221	11327620	42865.4
3020	0.99836713	12129798	68277.8
3498	0.99869242	14744069	74223.8
4008	0.99886073	13640070	63877.9
4475	0.99819936	16516161	97558
5034	0.99779091	16764296	109370.4

Table A.6. N₂, v'=22.

NITROGEN	v'=22	Single Exponential Fit	
Pressure	r2	Decay	Decay Std Err
498	0.99514107	4209556	52510.2
998	0.99554425	5734059.5	59819.7
1500	0.9970273	7290128.5	57874.8
2004	0.99843908	8259105.4	46954.9
2503	0.998572	9450043.8	50234.6
3001	0.99854032	11544657	61012
3502	0.99767402	13203801	87716.7
4002	0.99707515	14100814	103630
4500	0.99541203	13758190	126202.4
5010	0.99660733	15936050	126079.5

A.2 Vibrational Level 23, Single Exponential Fits

Table A.7. He, v'=23.

HELIUM	v'=23	Single Exponential Fit	
Pressure	r2	Decay	Decay Std Err
512	0.99307876	20023441	20685.2
1002	0.97832951	18037353	373692.4
1500	0.98533547	19820771	336609.5
2005	0.97461129	15420661	343455.2
2502	0.98395544	17833395	316698.9
3003	0.97875004	18017498	368603.3
3545	0.97921503	15785752	322473.5
4025	0.94695922	16923998	5558645.8
4518	0.98214147	15049241	287205.2
5020	0.9843213	20951000	531551.7

Table A.8. Ne, v'=23.

NEON	v'=23	Single Exponential Fit	
Pressure	r2	Decay	Decay Std Err
499	0.99636438	25315058	209424
1016	0.99599996	23229934	202330.7
1500	0.99038605	23628835	322292.5
2006	0.99007284	18166707	251668.2
2494	0.98815524	20814476	311633.6
3005	0.99068211	18360279	247456
3498	0.98890541	19837994	291694.8
4018	0.98881941	20489231	302478.6
4500	0.99097606	19007030	253387.7
4985	0.98825542	20044896	304534.8

Table A.9. Ar, v'=23.

ARGON	v'=23	Single Exponential Fit	
Pressure	r2	Decay	Decay Std Err
742	0.99604602	20275866	173472.4
1002	0.99562652	22971451	210076.4
1503	0.99450186	19836384	200577.6
1994	0.9931388	20806335	232209.8
2499	0.99445345	23689584	242446.9
3047	0.995964	21681186	189120.6
3510	0.99452262	24915066	253820.5
4007	0.99375885	23499218	255807.5
4512	0.99540147	24411988	227289.7
5002	0.95524725	26013101	784439.2

Table A.10. Kr, v'=23.

KRYPTON	v'=23	Single Exponential Fit	
Pressure	r2	Decay	Decay Stnd Err
509	0.99188869	28647276	353048.7
748	0.9916093	22823886	284543.4
1019	0.99261789	28805773	336857.2
1501	0.9844252	23457047	395438.6
2003	0.99280746	32587110	379359.7
2502	0.99024617	26514545	356518.6
3005	0.99489605	26537156	256341.3
3503	0.98673561	29798106	465160.2
4008	0.9841694	28742349	497475.8
4485	0.9888339	29340888	429112.5
5012	0.99171927	30587684	393246.1

Table A.11. Xe, v'=23.

XENON	v'=23	Single Exponential Fit	
Pressure	r2	Decay	Decay Stnd Err
499	0.99771817	22609066	147652.1
752	0.9968518	23586310	182487.8
1005	0.99869254	23846699	117681.2
1494	0.9963157	27425939	231866.9
2005	0.99748682	24446630	169573.8
2518	0.99004352	29040298	319774.2
3012	0.99533892	31347943	299848.4
3500	0.99722733	31611472	231383.9
4007	0.99595076	35787450	320916.4
4471	0.99689428	38354155	299862.9

Table A.12. N₂, v'=23.

NITROGEN	v'=23	Single Exponential Fit	
Pressure	r2	Decay	Decay Stnd Err
498	0.98931138	29216939	404639.2
1001	0.9869017	29934428	460445.6
1500	0.9927803	22318235	254635.4
2002	0.99470241	23920528	235339.9
2504	0.99148099	30998403	389728.8
3004	0.99481579	29974924	295847.1
3506	0.9961376	32200075	275035
4012	0.99615409	31391249	265641.6
4500	0.99336846	35936362	405220.2
5016	0.99542665	35677097	333198.3

A.5 Vibrational Level 23, Double Exponential Fits The following decay rates and standard errors are reported from double exponential fits, as provided in equation [3.4.2], $I = I_0\{E \text{ Exp}(-A*t) + F \text{ Exp}(-B*t)\}$. The coefficients E and F are reported with the decay rate B. Decay rate A, held constant during the fit, was obtained by a single exponential fit to $v'=22$ at the same pressure.

Table A.24. He, $v'=23$.

HELIUM	$v'=23$	Double Exponential Fit				
Pressure	r2	E	F	Decay (B)	Decay Stnd Err	
502	0.9984036	0.02646921	0.8905811	25432488	65211	
1005	0.98266564	0.003048032	0.29598529	23226706	789077	
1496	0.99450441	0.004678453	0.76312151	29500552	591777	
2002	0.98733406	0.006069498	0.88172308	31910805	1251720	
2503	0.99783625	0.011696394	2.0515094	33896355	505892	
3020	0.99547283	0.01408171	4.1073529	38495127	881864	
3505	0.99279156	0.016181536	2.1643065	34763179	1126300	
4024	0.96407188	0.007425371	2.110007	39137816	2675880	
4511	0.99439293	0.014704764	1.5634607	34871880	1113950	
5012	0.99493285	0.19274117	43774945.17	39426808	1326840	

Table A.25. Ne, $v'=23$.

NEON	$v'=23$	Double Exponential Fit				
Pressure	r2	E	F	Decay (B)	Decay Stnd Err	
499	0.99754398	0.005030184	2.834485	28246060	313829	
1016	0.99860488	0.009211735	2.5638249	27944238	252211	
1500	0.99522837	0.010368513	3.0102201	30512060	538041	
2006	0.99614492	0.014197249	1.2734585	27104814	521550	
2494	0.99606276	0.016925951	3.4424064	33360537	647970	
3005	0.99634983	0.021614565	1.6844726	27942000	579553	
3498	0.99838689	0.032012487	5.7178459	35103501	489506	
4018	0.99934179	0.055476851	13.79341	37959643	342301	
4500	0.9994046	0.069043318	8.4462147	33500826	303780	
4985	0.99917836	0.070851951	18.491573	39668837	431036	

Table A.26. Ar, v'=23.

ARGON	v'=23	Double Exponential Fit				
Pressure	r2	E	F	Decay (B)	Decay Stnd Err	
742	0.99792338	0.006221036	0.98148885	24674279	309917	
1002	0.99853343	0.008409008	2.2994356	28665769	294761	
1503	0.99744102	0.010343693	1.1972039	26032653	407290	
1994	0.99873524	0.020334047	3.3975915	31368387	359419	
2499	0.99962766	0.032002297	8.7450707	35985258	235510	
3047	0.99938536	0.037511284	4.4463203	31787023	302774	
3510	0.99954122	0.045431796	14.523101	39225380	311461	
4007	0.99847204	0.038336341	8.3896914	39061634	661895	
4512	0.99944354	0.083441738	19.01671	41533211.5	454450	

Table A.27. Kr, v'=23.

KRYPTON	v'=23	Double Exponential Fit				
Pressure	r2	E	F	Decay (B)	Decay Stnd Err	
509	0.99305772	0.000636515	0.65962534	31969062	601227	
748	0.99311986	0.00094029	0.22185717	26997048	595052	
1019	0.99350227	0.000676531	0.49859655	32404441	667387	
1501	0.98602028	0.001698299	0.29973597	29504379	1107760	
2003	0.99438002	0.001551772	1.4786081	38781603	811516	
2502	0.99056159	0.001099885	0.33201625	29197463	928291	
3005	0.99532699	0.00170989	0.37665475	30208105	736478	
3503	0.98664446	0.004080912	1.8187566	42871289	1888230	
4008	0.98721456	0.004170387	1.6687705	42818468	1886200	
4485	0.98930491	0.003180486	0.51146062	35108334	1631030	
5012	0.99208801	0.002464647	0.52132065	34639352	1299700	

Table A.28. Xe, v'=23.

XENON	v'=23	Double Exponential Fit				
Pressure	r2	E	F	Decay (B)	Decay Stnd Err	
499	0.99821757	0.001204752	0.39636621	24744418	270939	
752	0.99739619	0.001196846	0.37895941	26074579	365872	
1005	0.99910458	0.002014604	0.59732184	26297287	229839	
1494	0.99660534	0.00135234	0.63405473	29792307	529949	
2005	0.99765683	0.001767375	0.40061336	26357725	452482	
2518	0.99304896	0.005444931	1.7708853	37121436	823801	
3012	0.99593161	0.003837309	1.2185208	36312002	874993	
3500	0.99766332	0.008373559	1.5346463	37619343	845770	
4007	0.99640421	0.005264764	3.0616541	40929481	939815	
4471	0.99746276	0.010549681	5.4251348	45890250	994671	
5057	0.99577881	0.021580076	8.3738973	47521317	1486530	

Table A.29. N₂, v'=23.

NITROGEN	v'=23	Double Exponential Fit			
Pressure	r2	E	F	Decay (B)	Decay Stnd Err
498	0.99269994	0.001886171	1.0632086	36641766	719322
1001	0.99238981	0.001718091	1.3200508	39351883	808008
1500	0.99698958	0.00375021	0.44202321	31674892	551783
2002	0.99783709	0.00526596	0.6812453	33169002	516751
2504	0.99760229	0.007305752	5.7068286	47504930	723725
3004	0.99852386	0.010118391	3.3967361	45311103	666040
3506	0.99892546	0.013796608	4.5000724	45951818	595968
4012	0.99864684	0.013450209	3.10691	45155214	705023
4500	0.99760501	0.013100723	13.854902	55569282	1042380
5016	0.99896221	0.025253787	21.029534	57841024	829227

Appendix B: Summary of Errors

B.1 Discussion of Errors The errors present in the experiment were observed and characterized as much as possible. Mitigation of the errors was conducted if plausible. But the effect of errors not mitigated or not well characterized was also evaluated to determine the outcome of the final product of the experiment. The purpose of this experiment is to report the electronic quenching rates as determined by linear Stern-Volmer plots of decay rate versus pressure. Therefore, over the course of buffer gas specie observed at a given vibrational level, the concern of the experiment was purely on the slope of the observed linear fit (although the intercept had certain ancillary benefits as discussed in Chapter 4). There are three issues that will be discussed accordingly, errors propagated by the sectioning of data, the variance of pressure within the fluorescence cell, and the observation of multiple exponential decay curves at the same time.

B.2 Sectioning Error Various methods of sectioning data were studied to determine the method that presented the least error. For a given fluorescence data point, sectioning data at several different locations along the decay curve while still maintaining high coefficients of determination (>0.995), analysis of the fluorescence decay rate may differ by as much as 20%. Changes in the sectioning of data from one data point to the next in a buffer gas sample will greatly affect the observation of electronic quenching rate as derived from a linear fit of such decay rates. Therefore, a consistent method must be applied to each data point to mitigate these errors.

For each vibrational level studied, for all buffer gasses, specific temporal locations were selected along the curve (i.e. constant time after trigger pulse) that served as the beginning and end of the data to be sectioned. This sectioned data was the only used to fit to exponentials (or double exponentials) and characterize the decay. This consistency eliminated most of the systematic error present by sectioning and enabled comparison of quenching rates between different buffer gasses that otherwise would have vastly different results.

B.3 Pressure Variance The pressure maintained within the fluorescence cell during data collection was an important aspect of determining quenching rates. Large deviations in pressure from the recorded pressure of fluorescence decay could generate significant errors in the Stern-Volmer analysis. For this experiment, measurements were not considered valid if the pressure varied any more than 0.5% of the desired pressure. In this way the effects of systematic errors introduced by unstable pressures could be minimized. Because the Stern-Volmer technique utilizes a linear fit of data recorded by

pressure, the variance of pressure points by $\pm 0.5\%$ will not significantly affect the recorded quenching rates.

The pressure of the fluorescence cell was not observed at the point of fluorescence in the actual center of the cell, but rather in the lateral arm that also serves as an input source of buffer gas. Because buffer gas must constantly flow through the arm, into the center of the fluorescence cell, and escape through the vacuum system on the top of the cross, there is necessarily a pressure differential between the MKS Baritron manometer and the actual fluorescence location. The pressure differential is directly proportional to the flow of buffer gas. For this reason, the buffer gas flow was held as consistent as possible through measurements by the manipulation of buffer gas inlet valve and vacuum valve. Since there is no mechanism to observe the flow of buffer gas, one must rely upon the experimenter's sense of sound (observing relative flow of buffer gas through the cell by the sound it makes) or memory of the general location of the valve positions. Though this is not the objective method in such an experiment, the amount of pressure variance between actual and observed will not likely be more than -5% . Because the pressure observed will always be greater than the actual pressure (since the flow is always in the same direction), the linear Stern-Volmer slope by which the electronic quenching is derived will be scarcely effected by these errors.

B.4 Multiple Exponentials. Often the fluorescence decay that appears as a single exponential is in fact a series of exponential curves of greatly varying decay rate. A single exponential fit to a series of multiple exponentials generates large error in the determination of the decay rate, particularly when the decay rate desired is of a larger

decay rate (shorter lifetime) than the other exponentials. There are two ways the experimenter may observe multiple exponentials; both are because this experiment analyzed quenching rates across a manifold of vibrational levels that transitioned from stable to unstable (predissociated) levels.

Multiple level pumping was a concern in this experiment because of bismuth dimers are spectrally dense in the A state. That is to say, there is significant overlap of rotational structure from competing vibrational levels. When selecting a vibrational level to pump with the dye laser, the experimenter must be aware of pumping two or more levels simultaneously as the observed decay will then be a sum of the proportional decays from each level. One way to mitigate this effect is to select a rotational level away from the bandhead and further away from any other vibrational level (as discussed in chapter 3). Fortunately, the neighboring bandhead will always be of a larger vibrational level (see figure 3.9). If another level pumped is a stable level ($v' < 23$), the quenching rates are independent of vibrational level and the effect of the multiple pumping will be minimal. If another level pumped is an unstable vibrational level, the decay rate will be so large as to approach zero much faster than the desired level. This is true even when the desired level is unstable as the quenching rates increase very rapidly with increasing vibrational level. The mitigation of multiple level pumping within the analysis is accomplished by the appropriate sectioning of data, whereby the sectioning begins after the undesired level is believed to have decayed. Obviously, this technique is heuristic in nature and is developed over several series of attempts at analysis.

The final result of multiple level pumping will appear in the residuals of the decay curves. The undesired exponential appears as a rapidly decaying sinusoid, a product of

the fitting routine averaging between two exponential decay curves. The data analyzed and reported here did not experience residuals of intensity greater than 1% of the observed decay rate. Multiple exponentials accounted for less than 2% of any observed decay rate and the effects are negligible compared to the much larger sources of error in the experiment.

An additional mechanism to generate multiple exponentials is by the V-T transfer of dimers across the vibrational manifolds. The effects would be similar to those encountered in the previous paragraph, except that the transfer is likely to include lower vibrational levels than the level under study. It is then possible to observe small proportions of stable fluorescence decay when observing an unstable vibrational level. These effects cannot be mitigated by sectioning, as the stable fluorescence decay will not return to baseline until well after the unstable level has. The phenomena of V-T transfer are interesting to observe and are included in the formulation of electronic quenching. The effects of V-T, therefore, were not a source of error and the only mitigation attempted was the differentiation between V-T transfer and multiple level pumping.

Bibliography

Babaky, O. S. "Molecular constants of the XO^+_g and AO^+_u states of Bi_2 ," Egyptian Journal of Physics 28, No. 1-2: 71-80 (1997).

Barrow, R. F. "Electronic States of Bi_2 ," Molecular Physics, Vol. 87: 725-733 (1996).

Benard, D. J. "Threshold Oscillation of an $\text{NF}(a^1\Delta)/\text{BiF}$ Visible Wavelength Chemical Laser," Journal of Applied Physics, 74: 2900-2907 (1993).

Bernath, Peter F. Spectra of Atoms and Molecules. Oxford: Oxford University Press, 1995.

Blondeau, J. M., G. Gandara, P. Carette and J. Messelyn. "Lifetimes of the AO^-_u State and Quenching Cross Sections of Bi_2 ," Chemical Physics Letters, Vol. 71: 246-252 (April, 1980).

Brown, John M. Molecular Spectroscopy. Oxford: Oxford University Press, 1998.

Dolezal, Michael W. Spectroscopic and Lifetime Studies of Diatomic Bismuth. Unpublished dissertation, Air Force Institute of Technology (AU), Wright Patterson AFB OH (June, 1999).

Drosch, S. and G. Gerber. "Optically pumped CW molecular bismuth laser," Journal of Chemical Physics, Vol. 77: 123-130 (July, 1982).

Fischer, Albert K. "Vapor Pressure of Bismuth," The Journal of Chemical Physics, 45: 375-377 (July, 1966).

Franklin, R. E. Spectroscopic and Kinetic Study of Bismuth Dimers. Air Force Institute of Technology (AU), Wright Patterson AFB OH, February, 1997.

Gerber, G., H. Honniger, and J. Janes. "Rotational analysis of the $\text{A} \rightarrow \text{X}$ bands system of Bi_2 ," Chemical Physics Letters, 85: 415-417 (January, 1982).

Gerber, G., and H. P. Broida, "Electronic States and Molecular Constants of Bi_2^* ," Journal of Chemical Physics, Vol. 64: 3410-3422 (April, 1976).

Herbelin, J. M. "Prospects of a Visible Chemical Laser," Applied Optics, 25: 2138 (1986).

Herzberg, Gerhard. Spectra of Diatomic Molecules. New York: Van Nostrand Reinhold Company, 1939.

Kondrat'ev, V. N. Chemical Kinetics of Gas Reactions. Reading, Mass.: Pergamon Press, 1964.

Landau, V. L. and E. Teller. Phys Z Sowj Un. 10: 35 (1936).

McKenna, P. "Set Lasers on Stun!" Airman, 41: 10-13, 1997.

Montroll, E. W. and K. E. Shuler. "Studies in the Nonequilibrium Rate Processes. The Relaxation of a System of Harmonic Oscillators," Journal of Chemical Physics, 26: 454 (1957).

Melton, David W., Glen P. Perram and Won B. Roh. "Collisional dynamics of the BrF $B^3\Pi(0^+)$ state. I. Electronic quenching," Journal of Chemical Physics, 96 (9): 6666-6671 (May, 1992).

Mulliken, R. S. "Some neglected subcases of Predissociation in Diatomic Molecules," Journal of Chemical Physics, Vol. 33: 247-252 (July, 1960).

Perram, Glen P. Collisional Dynamics of the $B^3(0^+)$ State of Bromine Monochloride. Air Force Institute of Technology (AU), Wright Patterson AFB, OH, August 1986.

Perram, Glen P. "Visible Chemical Lasers," Proceedings of the International Conference on LASERS '89: (1989).

Perram, Glen P. Class handout, CHEM 720, Chemical Kinetics. School of Engineering and Management, Air Force Institute of Technology, Wright-Patterson AFB OH, May 2000.

Perram, Glen P. Thesis Advisor. Personal interview. (2001).

Perram, Glen P. and S. J. Davis. "Collisional dynamics of the BrCl $B^3\Pi(0^+)$ state. II. Vibrational and rotational energy transfer," Journal of Chemical Physics, 98(1): 373-382 (January, 1993).

Pines, D. "APS Study: Science and Technology of Directed Energy Weapons," Reviews of Modern Physics, 59: 34 (1987).

Polanyi, J. C. "Proposal for an Infrared Maser Dependent on Vibrational Excitation," Journal of Chemical Physics, Vol 34: 347 (1961).

Schwartz, R. N., Z. I. Slawsky and K. F. Herzfeld. "Calculation of Vibrational Relaxation Times in Gases," Journal of Chemical Physics, Vol. 20: 1591-1599 (October, 1952).

Spectra-Physics (Laser Products Division). Quanta-Ray PDL-3, Pulsed Dye Laser Instruction Manual.

Steinfeld, Jeffrey I. Chemical Kinetics and Dynamics. New Jersey: Prentice Hall, 1999.

Stern, O. and M Volmer, Physik, Z80: 183, (1919).

Vizard, Frank. "Return to Star Wars," Popular Science: 57-61 (April, 1999).

West, W. P. and H. P. Broida. "Optically Pumped Vapor Phase Bi2 Laser," Chemical Physics Letters, Volume 56: 283-285 (June, 1978).

Vita

First Lieutenant Joseph Lee Cox (Joe) was born in San Diego County, California to Joe graduated from Granite Hills High School in El Cajon, California in 1990 and enrolled in Cuyamaca Community College the following year. Joe transferred to San Diego State University in San Diego, California, in 1995, enrolling in the Air Force Reserve Officers Training Corps, AFROTC, Detachment 075, at San Diego State University. He became the first person in the history of his family to graduate from college in May 1997 with a Bachelors degree in Physics. Two weeks later, Joe accepted a commission as a Second Lieutenant (2LT) in the United States Air Force. Two weeks after commissioning, 2LT Joseph Lee Cox married

One week after the wedding, the bride and groom moved to the Boston, Massachusetts area where Joe accepted his first assignment as a military satellite communications (MILSATCOM) scientist working with the Electronic Systems Center (ESC), MILSATCOM Systems Program Office, Hanscom Air Force Base, Massachusetts. 2LT Cox led the MILSATCOM Systems Program Office advanced technology infusion, with emphasis on development of wide-band airborne satellite communications for Nuclear Force Elements, military airlift aircraft, and large bomber aircraft. Additionally, 2LT Cox was the satellite communications lead for the Air Force's vaunted Expeditionary Forces eXperiment '98 (EFX-98). EFX-98 was a Chief of Staff of the Air Force (CSAF) directed live fly experiment designed to rapidly test, evaluate and field rapid air expeditionary forces tactics, doctrine, systems and technologies in an unprecedented 8 month integration schedule. During his tour at Hanscom Air Force Base, Joe also volunteered as a member of the Patriot Honor Guard performing over 50 veteran, retiree, and active duty funerals, and several community color guard postings and parades in 14 months with the Honor Guard. For his next tour of duty, Joe was assigned to Wright Patterson Air Force Base, Ohio, having been promoted to First Lieutenant just prior to departure from Hanscom Air Force Base. At Wright Patterson, 1LT Cox attended graduate school in residence at the Air Force Institute of Technology (AFIT), where he is currently completing his requirements for a Master of Science Degree in Applied Physics, specializing in Laser Optics. After graduation in March, 2001, 1LT Cox is expecting a follow on assignment to Eglin Air Force Base, Florida, where he will work on advanced electro-optics sensor systems for the Munitions Directorate, Air Force Research Laboratory.

REPORT DOCUMENTATION PAGE

 Form Approved
 OMB No. 074-0188

The public reporting burden for this collection of information is estimated to average 1 hour per response, including the time for reviewing instructions, searching existing data sources, gathering and maintaining the data needed, and completing and reviewing the collection of information. Send comments regarding this burden estimate or any other aspect of the collection of information, including suggestions for reducing this burden to Department of Defense, Washington Headquarters Services, Directorate for Information Operations and Reports (0704-0188), 1215 Jefferson Davis Highway, Suite 1204, Arlington, VA 22202-4302. Respondents should be aware that notwithstanding any other provision of law, no person shall be subject to a penalty for failing to comply with a collection of information if it does not display a currently valid OMB control number.

PLEASE DO NOT RETURN YOUR FORM TO THE ABOVE ADDRESS.

1. REPORT DATE (DD-MM-YYYY) 26-02-2001			2. REPORT TYPE Master's Thesis		3. DATES COVERED (From – To) Jun 2000 – Feb 2001
4. TITLE AND SUBTITLE ELECTRONIC QUENCHING OF THE A(0 ⁺) STATE OF Bi ₂			5a. CONTRACT NUMBER		
			5b. GRANT NUMBER		
			5c. PROGRAM ELEMENT NUMBER		
6. AUTHOR(S) Cox, Joseph, L., First Lieutenant, USAF			5d. PROJECT NUMBER		
			5e. TASK NUMBER		
			5f. WORK UNIT NUMBER		
7. PERFORMING ORGANIZATION NAMES(S) AND ADDRESS(S) Air Force Institute of Technology Graduate School of Engineering and Management (AFIT/EN) 2950 P Street, Building 640 WPAFB OH 45433-7765				8. PERFORMING ORGANIZATION REPORT NUMBER AFIT/GAP/ENP/01M-02	
9. SPONSORING/MONITORING AGENCY NAME(S) AND ADDRESS(ES) Dr. Michael Berman AFOSR/NL				10. SPONSOR/MONITOR'S ACRONYM(S)	
				11. SPONSOR/MONITOR'S REPORT NUMBER(S)	
12. DISTRIBUTION/AVAILABILITY STATEMENT APPROVED FOR PUBLIC RELEASE; DISTRIBUTION UNLIMITED.					
13. SUPPLEMENTARY NOTES					
14. ABSTRACT Temporally-resolved laser induced fluorescence of high vibrational levels in Bi ₂ A(0 ⁺ _u) above and below the predissociation limit of v'=22 were investigated by observing total fluorescence from a wavelength tunable, pulsed dye laser. Electronic quenching of Bi ₂ A(0 ⁺ _u) by five collision partners (Ne, Ar, Kr, Xe, N ₂) was examined for four vibrational levels (v'=22, 23, 24, 25). Electronic quenching by a sixth collision partner (He) was examined for eight vibrational levels (v'=18 through 25). The quenching from stable vibrational levels (v'≤22) was independent of vibrational quantum number. A significant increase in quenching occurs for the predissociated level v'=23. Electronic quenching transfer rates ranged from 227.3 to 850.5x10 ¹³ cm ³ molec ⁻¹ sec ⁻¹ for v'=22 and from 741.2 to 1570x10 ¹³ cm ³ molec ⁻¹ sec ⁻¹ for v'=23, and are very nearly gas kinetic for v'=23. Electronic quenching of higher vibrational levels (v'>23) was not temporally resolvable by the experimental apparatus.					
15. SUBJECT TERMS Laser, Laser Induced Fluorescence, Chemical Kinetics, SSH Theory, Bismuth, Bismuth Dimers, Spectroscopy, Landau Teller, Predissociation, Quenching, Electronic Quenching, Lifetime, Vibrational Transfer, Collisional Quenching, Temporally Resolved					
16. SECURITY CLASSIFICATION OF:		17. LIMITATION OF ABSTRACT UU	18. NUMBER OF PAGES UU	19a. NAME OF RESPONSIBLE PERSON LtCol G. P. Perram, AFIT/ENP	
a. REPOR T U	b. ABSTR ACT U			c. THIS PAGE U	19b. TELEPHONE NUMBER (Include area code) (937) 255-3636

 Standard Form 298 (Rev. 8-98)
 Prescribed by ANSI Std. Z39-18

 Form Approved
 OMB No. 074-0188